Investigation of Copper Chloride for Photonics Applications

by

Dominik Danieluk

A thesis submitted to the

University of Dublin

for the degree of

Doctor of Philosophy

University of Dublin

School of Physics

Trinity College Dublin

April, 2011

Declaration

I declare that the work in this thesis has not been previously submitted as an exercise for a degree to this or any other university. The work described herein is entirely my own, except for the assistance mentioned in the acknowledgements and the collaborative work mentioned in the list of publications. I agree that Trinity College Library may lend or copy this thesis on request.

Investigation of Copper Chloride for Photonics Applications

by Dominik Danieluk

Summary:

Wide band gap semiconductors have found multiple applications. Being light emitters in the range of blue and UV, materials like GaN or ZnO have been applied to highly efficient blue light emitting diodes, and increasingly popular high power and efficient white light emitters or blue lasers. Due to significant lattice mismatches with their substrates both GaN and ZnO suffer from a large number of material defects. Advanced growth techniques allowed us to achieve satisfactory results, but at the cost of fabrication simplicity, which has impacted on the production cost. Another interesting property of wide band-gap semiconductors is high exciton binding energy. In GaN this energy is of the order of 25 meV, which corresponds to the room temperature thermal energy. ZnO has a significantly higher exciton binding energy of 60 meV. High exciton binding energies are of high importance since they allow exciton based processes to take place at higher temperatures. A lot of research is being done towards exciton driven lasing, condensation and other phenomena which can potentially lead to new types of highly efficient photonic devices. Copper chloride, with a band gap of 3.4 eV, which is comparable with both GaN and ZnO, is their natural competitor. Having an exciton binding energy of 190 meV makes this a very promising material for exciton driven photonics. Moreover, due to close matching with Si, high quality deposition of CuCl can be achieved using relatively simple and cheap vacuum deposition technique.

The high quality of CuCl layers deposited on Si substrate have been confirmed with X-ray spectroscopy and the optical properties of CuCl have been investigated using temperature dependent spectroscopy. From the thermal dependence of the free exciton peak width and intensity, the number of parameters can be deduced, and the FWHM increases with temperature. Such a broadening is the result of exciton phonon interactions. The parameters describing the exciton-phonon interactions are deduced from the PL spectra. Normalised integrated PL intensity dependence on temperature gives information on the processes involved in PL thermal quenching. The thermal activiation energies have been determined. Similar analysis has been conducted on the PL spectra of the CuCl sister semiconductor, CuBr. Both are members of the I-VII semiconductors group and, more precisely, they are known as copper halides. They have similar optical properties, although the lattice mismatch with Si is an order of magnitude higher for CuBr. The influence of oxygen on the optical properties of CuCl on Si is also investigated. Oxygen is expected to be a p-type dopant. The oxygen-argon plasma treated CuCl on Si samples were studied with temperature dependent PL. New behaviour of PL intensity thermal dependence is observed as negative thermal quenching (NTQ) of photoluminescence. The thermal activation energy of the process involved in NTQ was calculated as approximately 10 meV.

For CuCl on Si the refractive index in the range of 244-1600 nm was obtained using ellipsometry. The refractive index is very important in the simulation process.

Besides the interesting properties in the UV/blue wavelength range, CuCl also has relatively low absorption in parts of the THz band. Since this region of electromagnetic radiation attracts a lot of attention, the usability of CuCl as a photonic crystal component is investigated. The photonic crystal is a periodic structure of different dielectrics and, like the semiconductor, forbids the propagation of particular electron energies depending on its structure; thus a photonic crystal can be designed to forbid particular photon frequencies. The structures of four different CuCl and air lattices are investigated. For a triangular lattice a mirror of reflectivity exceeding 90% at 8.56 THz at room temperature has been designed. A reflectivity of 98% is achievable for frequencies below 3 THz, but only at low temperatures.

Placing the semiconductor inside an optical cavity can influence the emission properties. Depending on the relation between the excitonic oscillator strength and the cavity finesse two distinct regimes can be distinguished. If the cavity influence can be described as perturbation only the interaction is known as a weak coupling. If the influence of the cavity is more significant, such that the interacting cavity phonon and the semiconductor exciton constitute a new quantum state, the cavity operates in the strong coupling regime. Both regimes are studied. The possibility of light extraction enhancement in weak coupling microcavities is investigated. The modification of spatial patterns leading to selective promotion of angular modes is not observed in bulk microcavities. Due to high absorption of CuCl the potential enhancement originating in the spatial pattern modification is limited. However, the extraction efficiency enhancement by means of substrate and thickness modification was demonstrated.

Due to very strong oscillator strength and high exciton binding energy copper chloride has been studied as a material for polariton driven PL emitters. From the reflectivity spectra of CuCl based optical microcavities the dispersion of the cavity polaritons has been deduced. For the first time strong exciton-photon coupling has been observed in bulk CuCl microcavity at room temperature. High Rabi splitting energy of 275 meV is obtained.

Acknowledgments

I would like to thank Dr. Louise Bradley for giving me the opportunity to work in semiconductor photonics group under her excellent supervision. Her support and encouragement during past four years of my PhD course made this work possible.

I would also like to thank all the people in semiconductor group I have had a pleasure to work with. I might not be able to mention all of them, but personally I would like to thank Dr. Vincent Weldon for his help.

Thanks also to all the friend I met during the course, here in semiconductor photonics group. Work with you was a pleasure and a great experience.

Many thanks for the all the help I got from Dr. Loic Bodiou, Dr. Clare Higgins, Rob Lennox and Ciaran Smith.

Thanks to the DCU team. To Prof. Paddy McNally, Dr. Francis Olabanji Lucas, Aidan Cowley, Barry Foy, Monjarul Aram and Rajani. Your help was invaluable.

I also want to thank Dr. Pascal Landais and Elif Degirmenci for the time spent together on the photonic crystals project.

Special thanks to my parents Teresa and Zbigniew Danieluk for constant support and love.

Finally I would like to thank my wife Edyta for love, patience and understanding, especially at the end of this work.

Table of Contents

Summary III

Acknowledgments V

Table of Contents VII

List of Presentations and Publications IX

1 Introduction 1

1.1 Thesis background 1

1.2 Thesis outline 4

1.3 References 6

2 CuCl material properties 11

2.1 Properties 11

2.2 Sample preparation 13

2.3 Measurements 13

2.3.1 XRD 13

2.3.2 Photoluminescence 14

2.3.3 Power dependence of PL emission 17

2.3.4 Oxygen treated CuCl on Si layers 25

2.3.5 CuCl refractive index determination from ellipsometry data 29

2.4 Conclusions 33

2.5 References 34

3 CuCl Photonic Crystals for TeraHertz Applications 39

3.1 Introduction 39

3.2 The theory 41

3.2.1 Photonic Crystal Theory 41

3.2.2 The plane wave expansion method 43

3.3 Comparison of different CuCl structures 48

3.4 Conclusions 57

3.5 References 59

4 Microcavity LED 63

4.1 Introduction 63

4.2 Background 63

4.2.1 The extraction efficiency 64

4.2.2 The radiative transitions 65

4.2.3 The influence of microcavity on emission spatial profile 67

4.3 The transfer matrix model 71

4.4 Modelling the light extraction 74
4.5 CuCl on Si Substrate 77
4.6 Conclusions 91
4.7 References 92
5 Cavity polaritons in CuCl based microcavities 94
5.1 Background 94
5.2 The light-matter interaction. 95
5.2.1 The weak coupling regime 95
5.2.2 The strong coupling regime 96
5.2.3 The model 96
5.3 Investigation of a bulk CuCl microcavity 98
5.4 The bulk CuCl microcavity 101
5.4.1 Tuning the cavity resonance 101
5.4.2 The semiconductor cavity - theory 103
5.5 The experiment 105
5.5.1 The sample 105
5.5.2 The reflectivity setup 106
5.5.3 The results 106
5.6 Conclusions 109
5.7 References 111
6 Conclusions and future work 113
6.1 Conclusions 113
6.2 Future work 115

List of presentations and publications

A. Mitra, L. O'Reilly, O. F. Lucas, Gomathi Natarajan, D. Danieluk, A. L. Bradley, P. J. McNally, S. Daniels, D. C. Cameron, A. Reader, and M. Martinez-Rosas, **"Optical properties of CuCl films on silicon substrates"**, phys. stat. sol. (b), 1– 7 (2008), DOI 10.1002/pssb.200844021

Dominik Danieluk, A. L. Bradley, A. Mitra, L. O'Reilly, O. F. Lucas, A. Cowley, P. J. McNally, B. Foy, E. McGlynn, **"Optical properties of undoped and oxygen doped CuCl films on silicon substrates",** Journal of Materials Science: Materials in Electronics, DOI 10.1007/s10854-007-9448-5

A. Cowley, F. O Lucas, E. Gudimenko, M. M. Alam, D. Danieluk, A. L. Bradley, P. J. McNally, **"Electroluminescence of CuBr thin films via vacuum evaporation depositon",** *Journal of Physics D: Applied Physics*, vol. 43, p. 165101, 2010

M. M. Alam, F. Olbanji Lucas, D. Danieluk, A. L. Bradley, K. V. Rajani, S. Daniels, P. J. McNally, **"Hybrid organic–inorganic spin-on-glass CuCl films for optoelectronic applications"** *J. Phys. D: Appl. Phys.*, vol. 42, p. 225307, 2009

F. O Lucas, P. J. McNally, A. Cowley, S. Daniels, L. Bradley, D. Danieluk, D. M. Taylor, **"Structural, optical and electrical properties of Co-evaporated CuCl/KCl films"** *physica status solidi (c)*, vol. 6, no. 1, pp. S114–S118, 2009

A. Cowley, B. Foy, D. Danilieuk, P. J. McNally, A. L. Bradley, E. McGlynn, A. N. Danilewsky, **"UV emission on a Si substrate: Optical and structural properties of CuCl on Si grown using liquid phase epitaxy techniques"** *physica status solidi (a)*, vol. 206, no. 5, pp. 923–926, 2009

Dominik Danieluk, A.L. Bradley, A. Mitra, P.J. McNally, L. O'Reilly, G. Natarajan, A. Cowley, B. Foy, E.McGlynn and D.C. Cameron

"Optical properties of CuCl on silicon substrate towards UV photonic devices"

Oral presentation at:

Second International Conference on Optical, Optoelectronic and Photonic Materials and Applications 2007, London, 30 July – 3 August 2007

D. Danieluk, A.L. Bradley, P.J. McNally, L. O'Reilly, O. F. Lucas, G. Natarajan, S. Daniels, E.McGlynn, A. Cowley, B. Foy and D.C. Cameron

"Optical properties of CuCl on Si substrates – toward UV photonic devices"

Poster at:

Photonics Ireland 2007, Galway, 24-26 September 2007

F. O. Lucas, P.J. McNally, A. Cowley, L. Bradley, D. Danieluk

"Structural, Optical and Electrical Properties of Co-evaporated CuCl/KCl films"

Oral presentation at:

Third International Conference on Optical, Optoelectronic and Photonic Materials and Applications, Edmonton, 20-25 July 2008

1 Introduction

1.1 Thesis background

The ability to control the conduction of electrons provides the basis for electronics. This field of science has engaged vast resources, leading to fast progress in electronics and it's related fields. The invention of the transistor in late forties of the twentieth century began a new era in electronics. Data processing became easily available. The transistor became the basic element of devices now present in every aspect of our lives. The demand for making these devices more powerful, stable, efficient and smaller could be satisfied. However, due to the physical constraints, further progress by means of miniaturization, without a paradigm shift in approach, is reaching its limit. The dimensions of transistor features comprising the integrated circuits have decreased from approximately 10 microns originally, to tens of nanometres at present. At approximately a 32 nm scale, quantum mechanical effects which lead to the current leakage at the logic gate, start to play a significant role, thus further miniaturisation could become uneconomical even before the theoretical limits are reached. Nevertheless, the need for ever increasing performance prevails. This limitation originates in fermionic nature of electrons. Electron-electron interactions lead to system heating with increased frequencies. It was found that a photon being able to constitute coherent states is a more suitable information carrier than an electron. Photon-photon interaction is very weak thus photon beams can pass each other and the carried information is not lost. The invention of optical fibres in the sixties and finally the practical application of this invention in the seventies, initiated the branch of physics we know today as photonics. The need for controlling light propagation spurred research on light emitters, modulators, detectors and conductors. At present, the complete replacement of electron-based technology with photonics based technology is not possible. The present time can be perceived as the era of hybrid electronic/photonic technologies. Great progress has been made in the development of light emitters and detectors. Also, solutions for long distance transmission of light have been implemented. However, the basis of electronic devices, the transistor, is still beyond the reach of photonics. Thus, the data-carrying optical signals have finally encountered a bottle-neck in the form of electronic processing. As can be seen, to achieve the goal of fully optical computing, every step towards this direction is valuable. In this work an interesting material system will be discussed. Copper (I) chloride (CuCl) is closely matched with silicon in terms of its lattice constant. The combination of wide band gap semiconductor capable of emitting in UV/visible (CuCl) and the very mature base material of electronics (Si) is very promising from the point of view of hybrid electronic-photonic devices. Due to its optical properties, in many ways outperforming those of other wide band-gap semiconductors, CuCl is also a potential candidate for more traditional applications. Strong

UV/blue emission at room temperature makes it an ideal candidate for high power, low cost LEDs. Materials like GaN or ZnO suffer from a lack of suitable substrate. The high level od lattice mismatch in GaN (13%) leads to a large number of threading dislocations affecting the longevity of the device. This major problem was overcome with a rather complex growth method involving the transition layer between the substrate and the active region. Due to the lattice matching with silicon it will be possible to grow high quality materials without the need of such a sophisticated technique. Thus CuCl is expected to be a possible replacement for GaN and ZnO in the field of white LEDs or high power short wavelength lasers.

Semiconductors having a band-gap exceeding approximately 2.6 eV are suitable for UV/blue emission. Short wavelength semiconductor electroluminescent devices are highly interesting for many applications, among which are high density optical data storage [1], high power and efficient LEDs [2] or UV photodetectors [3]. The combination of UV/blue emitters with phosphors allows for the building of high efficiency white light LEDs [4]. In order to fabricate the successful electroluminescent device a p-n junction has to be built. Thus the issue of doping has to be addressed. Many wide band-gap semiconductors have been found to be difficult to dope [5-7]. The efforts to realise a miniaturised semiconductor blue laser had been unsuccessful for many years due to a lack of appropriate materials. Group II-VI materials like ZnS, ZnSe, or CdTe were investigated for many decades before GaN blue laser was successfully fabricated [8-11]. In order to fabricate a room temperature laser, very high quality materials are required. GaN has a wide band-gap of 3.28 eV, and a relatively high exciton binding energy of 28 meV, however suffers from a mismatch with its substrate – sapphire [12]. This mismatch, on the order of 18%, leads to a large number of threading dislocations which affects a devices's performance in terms of longevity, efficiency and thermal stability. The research then concentrated heavily on improving the GaN devices and overcoming these limitations [13], [14]. Advanced growth techniques, such as epitaxial lateral overgrowth (ELO), helped to reduce the number of dislocations in the GaN active region [15], [16]. However, increased growth sophistication resulted in the further complication of an already complex GaN device fabrication process, with a resultant increase in processing costs.

Another material that attracted a lot of attention as a potential GaN competitor is zinc oxide (ZnO) which has a band-gap of 3.37 meV and an exciton binding energy of 60 meV [17]. ZnO also suffers from the lack of a naturally matched substrate. The mismatch with SiC is of 18%. Additionally ZnO was found to be difficult to be p-doped [18]. However, the UV laser diode based on ZnO/MgZnO quantum wells was already fabricated [5]. The output power of such a diode is significantly lower than that of GaN based devises [1], [19]. A lot of work is being done on ZnO towards quantum confined structures [17]. Due to a high surface to volume ratio, structures like ZnO nanowires or nancrystals are very efficient radiation detectors[17]. Although the greatest

progress was made in terms of GaN and ZnO application, the field remains open for alternative materials. The level of study so far undertaken on CuCl is at a much earlier stage than that of those semiconductors mentioned above, however the promising results are encouraging for further research on CuCl and other copper halides.

In this work a novel material system, namely CuCl on Si, is studied. Copper (I) chloride has a band-gap of 3.39 eV and is closely lattice matched to the silicon (<0.4%). With an exciton binding energy of 190 meV [20], significantly exceeding that of both GaN and ZnO, CuCl is a promising alternative. Additionally, the close lattice match with the dominant electronics material, Si, potentially enables fabrication of hybrid electro-photonic devices.

CuCl has been researched for many years. Early publications appeared in the 1950s [21], [22]. Early research concentrated on the absorption and the luminescence of single crystals, bulk material, polycrystalline and amorphous layers grown on various substrates [21-27]. In 1968 the biexciton in CuCl was discovered [28] initiating interest in this aspect of CuCl properties [27], [29], [30]. The biexciton is a quasiparticle built of two excitons thus bounds two electrons and two holes. Such a quasiparticle resembles to some extent the hydrogen molecule, H_2. The annihiliation of a biexciton results in a remaining free exciton and creation of a photon. The photon energy is lower than that of the free exciton. The difference is the biexciton binding energy. Biexciton lasing in CuCl was demonstrated [31-33]. Also the nonlinear optical properties were investigated in CuCl [34], [35]. The progress in the material fabrication technology moved the attention to CuCl quantum confined structures, such as quantum spheres, embedded CuCl microcrystals and a thin layers [31-33], [36-46]. The semiconductor structures spatially limited in 1, 2 or 3 dimensions helped to understand how the emission of photons in semiconductors can be controlled. With this knowledge increasing, phenomena such as luminescence enhancement, ultra low threshold polariton lasing [47-49], and polariton Bose-Einstain condensation [50-52] were demonstrated. The evidence of quantum entangled photons generation from CuCl biexcitons was also reported [53]. Strong coupling between the cavity photon and CuCl exciton was observed at low temperatures in the CuCl microcavities [54], [55].

To investigate many novel concepts and phenomena, much of the research has concentrated on the most mature optoelectronic material, GaAs, which has a bandgap in the near-infrared. With the introduction of wide band-gap semiconductors new possibilities arise. Wide band gap semiconductors have much higher exciton binding energies than GaAs [56]. Due to this, the exciton related phenomena, which could only be studied at low temperatures, less than 100K in Gas based materials, can now manifest at high temperatures in materials such as GaN or ZnO [57-60]. Thermal energy at 300K is of approximately 25 meV. This value is very close to the exciton binding energy in GaN. ZnO excitons have binding energy exceeding that of room temperature thermal energy by ~35 meV. CuCl has the highest exciton binding energy of these three materials

thus was used for the fundamental studies of the physics of excitons since the 1960s. Most applications of optoelectronic materials such as lasers, light emitting diodes and optical amplifiers have not depended on the fundamental exciton state. New device concepts, particularly in the area of polariton devices, do require the exciton and so CuCl can have a significant advantage.

The successful application of CuCl must be preceded by thorough examination of the material properties. In this thesis the structural and optical properties of CuCl layers deposited on Si will be discussed. The complex refractive index of CuCl over a wide range of energies, including the band-gap energy, is deduced from ellipsometry measurements. The refractive index is a crucial parameter for simulations of CuCl based structures. Optical microcavities with bulk CuCl as an active medium are discussed, with emphasis on light extraction for potential light emitting diode applications. Experimentally, the strong light-matter coupling evidence in bulk CuCl miocrocavity at room temperature is demonstrated for the first time. A very large Rabi splitting of 275 meV is observed.

Copper chloride can also potentially find application as a waveguide in the growing field of THz radiation. This band of electromagnetic waves has remained *terra incognita* of applied physics for many years. The reason for this lies in the nature of THz radiation. Being the transition between infrared and radio frequencies, THz possesses shortcomings of both. However in more recent times it has been recognised that THz radiation may be viable for many applications [61] such as, for instance, fast data communication [62], [63]. However, because of omnipresent water vapours, free air THz transmission is dramatically limited, practically only to laboratory applications [64]. Thus the search for waveguiding options is on-going. Again, the interaction of THz radiation with vibrational modes of molecules leads to the significant attenuation in waveguides [65], [66]. Wire-like metal conductors were found to be poor THz guides due to limited conductivity of metals. Some promising results were obtained for the periodic structures of different dielectric materials [67-70]. Such structures, known as photonic crystals (PC), can be rather easily fabricated for THz waves. The physical dimensions of involved structures are of the range of microns or tens of microns in THz range. The constituent materials of PCs should possibly have the lowest absorption for THz radiation, preferably none. Such materials are very rare. One of them, high resistivity silicon (HR-Si), is rather expensive in fabrication, thus alternative materials are researched. CuCl has relatively low absorption in parts of THz band and so simulations of CuCl based photonic crystals, designed as THz mirrors, are investigated in this work.

1.2 Thesis outline

In **Chapter Two** the material properties of CuCl are investigated. The sample preparation using the physical evaporation technique is described. The quality and optical properties of

the vacuum evaporated CuCl on Si are discussed. The analysis of temperature dependent photoluminescence provides a number of important material parameters for comparison with CuCl deposited on other substrates and single crystal CuCl. Results for CuBr are also presented. The development of a p-n junction is the first step toward a light emitting device. In order to fabricate such a junction controlled doping of CuCl has to be achieved. Oxygen is considered to be a potential p-type dopant. Oxygen plasma treated samples of CuCl are optically analysed in order to determine the influence of oxidisation on CuCl optical properties. Finally in this chapter the complex refractive index of CuCl over a wide wavelength range, including at wavelengths below the bandgap, is determined using spectroscopic ellipsometry. The complex refractive index is one of the most crucial parameters of a material and is essential for the optical simulation of the material in structures and devices.

Chapter Three investigates four CuCl photonic crystal structures with a view to applications in the THz region of the electromagnetic spectrum. Due to the relatively low absorption coefficient at low temperatures below 3THz CuCl can potentially find application in this field. Also at room temperature over 8THz CuCl absorption remains small.. From the band-gap maps the lattice parameters are obtained and using the transfer matrix method the reflectivity spectra of CuCl THz mirrors are discussed.

Chapter Four presents the study of CuCl microcavities working in weak coupling regime and addresses the issue of light extraction from CuCl based light emitting devices. The simulations done using the transfer matrix method show the dependence of light extraction on the CuCl layer thickness and the substrate optical properties. The possibilities for maximising the extraction efficiency are discussed.

In **Chapter Five** the regime of strong light-matter coupling inside a bulk CuCl based microcavity is discussed. CuCl is considered for room temperature polariton devices. The very high exciton binding energy of 190 meV compared with other wide bandgap materials such as GaN and ZnO can offer significant advantage for room temperature operation. A simple bulk microcvaity is designed and fabricated. Evidence for strong coupling at room temaperature, through observation of anti-crossing of the upper and lower polariton branches, is investigated using reflectivity measurements. The results are compared with simulation.

The conclusions are presented in **Chapter Six**.

1.3 References

[1] M. Shono, "High-power blue-violet laser diodes for next-generation optical disc systems," in *Proceedings of SPIE*, pp. 411-416, 2004.

[2] S. Hon, C. T. Kuo, T. P. Chen, and M. H. Hsieh, "High power GaN LED chip with low thermal resistance," in *Proc. of SPIE Vol*, vol. 6894, pp. 689411–1.

[3] F. Omnès, E. Monroyb, E. Mu\ nozc, and J. L. Reverchond, "Wide bandgap UV photodetectors: A short review of devices and applications," in *Proc. of SPIE Vol*, vol. 6473, pp. 64730E–1.

[4] S. C. Allen and A. J. Steckl, "A nearly ideal phosphor-converted white light-emitting diode," *Applied Physics Letters*, vol. 92, p. 143309, 2008.

[5] S. Chu, M. Olmedo, Z. Yang, J. Kong, and J. Liu, "Electrically pumped ultraviolet ZnO diode lasers on Si," *Applied Physics Letters*, vol. 93, no. 18, p. 181106, 2008.

[6] I. Akasaki, H. Amano, M. Kito, and K. Hiramatsu, "Luminescence of Mg-doped p-type GaN and electroluminescence of GaN p-n junction LED," *Journal of Luminescence*, vol. 48, pp. 666-670, 1991.

[7] U. V. Desnica, "Wide band-gap II-VI compounds–can efficient doping be achieved?," *Vacuum*, vol. 50, no. 3, pp. 463–471, 1998.

[8] A. Ishibashi and Y. Mori, "Advances in blue laser diodes," *Journal of Crystal Growth*, vol. 138, no. 1, pp. 677–685, 1994.

[9] N. Lovergine et al., "MOVPE Growth of Wide Band-Gap II-VI Compounds for Near-UV and Deep-Blue Light Emitting Devices," *Crystal Research and Technology*, vol. 33, no. 2, pp. 183–195, 1998.

[10] H. Luo and J. K. Furdyna, "The II-VI semiconductor blue-green laser: challenges and solution," *Semiconductor Science and Technology*, vol. 10, p. 1041, 1995.

[11] T. Tauchi, Y. Yamada, T. Ohno, J. T. Mullins, and Y. Masumoto, "Ultraviolet laser and photodetector of CdZnS/ZnS multiple quantum wells," *Physica B: Condensed Matter*, vol. 191, no. 1, pp. 136–139, 1993.

[12] S. Nakamura et al., "InGaN/GaN/AlGaN-based laser diodes with modulation-doped strained-layer superlattices grown on an epitaxially laterally overgrown GaN substrate," 1998.

[13] S. Pal and C. Jacob, "Silicon—a new substrate for GaN growth," *Bull. Mater. Sci.*, vol. 27, no. 6, pp. 501-504, 2004.

[14] P. Trautman, K. Pakula, and J. M. Baranowski, "The fundamental absorption edge of

high crystalline quality GaN and that of amorphous GaN grown at low temperature," *physica status solidi (c)*, vol. 2, no. 3, 2005.

[15] T. S. Zheleva, O. H. Nam, M. D. Bremser, and R. F. Davis, "Dislocation density reduction via lateral epitaxy in selectively grown GaN structures," 1997.

[16] P. Gibart, "Metal organic vapour phase epitaxy of GaN and lateral overgrowth," *Rep. Prog. Phys.*, vol. 67, pp. 667-715, 2004.

[17] C. Jagadish and S. J. Paerton, *Zinc Oxide Bulk, Thin Films and Nanostructures. Processing, Properties and Applications*. 2007.

[18] X. Li, S. Asher, B. Keyes, H. Moutinho, J. Luther, and T. Coutts, "p-Type ZnO Thin Films Grown by MOCVD," in *Version 4A, Los Alamos National Laboratory Manual LA-12625-M, Los Alamos National Laboratory, Los Alamos, New Mexico, USA*, 2005.

[19] T. Kozaki, S. Nagahama, and T. Mukai, "Recent progress of high-power GaN-based laser diodes," in *Proc. of SPIE Vol*, vol. 6485, pp. 648503–1.

[20] K. L. Shaklee, R. F. Leheny, and R. E. Nahory, "Stimulated Emision from the Excitonic Molecules in CuCl," *Phys. Rev. Lett.*, vol. 26, no. 15, pp. 888-891, 1971.

[21] L. M. Kraemer, "Cuprous Halide Films on Alkali Halide Crystals," 1960.

[22] I. Tsujikava and E. Kanda, *Fluorescence Spectra of Cuprous Halides at Low Temperatures*. 1954.

[23] T. Goto, T. Takahashi, and M. Ueta, "Exciton Luminescence of CuCl, CuBr and CuI Single Crystals," *Journal of the Physical Society of Japan*, vol. 24, no. 2, pp. 314-327, 1968.

[24] A. F. Armington and J. J. O'connor, "Gel growth of cuprous halide crystals," *Journal of Crystal Growth*, vol. 3, no. 4, pp. 367-371, 1968.

[25] M. Cordona, "Optical Properties of the Silver and Cuprous Halides," *Phys. Rev.*, vol. 129, no. 1, pp. 69-78, 1963.

[26] D. Frohlich, B. Staginnus, and E. Schonherr, "Two-Photon Absorption Spectrum of CuCl," *Phys. Rev. B*, vol. 19, no. 18, pp. 1032-1034, 1967.

[27] T. Goto, H. Souma, and M. Ueta, "Emission spectra of cuprous halides and their correlation with exciton," 1970.

[28] A. Mysyrowicz, J. B. Grun, R. Levy, A. Bivas, and S. Nikitine, "Excitonic molecule in CuC1," *Physics Letters A*, vol. 26, no. 12, pp. 615-616, 1968.

[29] L. L. Chase, N. Peyghambarian, G. Grynberg, and A. Mysyrowicz, "Evidence for Bose-Einstein Condensation of Biexcitons in CuCl," *Phys. Rev. Lett.*, vol. 42, no. 18, pp. 1231-1234, 1979.

[30] N. Peyghambarian, H. M. Gibbs, M. C. Rushford, and D. A. Weinberger, "Observation of Biexcitonic Optical Bistability and Optical Limiting in CuCl," *Phys. Rev. Lett.*, vol. 51, no. 18, pp. 1692-1695, 1983.

[31] Y. Masumoto, T. Kawamura, and K. Era, "Biexciton lasing in CuCl quantum dots," *Appl. Phys. Lett.*, vol. 62, no. 3, pp. 225-227, 1993.

[32] G. Oohata et al., "Stable biexcitonic lasing of CuCl quantum dots under two-photon resonant excitation," *Physica E: Low-dimensional Systems and Nanostructures*, vol. 26, no. 1, pp. 347–350, 2005.

[33] Y. Kagotani et al., "Two-photon absorption and lasing due to biexciton in CuCl quantum dots," 2005.

[34] S. D. Kramer and N. Bloemberg, "Third-order nonlinear optical spectroscopy in CuCl," *Phys. Rev. B*, vol. 14, no. 10, pp. 4654-4669, 1976.

[35] D. C. Haueisen and H. Mahr, "Nonlinear Electronic Dispersion in CuCl," *Physical Review Letters*, vol. 26, no. 14, pp. 838-840, 1971.

[36] M. Nakayama, H. Ichida, and H. Nishimura, "Bound-biexciton photoluminescence in CuCl thin films grown by vacuum deposition," *J. Phys. Condens. Matter*, vol. 11, no. 39, pp. 7653-7662, 1999.

[37] S. Yano, T. Goto, T. Itoh, and A. Kasuya, "Dynamics of excitons and biexcitons in CuCl nanocrystals embedded in NaCl at 2 K," *Phy. Rev. B*, vol. 55, no. 3, pp. 1667-1672, 1997.

[38] Y. Masumoto, T. Wamura, and A. Iwaki, "Homogenous width of exciton absorption spectra in CuCl microcrystals," *Appl. Phys. Lett.*, vol. 55, no. 24, pp. 2535-2537, 1989.

[39] A. Nakamura, H. Yamada, and T. Tokizaki, "Size-dependent radiative decay of excitons in CuCl semiconducting quantum spheres embedded in glasses," *Phys. Rev. B*, vol. 40, no. 12, pp. 8585-8588, 1989.

[40] Y. Kayanuma, "Wannier exciton in microcrystals," *Solid State Communications*, vol. 59, no. 6, pp. 405–408, 1986.

[41] Y. Masumoto, S. Okamoto, and S. Katayanagi, "Biexciton binding energy in CuCl quantum dots," 1994.

[42] D. K. Shuh, R. S. Williams, Y. Segawa, J. Kusano, Y. Aoyagi, and S. Namba, "Line-shape and lifetime studies of exciton luminescence from confined CuCl thin films," *Phys. Rev. B*, vol. 44, no. 11, pp. 5827-5833, 1991.

[43] T. Wamura, Y. Masumoto, and T. Kawamura, "Size-dependent homogeneous linewidth of Z3 exciton absorption spectra in CuCl microcrystals," *Applied physics*

letters, vol. 59, no. 14, pp. 1758–1760, 2009.

[44] T. Itoh, M. Furumiya, T. Ikehara, and C. Gourdon, "Size-dependent radiative decay time of confined excitons in CuCl microcrystals," *Solid State Communications*, vol. 73, no. 4, pp. 271-274, 1990.

[45] M. Nagai, F. Hoshino, S. Yamamoto, R. Shimano, and M. Kuwata-Gonokami, "Spherical cavity-mode laser with self-organized CuCl microspheres," 1997.

[46] H. Kurisu, K. Nagoya, N. Nakayama, S. Yamamoto, and M. Matsuura, "Exciton and biexciton properties of CuCl microcrystals in an SiO2 matrix prepared by sputtering method," *J. Lumin.*, vol. 87, pp. 390-392, 2000.

[47] H. Deng, G. Weihs, D. Snoke, J. Bloch, and Y. Yamamoto, "Polariton lasing vs. photon lasing in a semiconductor microcavity," *Proceedings of the National Academy of Sciences of the United States of America*, vol. 100, no. 26, p. 15318, 2003.

[48] S. Christopoulos et al., "Room-Temperature Polariton Lasing in Semiconductor Microcavities," *Physical Review Letters*, vol. 98, no. 12, 2007.

[49] G. Malpuech, A. Di Carlo, A. Kavokin, J. J. Baumberg, M. Zamfirescu, and P. Lugli, "Room-temperature polariton lasers based on GaN microcavities," *Applied Physics Letters*, vol. 81, no. 3, p. 412, 2002.

[50] J. Kasprzak et al., "Bose–Einstein condensation of exciton polaritons," *Nature*, vol. 443, no. 7110, pp. 409-414, 2006.

[51] H. Deng and Y. Yamamoto, "Exciton-polariton Bose-Einstein condensation," *Reviews of Modern Physics*, vol. 82, no. 2, pp. 1489-1537, 2010.

[52] P. Littlewood, "PHYSICS: Condensates Made of Light," *Science*, vol. 316, no. 5827, pp. 989-990, 2007.

[53] K. Edamatsu, G. Oohata, R. Shimizu, and T. Itoh, "Generation of ultraviolet entangled photons in a semiconductor," *Nature*, vol. 431, pp. 167-170, 2004.

[54] G. Oohata, T. Nishioka, D. G. Kim, H. Ishihara, and M. Nakayama, "Exciton polaritons in bulk CuCl microcavities grown by vacuum deposition," *physica status solidi (c)*, vol. 6, no. 1, 2009.

[55] G. Oohata, T. Nishioka, D. Kim, H. Ishihara, and M. Nakayama, "Giant Rabi splitting in a bulk CuCl microcavity," *Physical Review B*, vol. 78, no. 23, 2008.

[56] S. Faure, T. Guillet, P. Lefebvre, T. Bretagnon, and B. Gil, "Comparison of strong coupling regimes in bulk GaAs, GaN, and ZnO semiconductor microcavities," *Physical Review B*, vol. 78, no. 23, 2008.

[57] D. Kovalev, B. Averboukh, D. Volm, B. K. Meyer, H. Amano, and I. Akasaki, "Free exciton emission in GaN," 1996.

[58] A. K. Viswanath, D. Kim, C. R. Lee, and J. Y. Leem, "Exciton-phonon interactions, exciton binding energy, and their importance in the realization of room-temperature semiconductor lasers based on GaN," *Phys. Rev. B*, vol. 58, pp. 16333-16339, 1998.

[59] M. Watanabe et al., "Photoluminescence characterization of excitonic centers in ZnO epitaxial films," *Applied Physics Letters*, vol. 86, no. 22, p. 221907, 2005.

[60] A. Yamamoto, K. Miyajima, T. Goto, H. J. Ko, and T. Yao, "Bound Biexciton Photoluminescence in ZnO Epitaxial Thin Films," *physica status solidi (b)*, vol. 229, no. 2, pp. 871–875, 2002.

[61] D. van der Weide, "Applications and Outlook for Electronic Terahertz Technology," *Opt. Photonics News*, no. 4, pp. 49-53, 2003.

[62] L. Moller, J. Federici, A. Sinyukov, C. Xie, H. C. Lim, and R. C. Giles, "Data encoding on terahertz signals for communication and sensing," *Opt. Lett.*, vol. 33, no. 4, pp. 393-395, 2008.

[63] R. Piesiewicz, C. Jansen, D. Mittleman, T. Kleine-Ostmann, M. Koch, and T. Kurner, "Scattering analysis for the modeling of THz communication systems," *IEEE Transactions on Antennas and Propagation*, vol. 55, no. 11, pp. 3002-3009, 2007.

[64] Y. Kasai and T. Seta, "Terahertz-Wave propagation Model. Atmospheric Propagation Model of Terahertz-Wave," *JNIICT*, vol. 55, no. 1, pp. 73-77, 2008.

[65] A. Hofmann, E. Hörster, J. Weinzierl, L. P. Schmidt, and H. Brand, "Flexible low-loss dielectric waveguides for THz frequencies with transitions to metal waveguides," presented at the European Microwave Conference, Munich, pp. 955-958, 2003.

[66] L. J. Chen, H. W. Chen, T. F. Kao, J. Y. Lu, and C. K. Sun, "Low-loss subwavelength plastic fibre for terahertz waveguiding," *Opt. Lett.*, vol. 31, no. 3, pp. 308-310, 2006.

[67] S. Wang, W. Lu, X. Chen, Z. Li, X. Shen, and W. Wen, "Two-dimensional photonic crystal at THz frequencies constructed by metal-coated cylinders," *Journal of Applied Physics*, vol. 93, no. 11, p. 9401, 2003.

[68] N. Krumbholz et al., "Omnidirectional terahertz mirrors: A key element for future terahertz communication systems," *Applied Physics Letters*, vol. 88, no. 20, p. 202905, 2006.

[69] Y. Han et al., "Terahertz supermirrors," in *Infrared, Millimeter, and Terahertz Waves, 2009. IRMMW-THz 2009. 34th International Conference on*, pp. 1–2, 2009.

[70] A. L. Bingham and D. R. Grischkowsky, "Terahertz 2-D Photonic Crystal Waveguides," *IEEE Microwave and Wireless Components Letters*, vol. 18, no. 7, pp. 428-430, 2008.

2 CuCl material properties

2.1 Properties

Copper (I) chloride, commonly known as cuprous chloride is an ionic semiconductor of wide and direct band gap. CuCl shares many properties with other group I-VII semiconductors. The subgroup of I-VII semiconductors constitutes compounds of copper and one of the halogen gases, that is, copper halides. Of all the copper halides CuCl has the highest ionicity of 0.75 [1]. The iconicity is defined as an ionic (heteropolar) fraction (f_i^{α}) of the whole bond. The remaining fraction (f_h^{α}) is of the covalent (homopolar) origin. These fractions satisfy equation 2.1 [2]:

$$F_i^{\alpha} + f_h^{\alpha} = 1 \qquad (2.1)$$

The iconicity determines the crystalline structure of the compound [3]. The compounds of iconicity exceeding 0.785 crystallise in rock salt structure. CuCl is close to this border, though the lowest energy of the crystal is still achieved within the zinc blende structure at room temperature. Generally copper (I) halides crystallise in zinc blende (γ) phase at room temperature [4]. At some temperature, depending on the compound, they undergo a phase transition into the wurtzite phase (β). Further, with increasing temperature, copper (I) halides might undergo another phase transition into the cubic α phase. However, at normal pressure CuCl melts before it reaches α phase. With a band-gap energy (E_g) of 3.4 eV CuCl as a UV/visible light emitter is the natural competitor of other wide band-gap semiconductors like GaN or ZnO and their properties are compared in *Table 1*.

***Table 1**: Basic optical properties of wide band-gap semiconductors - GaN, ZnO and CuCl.*

Semiconductor	Band-gap energy [eV]	Exciton binding energy [meV]	Lattice mismatch with the compatible substrate [%]
GaN	3.28	25	~13
ZnO	3.37	60	18.2
CuCl	3.4	190	<0.4

CuCl has been a subject of research since at least the middle of the twentieth century. Early research was focused on absorption and luminescence of single crystals or bulk polycrystalline or amorphous layers grown on various substrates [5-11]. In 1968 the biexciton in CuCl was discovered [12] starting interest in this aspect of CuCl properties [11], [13], [14]. Also the

nonlinear optical properties were investigated [15], [16]. The progress in material fabrication technology moved attention into quantum confined structures of CuCl like quantum spheres, embedded CuCl microcrystals and thin layers [17-30].

The exciton in CuCl however, Wannier-type, has a small radius of 0.7nm, only slightly bigger than the γ-CuCl lattice constant of 0.541nm. Due to this, even nanometre size crystals or layers of CuCl exhibit bulk rather than a quantum confined nature. Quantum confinement of excitons influences their binding energies [31-33]. The increase in binding energy of excitons has crucial meaning for materials having low exciton binding energies in bulk. An example is the case of the GaN/AlGaN quantum well, where quantum confinement can increase the binding energy above 25 meV while in bulk this energy remains at 20 meV [32]. The room temperature thermal energy is 25.5 meV thus in order to be able to survive at room temperature excitons should have a binding energy of at least 25 meV. What is achievable only within quantum structures in materials like GaN is not an issue in CuCl. The free exciton binding energy within bulk CuCl is 190 meV [34]. Another significant feature with CuCl is its compatibility with a suitable substrate. As can be seen in *Table 1* the mismatch between CuCl and its substrate silicon is 0.4%. This value is approximately thirty times less than in the case of GaN and more than forty times less than for ZnO. Moreover, the most compatible substrate of GaN and ZnO is Al_2O_3. Both GaN and ZnO can also be grown on a Si substrate, but the increased lattice mismatch generates a huge number of threading dislocations that affect device performance, decreasing their longevity and overall efficiency. Even the mismatch of 13% in the case of the GaN/Al_2O_3 system requires sophisticated growth techniques like Epitaxial Lateral Overgrowth (ELO) in order to grow sufficient quality semiconductor layers [35-37]. Also with the progress of material fabrication experiments involving cavity-polaritons became possible [38], [39]. Since the biexciton binding energy in CuCl is very high and reaches 30 meV in bulk material, biexcitons were involved in Bose-Einstein Condensation (BEC) experiments [13], [40]. Also with the help of biexcitons in CuCl the emission of entangled photons was demonstrated [41].

In order to achieve satisfactory efficiency of photon generation in a light emitting device a p-n junction has to be built. The p-type doping was a problematic issue for wide band-gap semiconductors of groups III-V and II-VI [42], [43]. CuCl is natively a p-type semiconductor [44]. Zinc was proven to be an n-type dopant [45]. Oxygen is expected to increase the holes concentration in CuCl, thus the preliminary research on oxygen plasma treatment was done and will be discussed later [46].

The process of design and fabrication of a device has to be preceded and supported by simulation. Accurate and reliable simulation is possible only when valid parameters are provided with the correct model describing the phenomena involved. For simulation of light emitting

devices, the crucial parameters are optical properties of devices constituent materials. Later in this chapter the characterization of CuCl properties will be discussed. The excitonic properties of CuCl thin layers will be analysed with the help of temperature dependent photoluminescence (PL). The refractive index of CuCl polycrystalline layers deposited on Si substrates will be obtained from the analysis of ellipsometry measurements.

2.2 Sample preparation

The samples of copper (I) halides, being the object of optical characterisation, consist of a thin layer of CuCl or CuBr deposited on commercially available Si wafers. Layers of thickness up to 500 nm are deposited by the author. The evaporation is performed at room temperature in Edwards Auto 306A evaporator. The pressure inside the chamber is 10^{-6} Torr. The target, in the form of powder or small spheroids, is heated by the induction heater. The evaporation rate is controlled with the help of the crystal oscillator. Due to interactions with atmosphere, particularly with humidity, unprotected CuCl samples tend degraded to degrade very quickly. Thus, in order to guarantee the required quality, the freshly prepared samples were immediately transported to the cryostat and kept in vacuum all the time.

2.3 Measurements

2.3.1 XRD

Structural properties of CuCl on Si are determined with X-ray diffraction (XRD). CuCl and Si crystalline lattices are closely matched. The lattice constant, *a,* of CuCl is of 0.542 nm [47] while that of Si is 0.543 nm [48]. The mismatch between the two is <0.4% , thus the quality of CuCl films grown on Si is expected to be very high. The XRD spectrum of CuCl layer on (100) oriented Si is shown in *Figure 2.1.* The inset shows the rocking curve of the CuCl layer on (111) Si. In the XRD scan the sample is placed in the fixed position. The X-ray source is also fixed. The detector changes the angular position which is also known as 2θ scan. This measurement gives the information about the material composition. In the rocking curve scan the the X-ray source and the detector are at fixed position. The sample is tilted (or rocked) slightly around the Bragg peak. The rocking curve is also known as Ω scan since the tilt angle is often denoted as Ω. The rocking curve gives more detailed information about the crystalline quality of the material. There are 4 peaks identified. The most intense one is attributed to both CuCl (200) and Si, with the intensity mostly due to the Si contribution. Two other peaks attributed to CuCl are CuCl (111) and CuCl (220). The preferential direction of growth of CuCl on Si is (111), though both the (111) and (110) orientations allow the growth of good quality CuCl thin films. The rocking curve shows that the CuCl peak is very close to the Si peak, with only a small misalignment visible. Broadening near the base is an indication of the polycrystallinity of γ-CuCl grown on silicon.

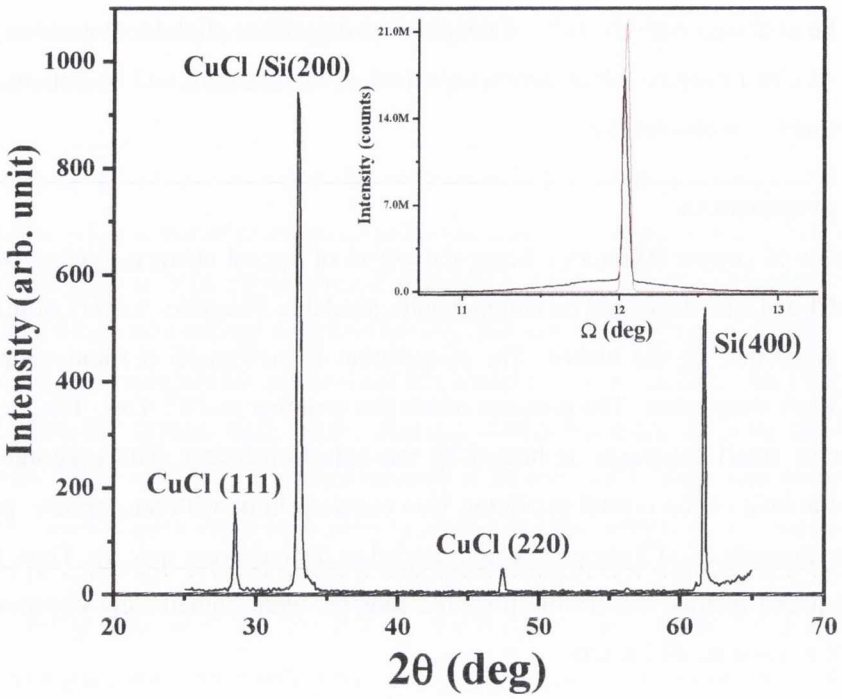

Figure 2.1: *CuCl on Si X-ray diffraction spectrum. There are three peaks corresponding to CuCl and two corresponding to Si visible. However at CuCl/Si (200) the most intense signal is detected it is mostly due to Si presence. The most intense CuCl peak is that of CuCl (111). The inset shows the rocking curve of CuCl on Si measured (black line) and simulated (red line). The broadening near the bottom of the measured line is an indication of CuCl polycrystallinity.*

2.3.2 Photoluminescence

A temperature dependent photoluminescence (PL) study of CuCl thin films was performed using the setup shown in *Figure 2.2*. A UV laser is used as the excitation source. The second harmonic (244 nm) of the continuous wave Ar-Ion laser and the third harmonic (355) of the pulsed Nd:YAG are available. The sample is held in a closed circulation liquid helium cryostat allowing the sample to be cooled down to 10K. Photoluminescence light is collected and focused by a set of lenses on the slit of a spectrometer equipped with a liquid nitrogen cooled CCD and connected to a computer for data collection. The spectral resolution of the overall system is 0.3 nm.

Figure 2.3 a shows typical low temperature spectrum of γ-CuCl deposited on (100) Si. A similar spectrum is obtained for CuCl on (111) Si.

There are four peaks visible. They are named and attributed as follows:

The highest energy peak (3.203 eV) Z_3 is attributed to the free exciton, I_1 at 3.181 eV is the bound exciton peak, at 3.159 eV there is the M peak attributed to free biexcitons and the lowest energy peak at 3.134 eV named N_1 is attributed to bound bi-excitons.

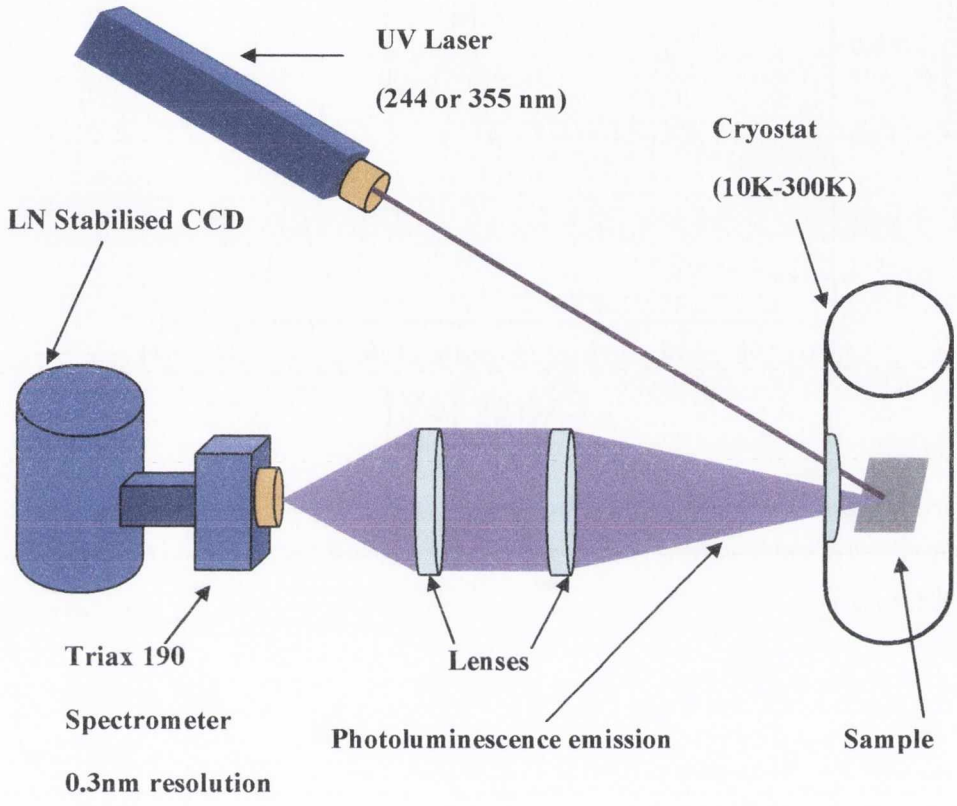

Figure 2.2: *Photoluminescence measurement setup. The source light is emitted by the laser. The sample hold in the liquid helium cooled cryostat is excited by the source light. The emitted radiation is collected by the set of lenses and focused onto the slit of the Triax 190 spectrometer having an optical resolution of 0.3nm. The resolved spectrum is recorded on PC computer with the help of LN stabilised CCD.*

In *Figure 2.4* the PL spectra of CuBr on Si are presented. The lattice constant of CuBr of 0.5695 nm is bigger than that of CuCl (0.542 nm) and Si (0.543 nm). Thus the lattice mismatch between CuBr and Si lattice is of ~4.7%. The sample was excited with the 355 nm pulsed Nd:YAG laser. Similar to CuCl, the exciton emission in CuBr has two bands separated by spin-orbit splitting. These bands are named $Z_{1,2}$ and Z_3 in both semiconductors. In CuCl Z_3 is the highest energy band while in CuBr the order is reversed with $Z_{1,2}$ the highest energy band [11].

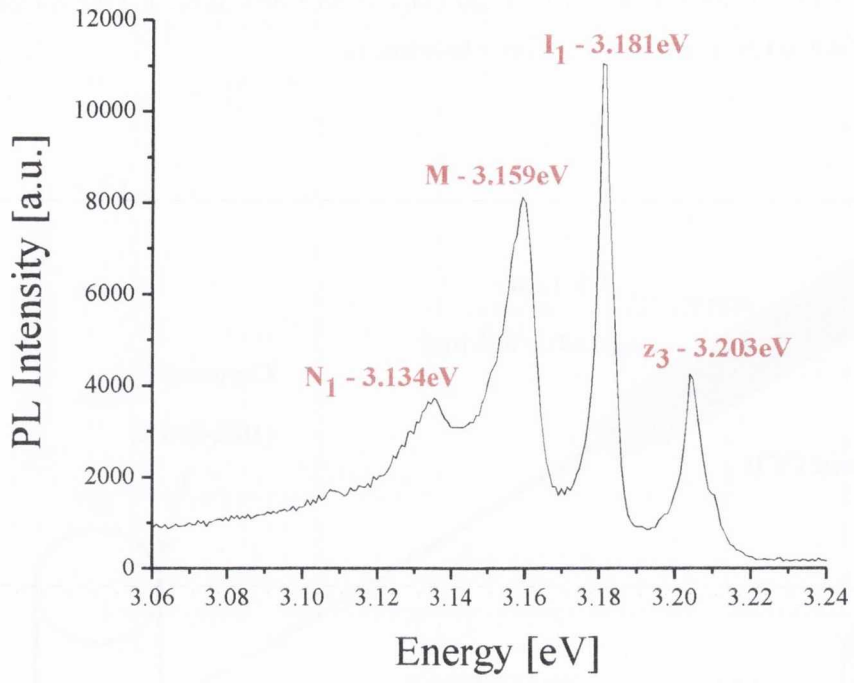

Figure 2.3: *Low temperature (14K) PL spectrum of CuCl on Si. There are four distinguishable features attributed to free and bound excitons(z_3 and I_1, respectively) and free and bound biexcitons (M and N_1, respectively).*

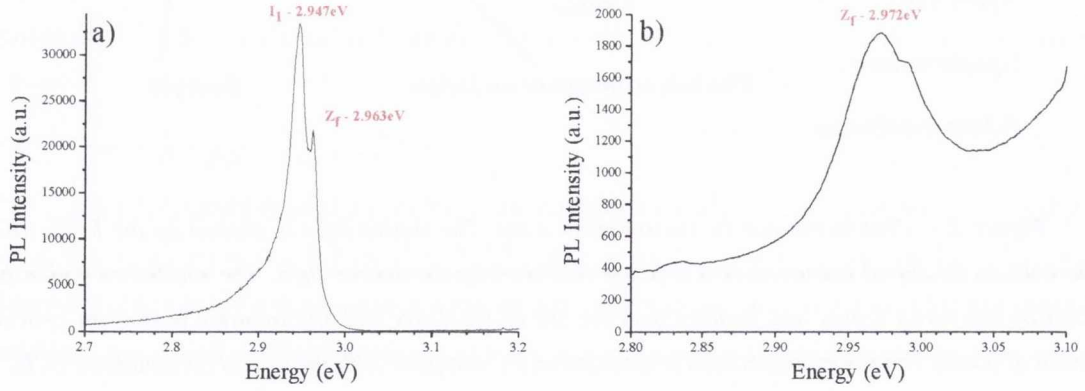

Figure 2.4: *CuBr PL spectra taken at 14K (a) and at room temperature (b).In the low temperature spectrum only the excitonic peaks are visible, at 2.963 eV the free exciton (z_f) peak and at 2.947 eV the bound exciton (I_1). At room temperature the bound exciton peak vanished and only one feature at approximately 2.972 eV is visible.*

There are two distinguishable peaks in the low temperature spectrum. The dominant bound exciton I_1 peak at 2.947 eV and the low energy side of free exciton $Z_{1,2}$ known as Z_f at 2.963 eV. At high temperatures the I_1 peak vanishes and the Z_f peak, which is thermally promoted to higher energies, merges with $Z_{1,2}$ thus only one feature is visible at 2.972 eV. These observations are consistent with previously reported spectra of CuBr single crystal samples [11].

According to the observed peaks positions presented in

Figure 2.3 the energy level diagram of CuCl is presented in figure 2.5 and the binding energies of individual exciton peaks can be determined.

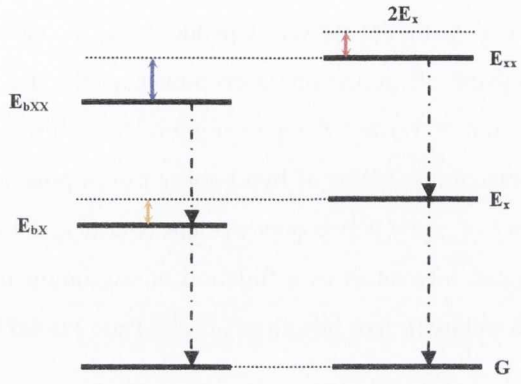

Figure 2.5: *Energy levels of CuCl.*

The energy values from the different peaks of the CuCl on Si photoluminescence spectrum taken at 14K are $E_X[Z_3]$=3.203 eV, $E_{XX}[M]$=3.159 eV, $E_{bX}[I_1]$=3.181 eV and $E_{bXX}[N_1]$=3.134 eV and the binding energies of bound excitons and biexcitons can be derived as follows:

bound exciton binding energy (marked with the orange arrow): $E^b_{bX}=E_X-E_{bX}$

free biexciton binding energy (marked with the red arrow): $E^b_{XX}=2E_X-E_{XX}$

bound biexciton binding energy (marked with the blue arrow): $E^b_{bXX}=2E_x-E_{bXX}-E_{bX}-E^b_{XX}$

The binding energy of the bound exciton E^b_{bX}=22±2 meV corresponds to the value previously reported for bulk CuCl crystals and to the layers deposited on sapphire substrate [17]. The line shape of free biexciton in CuCl is known to be of an inverse Boltzmann type. Assuming that the bound biexciton binding energy is 33 meV, as in bulk CuCl, the bound biexciton peak is expected at 4.174 eV which in fact is the high energy edge of the M peak [17].

2.3.3 Power dependence of PL emission

Very even energy separation of Pl peaks suggests that M and N_1 can be rather phonon replicas not biexcitons [49]. However, in the CuCl on Si samples under study, there are a number of features mitigating against this argument. Firstly, as the LO phonon energy in CuCl is typically 26 meV, the lower energy peaks are not at appropriate energies to correspond to phonon replicas of the Z_3 or I_1 exciton peaks. Secondly, the high intensities of the M and N lines with respect to the free and bound exciton peaks in the 10K spectrum, shown in figure 2, are not consistent with phonon replicas. Thirdly, due to the increased LO phonon-exciton interaction at higher temperatures the ratio of the LO phonon line intensity to the zero-phonon line intensity should

increase as a function of temperature and there is no evidence of this in the temperature dependent spectra in *Figure 2.8*.

The analysis of individual peak intensities as a function of excitation power helps to attribute them to the particular features. The biexcitonic origin of peaks at 3.159 eV (M) and 3.134 eV (N_1) was further confirmed with the power dependent PL measurements. Biexciton peak intensity increases as the square of excitation laser power while the excitonic peak intensity increases linearly with the excitation power. Such a simple relationship is however rarely observed in practice [18], [19]. An approximate factor of two between both power dependences is a typical signature of bi-excitonic behavior, even if it is only evident over a small range of excitation power [19]. *Figure 2.6* shows the peak intensities as a function of excitation power plotted for the free exciton peak Z_3 (marked with squares), free biexciton (circles) and bound biexciton (triangles).

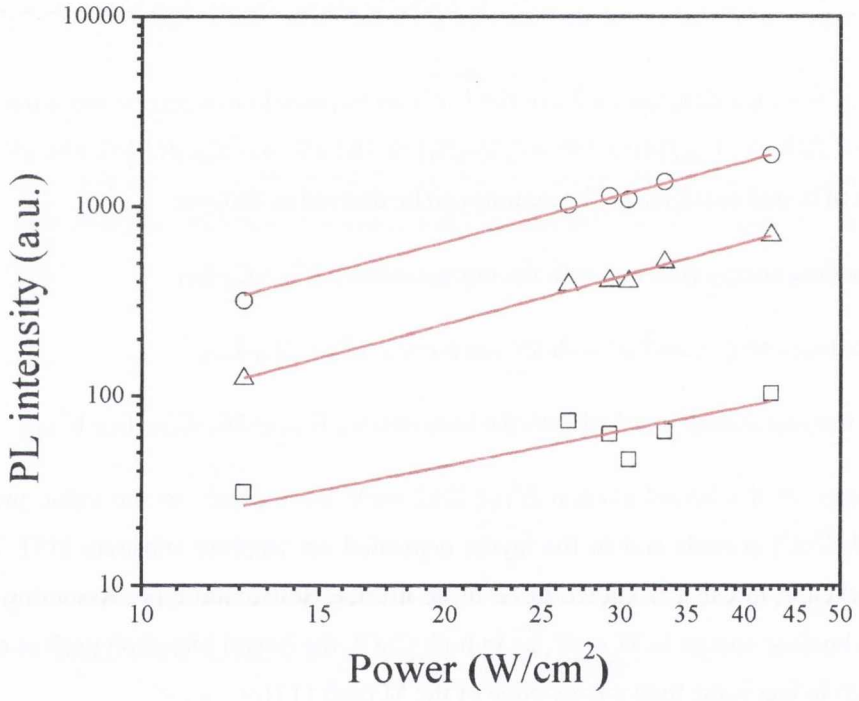

Figure 2.6: *Power dependence of CuCl on Si photoluminescence. Intensities of the Z_3 peak are marked with squares, free biexcitons and bound biexcitons are marked with circles and triangles, respectively. The exponential dependence of emission intensity on excitation power allows determining the origin of the peaks. The exponents of free and bound biexcitons are of 1.45±0.08 and 1.4±0.1, respectively. The exponent of free exciton peak is of 0.86±0.38. The difference between the biexcitonic and excitonic peaks power dependence of the level close to the unity confirms the origin of these features.*

The power range is almost two orders of magnitude lower than in other studies on biexcitons. However, the laser used in the experiment is emitting at 244 nm, where the absorption of CuCl is more efficient than in the case of the 355 nm or 337 nm lasers that are used in similar

studies [50]. Also very good quality of CuCl layer grown on Si allows for biexciton appearance under relatively low excitation power. The measured power dependence was 1.45±0.08 for the free biexciton and 1.4±0.1 for the bound biexciton. The Z_3 peak power dependence on excitation power was 0.86±0.38. These values confirm the biexcitonic nature of M and N_1 peaks.

The free exciton (Z_3) peak position changes with temperature. This dependence is shown in *Figure 2.7*. The peak position varies between 3.205 eV at 10K and 3.235 eV at room temperature. The increase of band gap energy as a function of temperature is the opposite to other semiconductors, which generally follow the Varshni or Einstein model [51], [52]. Similar results have been previously reported for vacuum evaporated CuCl thin films on fused quartz substrates [53]. To explain the behavior Garro *et al* [54] postulated that the Cu ions, vibrating predominantly at low frequencies, lead to an increase in the energy gap, whereas the Cl ions, vibrating at high frequencies, lead to a reduction in the energy gap. The effect of the Cl ions is seen at higher temperatures when the competition between the processes results in a reduction in the rate of increase of the band gap energy as a function of temperature.

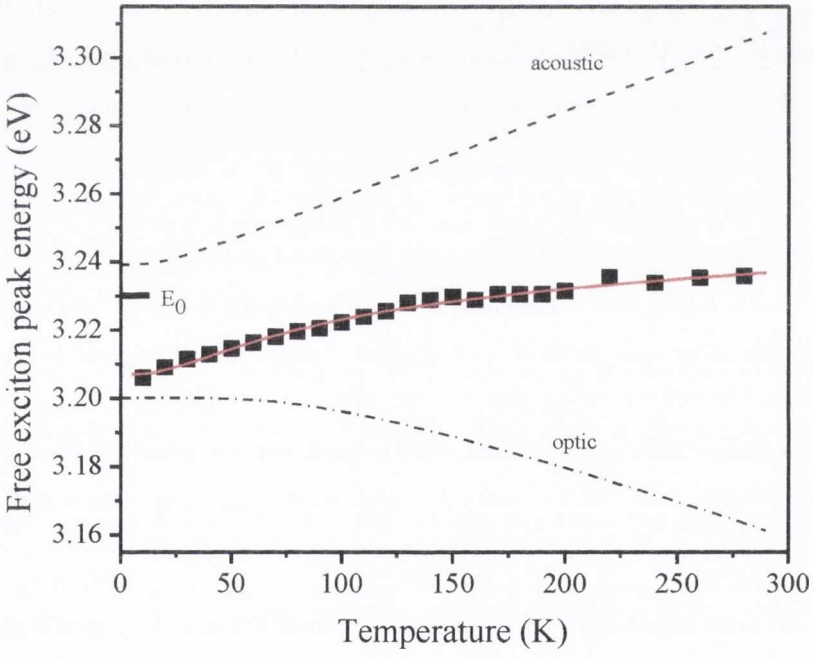

Figure 2.7: *Z_3 peak thermal shift in CuCl on Si. The measured energies of z_3 peak are marked with black squares. The dashed and dash-dotted lines represent the competing vibrations (acoustic and optic, respectively) leading to the thermal shift of the free exciton peak according to the Göbel model.*

Göbel *et al.* proposed a two harmonic oscillator model to describe the renormalization of the CuCl band gap by electron-phonon interaction [55]. Due to the relatively large mass difference between Cu and Cl, one oscillator describes purely chlorine-like vibrations at high (optic)

frequencies and the other purely copper-like vibrations at low (acoustic) frequencies. The following expression describes the mass and temperature dependence of the fundamental gap:

$$E_0(T,M) = E_0 + \frac{A_{Cu}}{\omega_{Cu} M_{Cu}}\left[n(\omega_{Cu},T) + \frac{1}{2}\right] + \frac{A_{Cl}}{\omega_{Cl} M_{Cl}}\left[n(\omega_{Cl},T) + \frac{1}{2}\right] \quad (2.2)$$

where, $n(\omega,T) = \frac{1}{e^{\frac{\hbar\omega}{kT}}-1}$ is the Bose-Einstein occupation number of the phonon. $M_{Cu/Cl}$ is the atomic mass of Cu/Cl, E_0 is the unrenormalised band gap and $A_{Cu/Cl}$ is an effective electron-phonon interaction parameter. As in references [51] we take an average optical, purely Cl-like, phonon frequency of ω_{Cl}=6 THz and an average acoustic, purely Cu-like, phonon frequency of ω_{Cu}=1 THz. This equation results in an excellent fit with our experimental data as shown in *Figure 2.7*. Values for E_0 and the $A_{Cu/Cl}$ parameters were determined: E_0=3.233±0.002 eV, A_{Cu}= 0.0032±0.0001 eV^2 amu, A_{Cl}= –0.057±0.004 eV^2 amu. By looking separately at the contributions of each of the two oscillators to the renormalization of the band gap energy we can determine that the optical, chlorine-like vibration reduces the unrenormalised band gap at 0 K by 33 meV while the acoustic, copper-like vibration increases the gap by 6 meV resulting in an overall 0 K band gap renormalization of 27 meV. These values are slightly smaller than those obtained by Göbel *et al.* of 38.8 meV and 8.7 meV for the optic and acoustic phonon contributions respectively.

The thermal dependence of PL emission from CuCl on Si is presented in *Figure 2.8*. While at low temperatures all previously named features are visible the shape of the PL spectrum changes as the temperature is raised, some of the spectral features disappear due to thermalization of (trapped) carriers. As their binding energies are lower than excitons, biexcitons disappear first. Finally at room temperature only the free exciton peak remains (inset of *Figure 2.8*) since free exciton binding energy (190 meV) is much higher than room temperature thermal energy (25 meV).

By analysing the peak intensities and widths more information regarding optical properties can be extracted. *Figure 2.9* presents the so-called Arrhenius plot of the normalised integrated photoluminescence intensity as a function of T^{-1}.

Several factors can induce luminescence quenching in semiconductors [56]. One of them is related to temperature quenching in which the lower state for radiative transition may become unavailable or an alternative nonradiative path for energy transitions can become available so that even if the number of excited centers remains constant the probability of radiative transition is reduced. The following equation can be used to study the thermally activated process leading to exciton (or biexciton) luminescence quenching.

$$I_{ex}^{peak} = \frac{I_0}{1 + Ae^{\frac{-E_i}{k_b T}}} \qquad (2.3)$$

I_0 is the photoluminescence integrated intensity at 0K, A is a constant, E_i is the thermal activation energy, k_B is the Boltzmann constant and T is the temperature. From the data presented in *Figure 2.9*, a free exciton thermal activation energy of 167.8±6.5 meV can be estimated for CuCl layer evaporated on Si. It is within the range of previously reported values for bulk CuCl and CuCl thin films (150-250 meV) [7].

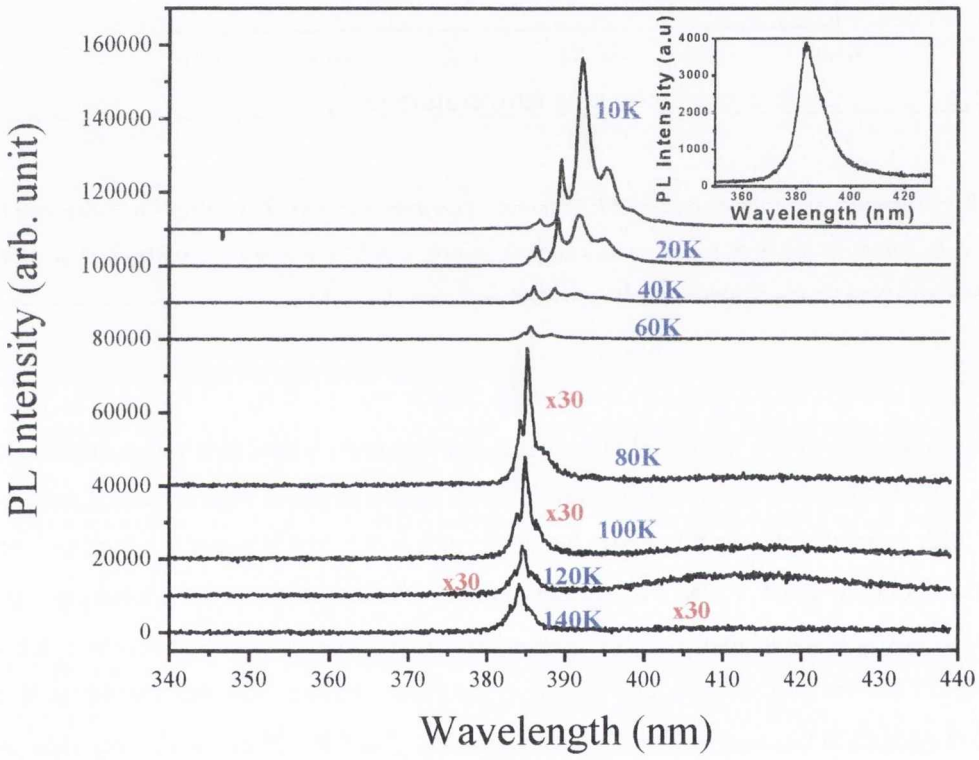

Figure 2.8: *Thermal dependence of CuCl on Si PL emission. There are four clearly distinguishable features visible in the 10K spectrum. Due to thermal quenching and exciton-phonon interactions intensities decrease with temperature and peaks become broader. Spectra for temperatures between 80 and 140K were multiplied by the factor of 30 for the sake of clarity. An inset shows the room temperature spectrum where only one peak, z_3 remains present.*

An understanding of the exciton-phonons coupling can be further elucidated from analysis of the PL line broadening study as a function of temperature. Whether excitonic emission would be visible at room temperature or not depends on the balance between exciton binding energy on one hand and exciton-phonon coupling strength on the other hand [18].

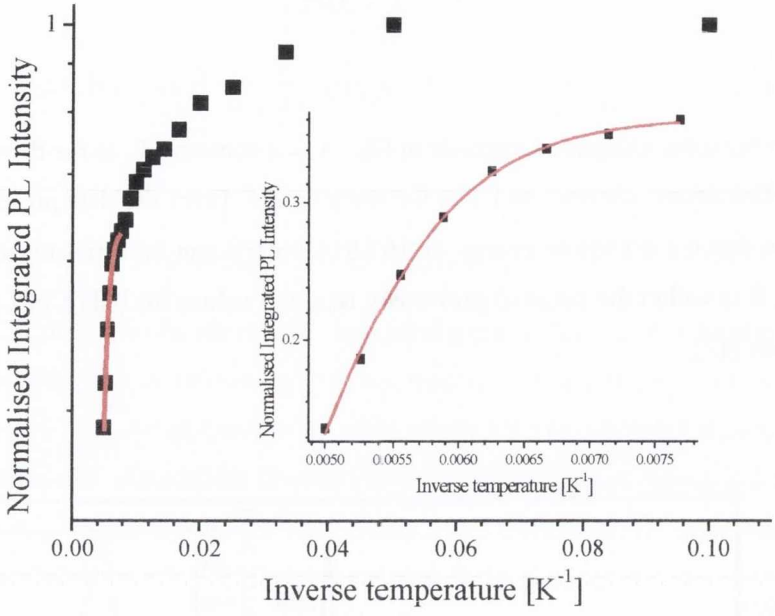

Figure 2.9: *Arrhenius plot of the normalised PL intensity vs temperature for Z_3 peak of CuCl deposited on Si. In the inset the zoom for the high temperature range is shown. Over the measured points marked with black squares the curve fitted using equation (2.3) is plotted with the solid red line.*

A high value of the exciton–LO phonon coupling parameter leads to an increase of the linewidth with temperature such that it might not be visible at room temperature. Interaction of excitons with acoustic phonons linearly broadens the line. This process is dominant at low temperatures, but at about 150K exciton/LO-phonon interaction starts to contribute. At high temperatures (close to room temperature) exciton/acoustic phonon interaction becomes dominant. Depending on the exciton binding energy value, excitonic features can be visible up to room temperature such as in the case of CuCl. *Figure 2.10* shows the FWHM of the Z_3 peak (assigned to free exciton emission) as a function of temperature. The black squares correspond to the experimental data.

The experimental data are fitted with the following equation

$$\Gamma(T) = \Gamma_0 + \gamma_{ph} T + \frac{\Gamma_{LO}}{e^{\frac{n\hbar\omega_{LO}}{k_b T}} - 1} \qquad (2.4)$$

where Γ_0 is the FWHM at 0K, γ_{ph} the acoustic phonon coupling constant, Γ_{LO} the coupling strength with longitudinal optical phonons, n the number of optical phonons involved and $\hbar\omega_{LO}$ the

optical phonon energy, with k_B and T representingthe Boltzmann constant and temperature, respectively. The final curve is the sum of three components: a constant corresponding to the FWHM at 0K, a linear part (describing the interaction of excitons with acoustic phonons which is dominant at low temperatures) and an exponential part (describing the interaction of excitons with optical longitudinal phonons becoming dominant at high temperatures).

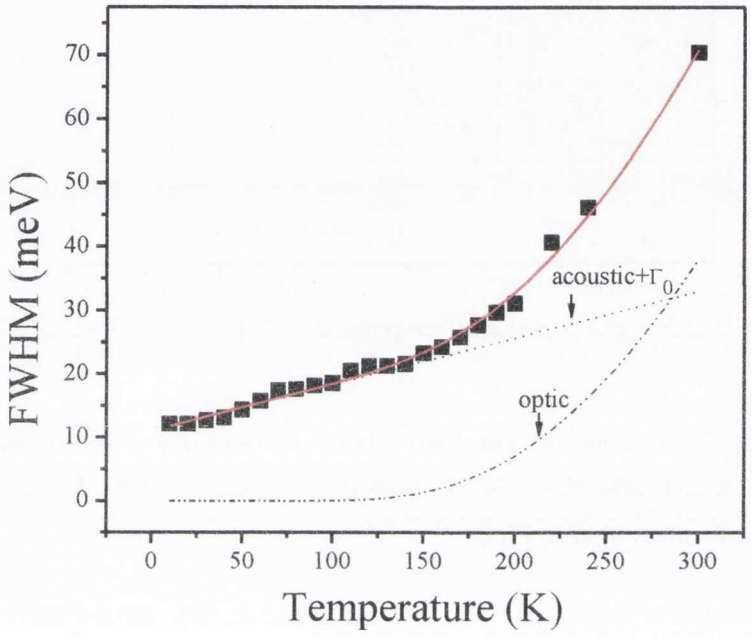

Figure 2.10: *FWHM of Z_3 peak in CuCl on Si sample excited with 244 nm CW laser. The red curve shows the fit obtained with the equation (2.4). The dotted curve shows the linear component corresponding to the exciton-acoustic phonon interaction while the dash-dotted line shows the exponential component describing exciton-longitudinal optical phonon interaction. The slight 'stepping' visible in the measured data points originates in limited accuracy of resolving PL spectra, especially at low temperatures, where spectra become quite complex.*

Our data can be fitted with an excellent agreement using the parameters: $n\hbar\omega_{LO}$=84.8±6.8 meV, γ_{ph}=73±7 μeV, Γ_{LO}=976±245 meV and Γ_0 =11.1 ±0.5 meV. The PL lines of CuCl z_3 exciton were fitted with the Lorentzian. For each temperature step in the range 14-300 K the FWHM was read. As Γ_{LO} is expected to increase with the polarity of the material and because CuCl ionicity is higher than that of ZnO or GaN, the obtained value for CuCl is in agreement when compared with previously reported values for the two other wide band-gap semiconductors (Γ_{LO} (ZnO)=876.1 meV) [57].

Similar analysis can be performed on the CuBr spectra. The Arrhenius plot for CuBr deposited on Si is shown in *Figure 2.11*.

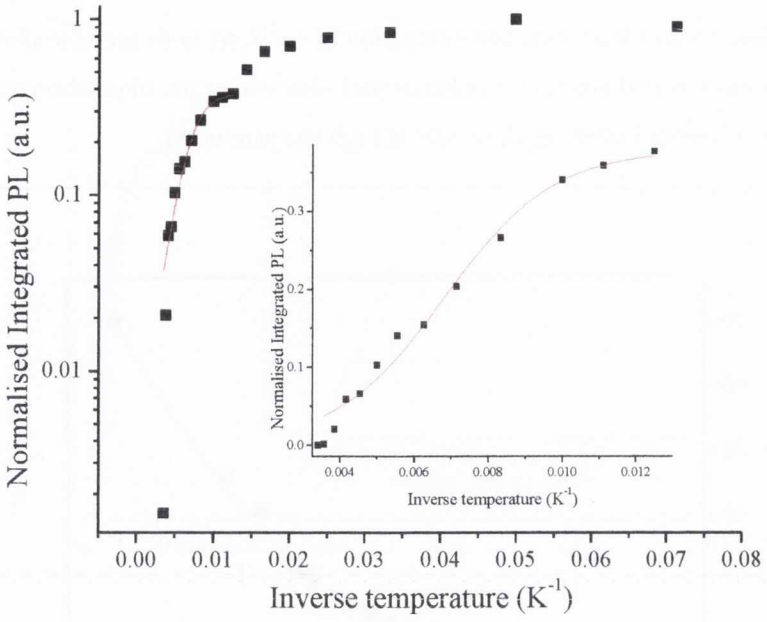

Figure 2.11: *Arrhenius plot of Z_f peak for CuBr deposited on Si. In the inset the high temperature part of the spectrum is zoomed. The red curve shows the fit obtained using equation (2.3) plotted over the black squares representing the measurement points.*

Again, the experimental data were fitted using the *equation (2.3)*. The thermal activation energy of the photoluminescence quenching process (E_i) for CuBr on Si was calculated as 59±7 meV. This value is consistent with previously reported values of 50 meV for single crystal CuBr [7].

The Z_f peak width as a function of temperature is presented in *Figure 2.12*. The experimental data corresponds to the FWHM of the free exciton peak over the temperature range 14 K to 293 K using the Nd:YAG 355 nm pulsed laser as the excitation source. The data are fitted with e*quation (2.4)* and the following parameters are obtained:

Γ_0 = 4.38 ±0.55 meV, Γ_{LO} = 50.45±4.33 meV, $n\hbar\omega_{LO}$=17.99±2.1 meV while γ_{ph}=37.4±19.5 μeV for CuBr on Si. Similarly to CuCl on Si case, interaction with acoustic phonons is much weaker than with optical phonons. The lower value of γ_{ph} for CuBr is consistent with expectation, as the deformation potential is also lower in CuBr than in CuCl [58]. The measured value of the optical phonon energy of 17.9±2.1 meV is comparable to literature data for CuBr which is of ~21 meV [59], [60]. Also the coupling strength between the exciton and LO phonon is much weaker in CuBr than in CuCl. This value is expected to increase with polarity, thus lower value for CuBr is expected.

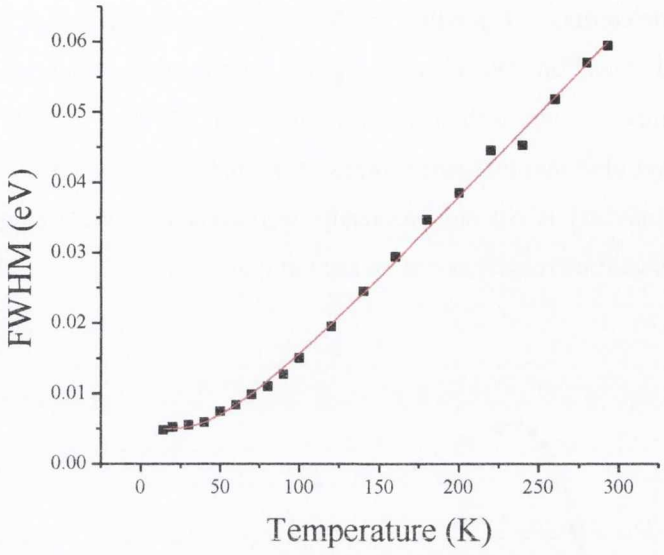

Figure 2.12: *Z_f peak width as a function of temperature in CuBr on a Si sample excited with 355 nm Nd:YAG pulse laser. The black squares represent the measured values of z_3 peak FWHM. The red line is the fit of equation (2.4).*

The parameters obtained from the thermal analysis of PL emission are very helpful. Together with XRD they allow assessment of the material quality. Comparison with the reported data of single crystals and thin layers evaporated on other than Si substrates gives the information about the overall quality and properties of copper halide layers grown on Si. Obtained PL spectra of sharp and well defined features and material parameters comparable to those reported in literature, even for single crystal CuCl, provide high quality evidence of vacuum deposited layers on the Si substrate.

2.3.4 Oxygen treated CuCl on Si layers

One of the issues that has to be addressed before the p-n junction can be fabricated is material doping. As was already reported, CuCl is natively a p-type semiconductor. Zn has been investigated as a possible n-type dopant [45]. On the other hand doping with oxygen is expected to increase the hole concentration in CuCl. The oxygen plasma treatment is examined as a possible oxygen doping technique for CuCl and possibly for other copper (I) halides. For the purpose of the experiment the vacuum deposited CuCl on Si layers were treated in an RF oxygen/argon plasma. Ar is a neutral gas and thus it does not react with CuCl. High energy Ar ions penetrate CuCl deeper than oxygen ions. The Ar penetrated CuCl layer is thus doped not only at the surface, but also to some extent deeper. A number of oxidized CuCl samples were prepared to examine optical properties of such modified CuCl. 500 nm of CuCl on Si substrate samples were prepared using the evaporation technique mentioned before. Such samples were oxygen plasma treated for periods

varying from 30s up to 5 minutes. Temperature dependent PL was performed on each sample. A PL spectrum is a result of one or more possible energy transitions in the material. Radiative transitions give a positive contribution to the photoluminescence while non radiative transitions may be considered as deleterious. Depending on the band structure of the crystal there could be more than one allowed transition. With increasing temperature the probability of non-radiative transitions becomes higher, leading to the previously mentioned thermal quenching process. From the normalized integrated photoluminescence intensity plotted versus T^{-1} of oxidized samples we can notice that the PL intensity is not monotonically decreasing with increasing temperature, but for some temperature range it increases, as can be seen in *Figure 2.13*.

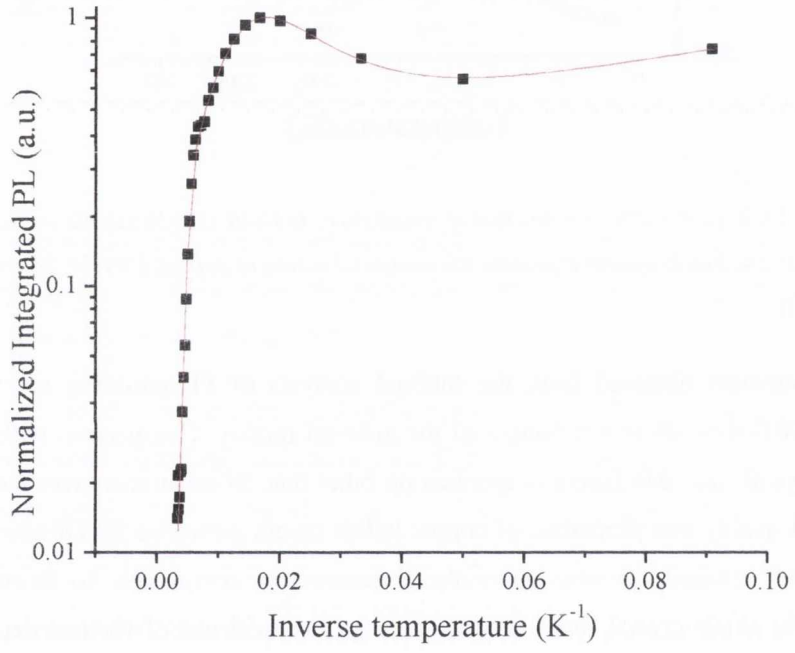

Figure 2.13: *Z_3 peak thermal quenching of plasma treated CuCl on Si sample. The black squares show the measurement points. The red curve is the fit of equation (2.5) assuming that there are four processes involved. Three of them contribute to thermal quenching and one of them drives the negative thermal quenching visible as the dip in the fitting curve.*

An explanation of this phenomenon was proposed by Shibata *et al* and applied to GaAs [61]. He suggested the existence of energy transitions leading to thermal activation of electrons from some inner energy level to an excited level. Transitions from this inner level would be non-radiative while transitions from the excited level to the ground level are radiative. The schematic diagram of this model is presented in *Figure 14*. The transition from the excited energy level (denoted as A) to the ground level (G) are radiative. The transitions between the excited level and inner levels (B1-Bw) can be both radiative and nonradiative. The temperature induced transition from the

potentially nonradiative level B2 to the excited level contributes to the increased PL intensity with increased temperature.

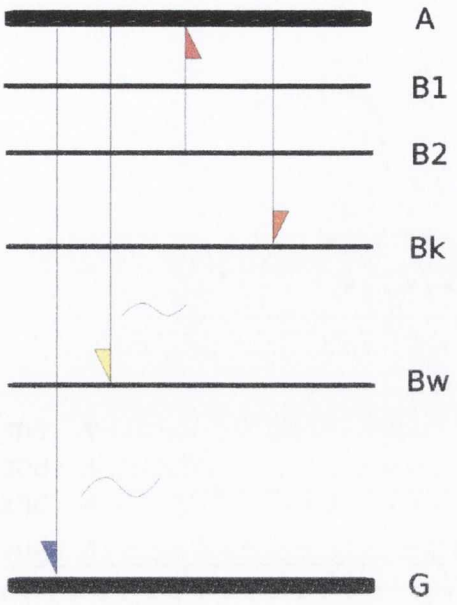

Figure 14: *The scheme of energy transitions in oxygen plasma treated CuCl on Si. The number of new, both radiative and nonradiative, transitions is introduced. Additionally the temperature activated transitions from inner levels to the excited level become possible.*

Thus for some temperature range over which the thermal energy is sufficient to excite the electron an increase of the PL intensity with temperature called Negative Thermal Quenching (NTQ) is observed. Mathematically this model is described by *equation (2.5)* [61].

$$\frac{I(T)}{I(0)} = \frac{1 + \sum_{q=1}^{w} D_q e^{\frac{-E'_q}{k_B T}}}{1 + \sum_{j=1}^{m} C_j e^{\frac{-E_j}{k_B T}}} \qquad (2.5)$$

In *equation (2.5)* the numerator is the sum of w terms attributed to the processes responsible for negative thermal quenching. E_q is the q^{th} process thermal activation energy. The denominator is the sum of m processes contributing to thermal quenching. E_j is the j^{th} process thermal activation energy. D and C are fitting constants. T is the temperature and k_B is Boltzmann constant. If the number of processes contributing to NTQ is 0 (w=0) and only one process contributes to PL quenching (m=1) this equation simplifies to the previously mentioned Arrhenius *equation (2.3)*. Assuming there are 3 processes contributing to the thermal quenching of PL of oxidized sample, and one process contributing to NTQ a very good fit to the experimental data could be obtained, as can be seen in *Figure 2.13*. From fitting the experimental data the activation energy of the NTQ process of approximately 10 meV for all of the measured samples was obtained. It was also noticed that the ratio of PL intensity at low temperature to that at room temperature decreases with

oxidation time. Plots of normalized integrated photoluminescence intensity as a function of T^{-1} showing the difference caused by the oxygen plasma exposition time are shown in *Figure 2.15*.

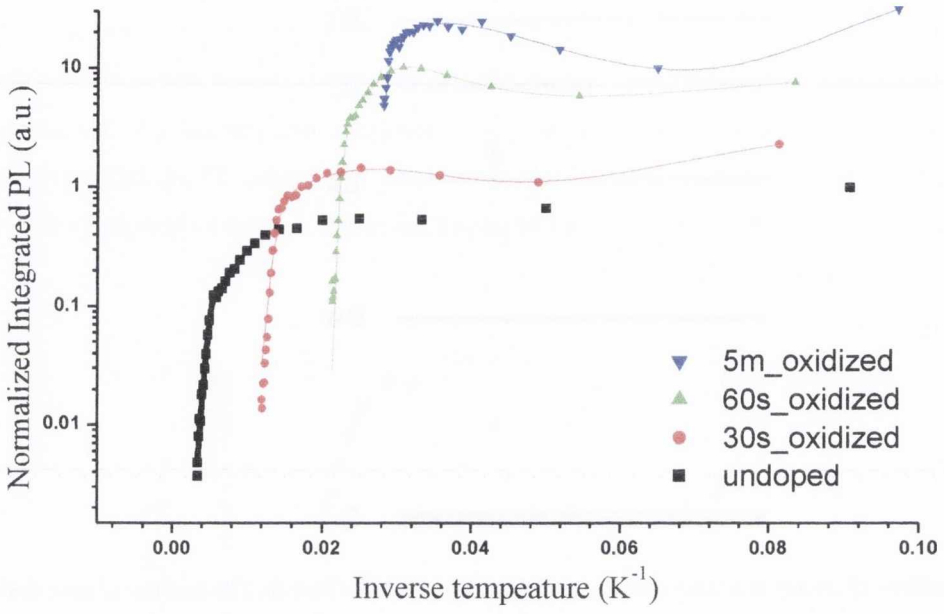

Figure 2.15: *PL intensity dependence on oxidization time. Curves of 30s-5m are vertically shifted in order to emphasize differences. Increased oxidization time has twofold impact on thermal quenching. The negative thermal quenching becomes more significant and the PL intensity decreases.*

Optical properties of CuCl are affected by the plasma treatment. The intensity decreases with an increasing of oxidation time, but it is not quenched completely. The activation energy of additional non-radiative processes was determined and this suggests that the number of defects in the CuCl layer had increased. However the photoluminescene signal remained relatively high. Electrical measurements are required to validate the increase of hole conductivity. Also doping with other elements (like Sr or Ba) could be investigated to modify the electrical properties of CuCl and determine the optimum dopant.

Structural and optical measurements show that room temperature vacuum evaporation can give a good quality material using this relatively simple growth technique. Values of optical parameters were measured and compared with those reported for single crystal CuCl and for Cu-Ha layers grown on other substrates.

Of course more advanced growth techniques like MBE would allow more precise control over thickness and overall material quality, i.e. improve the epitaxial quality. Our collaborators are currently developing liquid phase epitaxial growth of CuCl on Si. It will allow single crystal layer of CuCl to be grown on Si. And to investigate the rest of the copper halides group, CuBr and CuI.

2.3.5 CuCl refractive index determination from ellipsometry data

The growth of more sophisticated structures leading ultimately to CuCl based optoelectronic devices requires simulations to investigate different device design options. The complex refractive index, $\tilde{n}$, is a key parameter required for accurate simulation of the propagation of electromagnetic fields in multilayer structures. For many materials values of refractive index are known for a wide range of wavelengths. Available data for CuCl is rather incomplete [62], [63]. Other authors give the absorption coefficient of CuCl obtained from low temperature measurements [64] or some just show the shape of the absorption curve but give no quantitative values [65]. Only one publication describes the dielectric constant of CuCl around the band-gap at room temperature [66]. The refractive index is not only temperature dependant, but also depends on material quality. Moreover, the refractive index strongly depends on the growth technique. More precisely, the refractive index depends on the material quality. The imaginary part of the refractive index remains sharp for good quality epitaxial materials. Structural distortions broaden the absorption line and thus the real part of the refractive index becomes flattened.

In order to guarantee the highest possible accuracy of simulation the refractive index of vacuum evaporated CuCl on Si is determined at room temperature using ellipsometry. This section presents the technique and results of the measurement of the refractive index of CuCl on Si for a wide range of wavelengths including the proximity of the band-gap. This optical parameter is then used for the simulation of microcavity structures in Chapters 4 and 5.

2.3.5.1 The ellipsometry technique

The ellipsometry is a sensitive technique which allows the polarization state of reflected light to be measured. Such reflected light is decomposed into its two components: s (perpendicular) and p (parallel) to the plane of incidence. The measured parameters Ψ and Δ are related to the ratio of reflected amplitudes by the equation:

$$\rho = \frac{r_p}{r_s} = \tan(\Psi)e^{i\Delta} \qquad (2.6)$$

Where r_p and r_s are the Fresnel reflection coefficients (respectively parallel and perpendicular to the incidence plane).

Typical Ψ and Δ values have been obtained for a sample with 500 nm of CuCl deposited on Si and are presented in *Figure 2.16*.

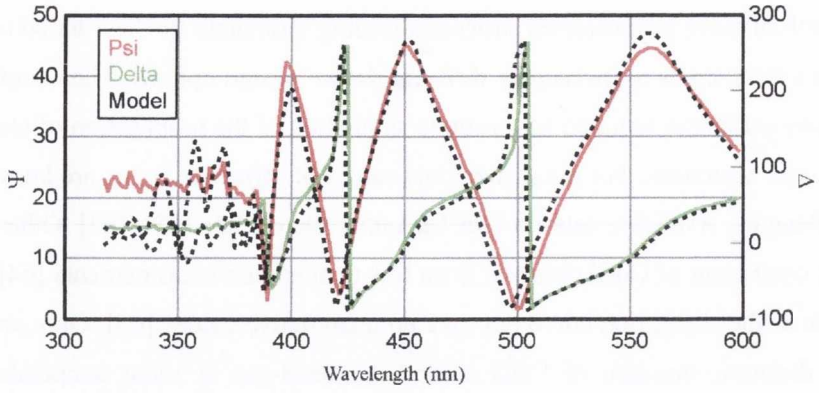

Figure 2.16: *Ellipsometry data of 500 nm CuCl on Si layer. The dotted lines represent the measured ellipsometric angles while the solid lines represent the modeled Ψ and Δ using the 'guessed' refractive index.*

The red and green lines show the experimental values of Ψ and Δ given in degrees. Dotted lines show fitted curves using modelled values of n and k. It can be seen that the fit is very close the measured data for the energies below the band-gap at room temperature (3.39 eV) which corresponds to wavelengths > 365 nm. For energies > 3.39 eV there is significant absorption which makes it difficult to detect the oscillations.

There are different mathematical models to describe the dispersion of the dielectric constant in different types of materials. Most of them are quite reliable for energies below the band-gap. The model chosen to model dielectric constants of the measured samples was the Tauc-Lorentz model, in particular it was used to extract the complex refractive index below the band-gap [67]. Components of the complex dielectric function in this model are calculated as follows:

$$\varepsilon_2 = \begin{cases} \dfrac{AE_0C(E-E_g)^2}{(E^2-E_0^2)+C^2E^2}\dfrac{1}{E} & E > E_g \\ 0 & E < E_g \end{cases} \tag{2.7}$$

And

$$\varepsilon_1 = \varepsilon_1(\infty) + \frac{2}{\Pi}P\int_{E_g}^{\infty}\frac{\xi\varepsilon_2(\xi)}{\xi^2-E^2}d\xi \tag{2.8}$$

Where A is a transition-matrix related parameter, C is the broadening parameter, E_0 is the transiotion energy, E_g is the band-gap energy and $\varepsilon_1(\infty)$ is the dielectric constant.

It is a modified version of the Lorentz model.

$$\tilde{\varepsilon}(E) = \varepsilon_1(\infty) + \sum_{i=1}^{N} \frac{A_i}{E_k^2 - E^2 - iB_iE} \tag{2.9}$$

Where $\tilde{\varepsilon}(E)$ is a complex dielectric constant, $\varepsilon_1(\infty)$ is dielectric constant at high energies (over the band-gap), N is the number of oscillators, A_i is the amplitude of the ith oscillator, B_i is the broadening of the ith oscillator and E_k is the center energy of ith oscillator.

The Tauc-Lorentz model can be used to describe the dielectric constant around the band gap and below. However while this model is widely used with amorphous semiconductors, it did not provide a good fit for our pollycrystaline CuCl on silicon samples. The Tauc-Lorentz model was applied for energies below the band-gap. However to extract the complex refractive index close to or greater than the band-gap a point-by-point method was used to obtain discrete values of the dielectric constant.

2.3.5.2 CuCl on Si refractive index values

High absorption coefficients near and above the band-gap make ellipsometry signals weak for samples of thickness exceeding 120 nm. Signal strength increases with decreasing CuCl layer thickness, but surface roughness starts to play a significant role for samples thinner than 60 nm. Average surface roughness measured with a Dek-Tak profilometer is ~7 nm. Based on these factors a range of sample thicknesses ranging from 60 – 120 nm were characterized and analysed. Subsequently the data from the samples were combined to obtain the averaged complex refractive index over the entire wavelength range. The curves in *Figure 2.17* represent the averaged complex refractive index. The real part of refractive index (n) is shown with an absolute error of less than 0.0925 (~4.7%) and the imaginary part (k) is shown with an absolute error less than 0.092 (~18.9%). In the ranges where data was available, the refractive index of CuCl on Si obtained from ellipsometry data is very close to what has been reported in the literature for thin CuCl layers [66]. The ellipsometry angles measured for the 65 nm thick layer of CuCl deposited on Si are shown in *Figure 2.18*. The modeled curves were calculated with averaged refractive index data from *Figure 2.17* using a transfer matrix model (discussed in chapter 4). The averaged refractive index allows reliable simulation of ellipsometry angles. Values of the measured refractive index for wavelengths 387 nm and above are in very good agreement with those previously reported in the literature.

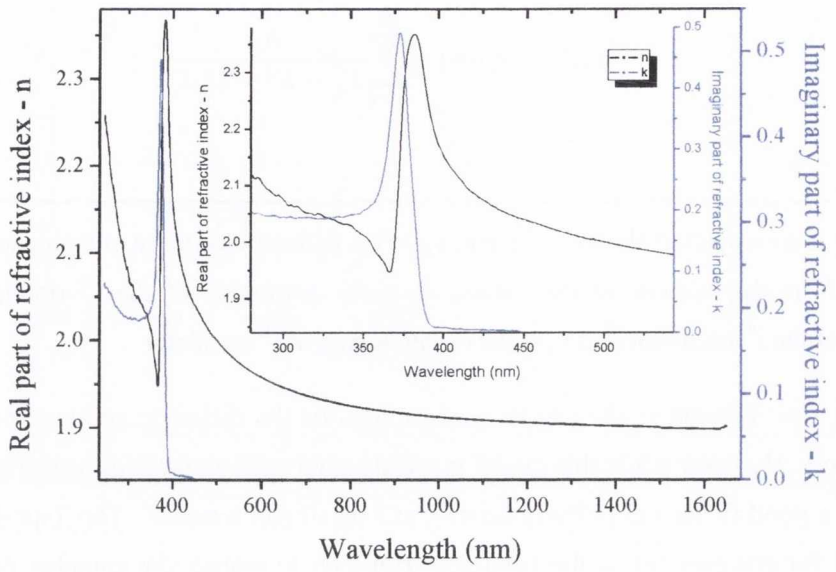

Figure 2.17: *Refractive index dispersion of CuCl on Si obtained from ellipsometry measurements at room temperature. On the left hand side of 'Y' axis the real part of refractive index is marked while on the right hand side the extinction coefficient values are marked. The black curve shows the refractive index of CuCl averaged for the range of samples of thicknes between 60 and 120 nm. The imaginary part is plotted with the blue line. In the inset the proximity of the CuCl band-gap is zoomed.*

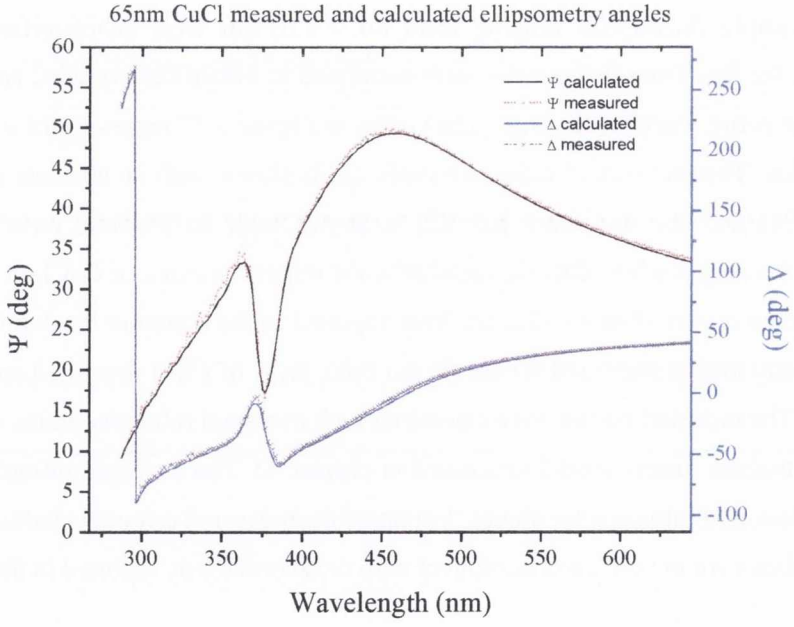

Figure 2.18: *Measured and calculated ellipsometry angles of 65 nm thick CuCl layer deposited on Si.The red and blue dots show the measured values of ellipsometric angles while the solid lines show the calculated curves using the refractive index from Figure 2.17.*

2.4 Conclusions

Copper (I) halides are very promising materials for UV/blue emitters. Due to an excellent lattice match with Si, this new material system is of interest for fundamental studies and possible device applications. XRD examination of vacuum evaporated CuCl layers shows very good structural and optical quality achieved with a relatively simple thermal evaporation deposition technique. Temperature dependent photoluminescence allowed for quantitative determination of some important material parameters, providing insight into the optical quality of the material and allowing for comparision with single crystal CuCl and CuCl thin films deposited by other techniques on a variety of substrates. From analysis of the temperature dependent PL quenching, free exciton thermal activation energies for CuCl and CuBr were determined. Obtained values are 167.8±6.5 meV and 59±7 meV for CuCl and CuBr, respectively, in agreement with literature reports for single crystals. The study of the dependence of the peak width change on temperature provides information about exciton-phonon interactions in both of the copper halide materials studied, and helps to understand the peak broadening mechanism. Further, oxygen plasma treated CuCl layers were studied. Oxygen is expected to be a p-type dopant. The study of oxidised CuCl layers shows that plasma treatment suppresses the luminescence. Additional energy levels that are identified are indicators of material quality deterioration as a consequence of the introduction of the dopant. The activation energies associated with the newly introduced energy levels were obtained from analysis of the temperature dependence of the peak intensity. Using the ellipsometry technique the complex refractive index of CuCl on Si was determined over a wide wavelength range, including in proximity to the band-gap. These values will be used in subsequent chapters for the investigation of microcavity based CuCl structures. All the material parameters obtained for CuCl and CuBr on Si confirm high quality copper halides on Si as indicated by the wide band-gap and very high exciton binding. Additionally the compatibility with Si makes copper halides a very promising electronics/photonics hybrid platform.

2.5 References

[1] F. El Haj Hassan, A. Zaoui, and W. Sekkal, "Structural properties of copper halides," 2001.

[2] S. Adachi, *Properties of group-IV, III-V and II-VI semiconductors*, 1 vols. Chichester: John Wiley & Sons, Ltd, 2005.

[3] J. C. Phillips, "Ionicity of the Chemical Bond in Crystals," 1970.

[4] A. Wojakowska and E. Krzyżak, "Factors affecting the general shape of the phase diagram and compound formation in the binary copper(I) halide-alkali-metal halide systems," 2006.

[5] L. M. Kraemer, "Cuprous Halide Films on Alkali Halide Crystals," *The journal of chemical physics*, vol. 33, no. 4, pp. 991-993, 1960.

[6] I. Tsujikava and E. Kanda, *Fluorescence Spectra of Cuprous Halides at Low Temperatures*. Tohoku University, 1954.

[7] T. Goto, T. Takahashi, and M. Ueta, "Exciton Luminescence of CuCl, CuBr and CuI Single Crystals," *Journal of the Physical Society of Japan*, vol. 24, no. 2, pp. 314-327, 1968.

[8] A. F. Armington and J. J. O'connor, "Gel growth of cuprous halide crystals," 1968.

[9] M. Cordona, "Optical Properties of the Silver and Cuprous Halides," *Phys. Rev.*, vol. 129, no. 1, pp. 69-78, 1963.

[10] D. Frohlich, B. Staginnus, and E. Schonherr, "Two-Photon Absorption Spectrum of CuCl," 1967.

[11] T. Goto, H. Souma, and M. Ueta, "Emission spectra of cuprous halides and their correlation with exciton," *Journal of Luminescence*, vol. 1, p. 231–240, 1970.

[12] A. Mysyrowicz, J. B. Grun, R. Levy, A. Bivas, and S. Nikitine, "Excitonic molecule in CuCl," *Physics Letters A*, vol. 26, no. 12, pp. 615-616, 1968.

[13] L. L. Chase, N. Peyghambarian, G. Grynberg, and A. Mysyrowicz, "Evidence for Bose-Einstein Condensation of Biexcitons in CuCl," *Phys. Rev. Lett.*, vol. 42, no. 18, pp. 1231-1234, 1979.

[14] N. Peyghambarian, H. M. Gibbs, M. C. Rushford, and D. A. Weinberger, "Observation of Biexcitonic Optical Bistability and Optical Limiting in CuCl," *Phys. Rev. Lett.*, vol. 51, no. 18, pp. 1692-1695, 1983.

[15] S. D. Kramer and N. Bloemberg, "Third-order nonlinear optical spectroscopy in CuCl," *Phys. Rev. B*, vol. 14, no. 10, pp. 4654-4669, 1976.

[16] D. C. Haueisen and H. Mahr, "Nonlinear Electronic Dispersion in CuCl," *Physical Review Letters*, vol. 26, no. 14, pp. 838-840, 1971.

[17] M. Nakayama, H. Ichida, and H. Nishimura, "Bound-biexciton photoluminescence in CuCl thin films grown by vacuum deposition," *J. Phys. Condens. Matter*, vol. 11, no. 39, pp. 7653-7662, 1999.

[18] Y. Masumoto, T. Kawamura, and K. Era, "Biexciton lasing in CuCl quantum dots," 1993.

[19] S. Yano, T. Goto, T. Itoh, and A. Kasuya, "Dynamics of excitons and biexcitons in CuCl nanocrystals embedded in NaCl at 2 K," 1997.

[20] Y. Masumoto, T. Wamura, and A. Iwaki, "Homogenous width of exciton absorption spectra in CuCl microcrystals," *Appl. Phys. Lett.*, vol. 55, no. 24, pp. 2535-2537, 1989.

[21] A. Nakamura, H. Yamada, and T. Tokizaki, "Size-dependent radiative decay of excitons in CuCl semiconducting quantum spheres embedded in glasses," *Phys. Rev. B*, vol. 40, no. 12, pp. 8585-8588, 1989.

[22] Y. Kayanuma, "Wannier exciton in microcrystals," *Solid State Communications*, vol. 59, no. 6, p. 405–408, 1986.

[23] Y. Masumoto, S. Okamoto, and S. Katayanagi, "Biexciton binding energy in CuCl quantum dots," *Phys. Rev. B*, vol. 50, no. 24, pp. 18658-18661, 1994.

[24] D. K. Shuh, R. S. Williams, Y. Segawa, J. Kusano, Y. Aoyagi, and S. Namba, "Line-shape and lifetime studies of exciton luminescence from confined CuCl thin films," *Phys. Rev. B*, vol. 44, no. 11, pp. 5827-5833, 1991.

[25] T. Wamura, Y. Masumoto, and T. Kawamura, "Size-dependent homogeneous linewidth of Z3 exciton absorption spectra in CuCl microcrystals," *Applied physics letters*, vol. 59, no. 14, p. 1758–1760, 2009.

[26] T. Itoh, M. Furumiya, T. Ikehara, and C. Gourdon, "Size-dependent radiative decay time of confined excitons in CuCl microcrystals," *Solid State Communications*, vol. 73, no. 4, pp. 271-274, 1990.

[27] M. Nagai, F. Hoshino, S. Yamamoto, R. Shimano, and M. Kuwata-Gonokami, "Spherical cavity-mode laser with self-organized CuCl microspheres," *Optics letters*, vol. 22, no. 21, p. 1630–1632, 1997.

[28] G. Oohata et al., "Stable biexcitonic lasing of CuCl quantum dots under two-photon resonant excitation," *Physica E: Low-dimensional Systems and Nanostructures*, vol. 26, no. 1-4, p. 347–350, 2005.

[29] Y. Kagotani et al., "Two-photon absorption and lasing due to biexciton in CuCl quantum dots," *Journal of Luminescence*, vol. 112, no. 1-4, p. 113–116, 2005.

[30] H. Kurisu, K. Nagoya, N. Nakayama, S. Yamamoto, and M. Matsuura, "Exciton and biexciton properties of CuCl microcrystals in an SiO2 matrix prepared by sputtering method," *J. Lumin.*, vol. 87, pp. 390-392, 2000.

[31] G. Bastard, E. E. Mandez, L. L. Chang, and L. Esaki, "Exciton binding energy in quantum wells," *Phys. Rev. B*, vol. 26, no. 4, pp. 1974-1979, 1982.

[32] S. Schulz and E. P. O'Reilly, "Excitonic binding energies in non-polar GaN quantum wells," *physica status solidi (c)*, vol. 7, no. 7-8, pp. 1900-1902, 2010.

[33] P. Hui, "Quantum-Con nement E ects on Binding Energies and Optical Properties ofExcitons in Quantum Dots," *Chin. Phys. Lett.*, vol. 21, no. 1, pp. 160-163, 2004.

[34] K. L. Shaklee, R. F. Leheny, and R. E. Nahory, "Stimulated Emision from the Excitonic Molecules in CuCl," *Phys. Rev. Lett.*, vol. 26, no. 15, pp. 888-891, 1971.

[35] T. S. Zheleva, O. H. Nam, M. D. Bremser, and R. F. Davis, "Dislocation density reduction via lateral epitaxy in selectively grown GaN structures," *Applied physics letters*, vol. 71, p. 2472, 1997.

[36] I. Kidoguchi, A. Ishibashi, G. Sugahara, and Y. Ban, "Air-bridged lateral epitaxial overgrowth of GaN thin films," *Applied Physics Letters*, vol. 76, p. 3768, 2000.

[37] P. Gibart, "Metal organic vapour phase epitaxy of GaN and lateral overgrowth," *Rep. Prog. Phys.*, vol. 67, pp. 667-715, 2004.

[38] V. Savona, F. Tassone, C. Piermarocchi, A. Quattropani, and P. Schwendimann, "Theory of polariton photoluminescence in arbitrary semiconductor microcavity structures," *Physical Review B*, vol. 53, no. 19, p. 13051–13062, 1996.

[39] R. Houdré, R. P. Stanley, U. Oesterle, M. Ilegems, and C. Weisbuch, "Room-temperature cavity polaritons in a semiconductor microcavity," *Phys. Rev. B*, vol. 49, no. 23, pp. 16761-16764, 1994.

[40] M. Hasuo, N. Nagasawa, T. Itoh, and A. Mysyrowicz, "Progress in the Bose-Einstein Condensation of Biexcitons in CuCl," *Phys. Rev. Lett.*, vol. 70, no. 9, pp. 1303-1306, 1993.

[41] K. Edamatsu, G. Oohata, R. Shimizu, and T. Itoh, "Generation of ultraviolet entangled photons in a semiconductor," *Nature*, vol. 431, pp. 167-170, 2004.

[42] C. Jagadish and S. J. Paerton, *Zinc Oxide Bulk, Thin Films and Nanostructures. Processing, Properties and Applications*, II., 1 vols. Amsterdam, The Netherlands: Elsevier, 2007.

[43] D. P. Norton et al., others, "Charge and Spin-Based Electronics using ZnO Thin Films," in *State-of-the-Art Program on Compound Semiconductors XLI and Nitride and Wide Bandgap Semiconductors for Sensors, Photonics and Electronics V: proceedings of the international symposia*, 2004, p. 276.

[44] J. B. Wagner and C. Wagner, "Electrical Conductivity Measurements on Cuprous Halides," *Journal of Chemical Physics*, vol. 26, no. 6, pp. 1597-1601, 1957.

[45] L. O'Reilly et al., "Characterisation of n-type γ-CuCl on Si for UV optoelectronic applications," *Journal of Materials Science: Materials in Electronics*, vol. 18, no. 1, pp. 57-60, 2007.

[46] D. Danieluk et al., "Optical properties of undoped and oxygen doped CuCl films on silicon substrates," *J. Mater. Sci. - Mater. Electron.*, vol. 20, pp. 76-80, 2007.

[47] S. Hull and D. A. Keen, "High-pressure polymorphism of the copper(I) halides: A neutron-diffraction study to ~10 GPa," *Physical Review B*, vol. 50, no. 9, pp. 5868-5885, 1994.

[48] C. P. Herrero, "Dependence of the silicon lattice constant on isotopic mass," *Solid State Communications*, vol. 110, no. 5, p. 243–246, 1999.

[49] T. Ikehara and T. Itoh, "Dynamical behavior of the exciton polariton in CuCl: Coherent propagation and momentum relaxation," *Phys. Rev. B*, vol. 44, no. 17, pp. 9283-9294, 1991.

[50] Y. Kondo, Y. Kuroiwa, N. Sugimoto, T. Manabe, and S. Ito, "Ultraviolet irradiation effect on the third-order optical nonlinearity of CuCl-microcrystallite-doped glass," *J. Opt. Soc. Am. B*, vol. 17, no. 4, pp. 548-554, 2000.

[51] Y. P. Varshni, "Temperature dependence of the energy gap in semiconductors," *Physica E*, vol. 34, pp. 149-154, 1967.

[52] X. T. Zhang et al., "Temperature dependence of excitonic luminescence from nanocrystalline ZnO films," *Journal of Luminescence*, vol. 99, pp. 149-154, 2002.

[53] Y. Kaifu and T. Komatsu, "Exciton line-width and exciton-phonon interaction in CuCl," *physica status solidi (b)*, vol. 48, no. 2, p. K125-K128, 1971.

[54] N. Garro, A. CantareroManuel, M. Cardona, T. Ruf, A. Göbel, and S. R\übenackeMarkus, "Electron-phonon interaction at the direct gap of the copper halides," *Solid State Communications*, vol. 98, no. 1, p. 27–30, 1996.

[55] A. G\öbel et al., "Effects of the isotopic composition on the fundamental gap of CuCl," *Physical Review B*, vol. 57, no. 24, p. 15183–15190, 1998.

[56] J. J. Pankove, *Optical processes in semiconductors*, II., 1 vols. New York: Dove Publications, Inc., 1975.

[57] T. Makino et al., "Exciton spectra of ZnO epitaxial layers on lattice-matched substrates grown with laser-molecular-beam epitaxy," *Applied Physics Letters*, vol. 76, p. 3549, 2000.

[58] J. B. Anthony, A. D. Brothers, and D. W. Lynch, "Deformation Potentials for Excitons in Cuprous Halides," *Phys. Rev. B*, vol. 5, no. 8, pp. 3189-3193, 1972.

[59] A. I. Ekimov, I. A. Kudryavtsev, and O. G. Lyublinskaya, "Excitonic luminescence spectra of hexagonal CuBr nanocrystals," *Physics of the Solid State*, vol. 39, no. 9, pp. 1479-1480, 1997.

[60] K. Inoue, A. Yamanaka, K. Toba, A. V. Baranov, A. A. Onushchenko, and A. V. Fedorov, "Anomalous features of resonant hyper-Raman scattering in CuBr quantum dots: Evidence of exciton-phonon-coupled states similar to molecules," *Physical Review B*, vol. 54, no. 12, p. 8321–8324, 1996.

[61] H. Shibata, "Negative Thermal Quenching Curves in Photoluminescence of Solids," *Japanese Journal of Applied Physics*, vol. 37, pp. 550-553, 1998.

[62] Y. Kaifu and T. Komatsu, "Refractive Index of CuCl," *J. Phys. Soc. Japan*, vol. 25, p. 644, 1968.

[63] A. Feldman and D. Horowitz, "Refractive Index of Cuprous Chloride," *J. Opt. Soc. Am.*, vol. 59, no. 11, pp. 1406-1408, 1969.

[64] M. Cardona, "Optical Properties of the Ag and Cuprous Halides," *Phys. Rev.*, vol. 129, no. 1, p. 69, 1963.

[65] A. Bohun, M. Lebl, and M. Rozsival, "The Absorption of Cupric Halides," *Z. Physik*, vol. 234, pp. 261-267, 1970.

[66] M. T. Kostyshin and I. Z. Indutnyi, "Spectral dependence of optical constants in the region of copper chloride exciton absorption," *Ukr. Fiz. Zh.*, vol. 22, no. 8, pp. 1367-1370, 1977.

[67] B. von Blanckenhagen,, D. Tonova, and J. Ullman, "Application of the Tauc-Lorentz formulation to the interband absorption of optical coating materials," *Appl. Opt.*, vol. 41, p. 3137, 2002.

3 CuCl Photonic Crystals for TeraHertz Applications

3.1 Introduction

Terahertz (THz) radiation covers the range of electromagnetic waves with frequencies between 0.3 THz and 10 THz. For this band of frequencies many materials exhibit absorption corresponding to vibration and/or rotation of their molecules. Depending on the presence of an electric dipole in molecules, they present a sensitivity to the THz, as demonstrated for instance with the water molecule. This is useful in a large range of applications [1] such as medical imaging [2-4], security systems [5], [6], communication [7], [8] and spectral or chemical analysis [9]. These applications generate a high demand for efficient THz radiation sources, detection and waveguides [1], [10]. Water absorbs THz radiation which prevents long haul transmission of the THz signal [11] in air. For frequencies over 0.5 THz (which is sometimes labelled as upper THz) transmission in air becomes virtually impossible. The atmospheric transmission of THz radiation drops from ~80% at 1 THz to ~30% at 3 THz. Being at the transition between the light (IR) and radio frequencies THz radiation has been found very hard to work with. Visible or infrared light radiation can propagate in air and in optical fibres with a typical attenuation of 0.2dB/km. On the other hand because of omnipresent water vapour in air and OH ions in optical fibres, the attenuation of THz radiation is very high [12], [11]. Thus the need for suitable THz waveguides has to be addressed. Because of the light-like nature of THz radiation one might expect mature SiO_2 optic fibre technology could provide a waveguide as a solution, however high absorption by SiO_2 makes it impossible [13], [14]. Other possible solutions that have been investigated to date have also been found to be unsuitable for one reason or another [15-19]. The attempt to use metallic wire-like waveguides was also not satisfactory due to the finite metal conductivity. Thus the search for more sophisticated solutions is underway, amongst them hollow fibre waveguides, planar metallic waveguides and surface plasmons can be mentioned [10], [14], [20-23]. Photonic crystal (PC) structures of different types were proven to be an option for THz mirrors [24-27].

One of the most important materials used in the THz range is high resistivity silicon (HR-Si) [28-33]. It has a high value of refractive index and low absorption over a wide range of the THz band. High resistivity silicon has almost a constant value of refractive index n of 3.42 and an extinction coefficient k varying between 4.8e-6 and 1.16e-4 in the range of 0.5 to 4.5 THz [34]. In particular its low absorption makes HR-Si the material of choice in PC design for far-infrared and THz applications. Very good reflectivity values of 0.9995 are achievable using HR-Si, even with 1D structures, over a wide range of frequencies [26]. However, it is a high cost option, which has motivated research to look at alternative material options [35], [28] for some specific applications even if it means compromising on the material refractive index and absorption. For example, alumina with a refractive index of 3 has the extinction coefficient between 0.006 and 0.031 in the range of 1 to 3 THz and steatite, with a refractive index of 2.5 and extinction coefficient varying

between 0.0126 and 0.05 in the range of 0.2 and 1 THz have been investigated [28]. In this context CuCl is an alternative material for THz applications. Some CuCl PC structures have already been examined [36], specifically 2D and 3D (square and cubic) lattices. The dielectric constant for these simulations was obtained from a theoretical model. In this work the simulations of four 2D PCs will be performed with the refractive index values obtained experimentally [37]. The square lattices similar to those from [36] will be compared with triangular lattices. At room temperature CuCl has a reasonably low extinction coefficient ranging from 0.012 to 0.023 in the band of 8 to 10 THz. The real part of the refractive index in this range is approximately 1.9. The dip in absorption for high THZ frequency band occurs at 8.56 THz with k=0.014 [37]. Between 8.56 THz and 9 THz the absorption coefficient rises from 0.014 to 0.018 and above 9 THz constantly decreases, reaching ~0.012 at 10 THz. For the lower THz band, the extinction coefficient at room temperature is higher and varies between 0.06 and 0.22 in the range of 0.5 to 2 THz. The absorption is highly dependent on temperature and the extinction coefficient becomes very low at cryogenic temperatures. CuCl absorption in THz range originates in phonons. At high temperatures phonon absorption lines broaden and the absorption increases in the wide band of THz radiation. In the range of 1.5 to 3.5 THz it varies between 0.005 and 0.018 and has a local minimum of 0.005 at 3THz at liquid He temperature [37]. The real part of refractive index below 3.5 THz is ~3.

Four PC structures based on CuCl will be studied in order to investigate the usability of CuCl for THz mirror design. In particular the 8 THz frequency region will be studied, where the CuCl absorption compares favourably with other materials. Two lower symmetry square lattices and two higher symmetry triangular lattices will be discussed.

Introduction to Photonic Crytsals

For many years now electronic devices have found a wide range of application in our lives. Actually all aspects of human activity rely on some form of electronic devices. Early attempts of practical application of electricity started in the XVIII century long before the discovery of the electron. The phenomenon of electricity found dual applications. On one hand the energy of electrons can be distantly transmitted and converted to any usable form, such as radiation or mechanical energy. It was also realised very early that electrons can carry information. The importance of this fact motivated research to push electronics to its limits.

By the electronics we mean the ability to understand and modify material properties in order to control the conductivity of electrons. It took only a few decades from the invention of the transistor to approach the technological limits of semiconductor technology [45], [46]. Progress in electronics has been based on the miniaturisation of its basic structures, the transistors, with the limits of this miniaturisation now being reached. Also the quantum nature of electrons introduces even more difficulties. Electrons, as fermions, obey the Pauli's exclusion rule and as such cannot

constitute coherent states. The carriers that can form the coherent state tend to share properties on the macro scale. For example photons, being bosons, can create the coherent state in the form of laser light. Such a beam of coherent photons is an excellent information carrier. The benefit of coherence in terms of information processing is the ability of coherent states to be sustained without significant losses. An example is laser light transmitted with insignificant loss via optic fibre. The electric current as a flow of electrons (fermions) is prone to information loss. Virtually lossless electric current transmission is possible only via superconductors. In such materials, electrons or holes (which are fermions), form virtual particles which in turn behave like bosons. Such an electronic state is achievable only at very low temperatures, while photons behave coherently at room temperature and above. Thus photons were found to be much more adequate carriers of information. In order to make more use of photons methods similar to those which control electrons in electronic devices have to be developed. Additionally, the aforementioned physical limitations of Si based technology in terms of the possibilities for further miniaturisation, is driving research towards photonic solutions.

Solid state materials can be divided into three groups according to their conductive properties. Conductors are highly conductive materials in which the conduction and valence bands overlap. If the valence and conduction bands are separated by an energy gap the materials act as an insulator or a semiconductor. The electronic properties, in simplified form, originate in the crystalline structure of solids. The same chemical compound has different properties in different crystalline structures. Moreover even a particular crystalline structure can have different electronic properties in different directions. Such anisotropy is a result of the lack of symmetry. One of these electronic material properties is a band-gap. The way in which an electron may or may not propagate within the structure depends on the periodicity of the structure.

The photonic crystal (PC) similarly influences the propagation of photons analogous to the periodicity of atoms influencing the propagation of electrons. Thus, a PC is a periodic structure whose dimensions are related to the wavelength of photons [47]. A PC is a periodically distributed structure of materials having different refractive indices. Such periodic structures of dielectric materials are potentially useful in the range of electromagnetic radiation, where conventional materials find very limited usage, namely, terahertz (THz).

3.2 The theory

3.2.1 Photonic Crystal Theory

The periodic structure of materials with different refractive indices is called a crystal by analogy with the atomic crystal [47]. Thus the nomenclature and understanding of solid state physics can be applied to photonic crystals. In *Figure 3.1* there are three photonic crystal structures presented.

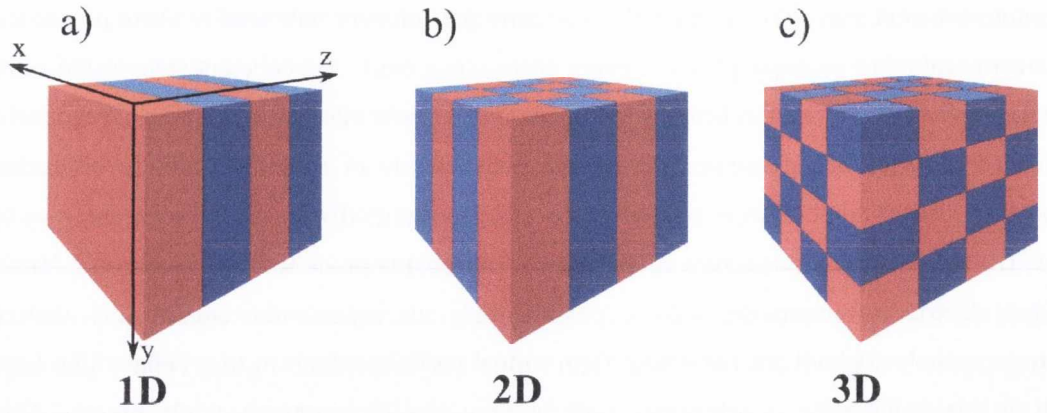

Figure 3.1: *The photonic crystals with periodicity of refractive index in one, two and three dimensions. The red and blue fields represent the volumes of different refractive index.*

The simplest one is a 1D photonic crystal. The different materials composing the crystal create a periodic structure in only one direction. In other words a 1D photonic crystal is a stack of pairs of materials and is generally known as a distributed brag reflector (DBR). This type of structure is used in the planar microcavity simulations in chapter 4. In this case the periodicity of the crystal depends only on the thicknesses of particular layers. In a more complex case, depicted in *Figure 3.1b,* the different materials create a two-dimensional structure. In 2D the basic elements can also be distributed periodically. The periodicity can be classified by analogy with crystalline lattices of atomic crystals. The equivalents of atoms or particles in electronic crystals are the rods of many possible cross-sections in the 2D photonic crystals which can be arranged in various ways. The 3D photonic crystal is of course the most analogous to the electronic crystal structure. Such a structure is built of the particles of one material periodically distributed in some other materials in all spatial dimensions. The particles can have different shapes, and are presented as cubes in *Figure 3.1c.*

The propagation of the electromagnetic field inside the structure with changing dielectric constant is described by *Equation (2.3)* [47].

$$\nabla \times \left(\frac{1}{\varepsilon(r)} \nabla \times H(r)\right) = \left(\frac{\omega}{c}\right)^2 H(r) \qquad (3.1)$$

Where, ε is the dielectric constant, H is the magnetic field, ω is the frequency and c is the speed of light in vacuum. This differential equation can be numerically solved for the structure given and then the electric field E can be calculated.

$$E(r) = \frac{i}{\omega \varepsilon_0 \varepsilon(r)} \nabla \times H(r) \qquad (3.2)$$

Where ε_0 is the vacuum dielectric constant.

The dielectric constant inside the PC is periodic. Thus the field inside the crystal can be expressed as the product of the plane wave and the periodic perturbation originating in the crystalline lattice periodicity.

$$H(r) = e^{ik \cdot r} \cdot u_k(r) \tag{3.3}$$

3.2.2 The plane wave expansion method

One of the most basic tasks in designing the photonic crystal is the determination of its band structure. In other words one has to determine which modes of electromagnetic field are allowed within the structure. One of the suitable approaches is the plane wave expansion method [48]. Both the fields and the dielectric constant are periodic inside the PC and can be expanded into Fourier series. Thus, the Helmholtz *equation (2.3)* can be expressed in form of plane wave superposition:

$$H(r) = e^{i\vec{k}r} \sum_{\vec{G}} H_{\vec{G}} e^{i\vec{G}r} \tag{3.4}$$

where $\vec{G}$ is the PC reciprocal lattice vector, $\vec{k}$ is the Bloch vector and $H_{\vec{G}}$ is the magnetic field plane wave expansion amplitude. For a given crystalline structure the Fourier series of the inversed dielectric constant can be expressed analytically.

3.2.2.1 The 2D case example

As an example the case of periodically arranged solid cylinders of material having dielectric constant ε_1 in the surrounding medium of dielectric constant ε_2 is considered. Such a structure is shown in *Figure 3.2.* The rods of the radius r and dielectric constant ε_1 are arranged into a triangular lattice in the medium material of dielectric constant ε_2. The lattice is characterised by the lattice constant *a.* This type of lattice is also known as the hexagonal lattice since the first Brillouin zone has hexagonal shape. The Brillouin zone has a similar meaning to that used in solid state physics nomenclature. In this 2D case it is the area bounded by the normals to the line segments connecting the rod with its closest neighbours. For such a lattice, when the rods are arranged in *x-y* plane the periodic electromagnetic waves can be expressed as follows:

$$H(r,t) = [0,0,H_z(r)]e^{-i\omega t} \tag{3.5}$$

$$E(r,t) = [E_x(r), E_y(r),0]e^{-i\omega t} \tag{3.6}$$

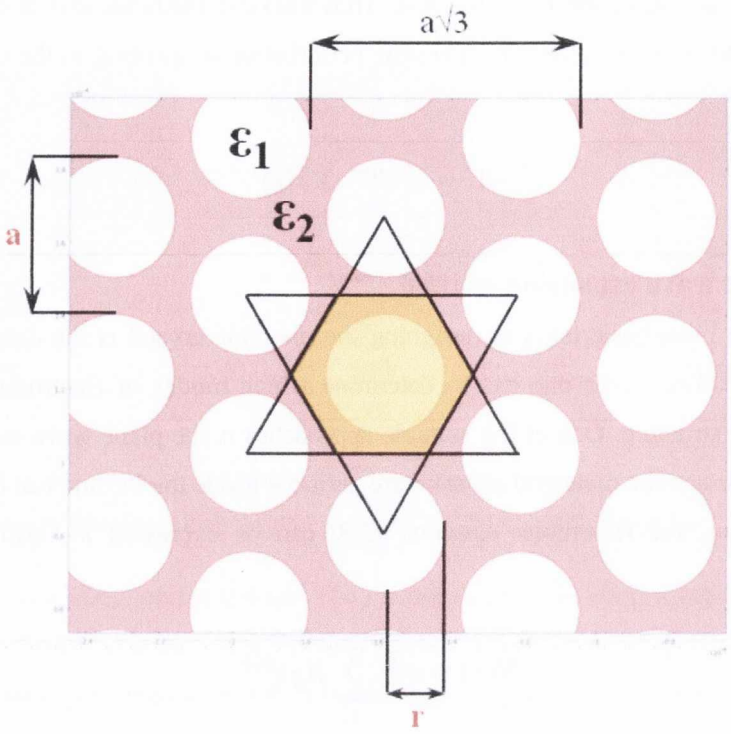

Figure 3.2: *The triangular lattice scheme. The first Brillouin zone is depicted as the orange area in the middle. Different materials distinguished by their dielectric constant are marked with* ε_1 *and* ε_1*. The critical parameters of the structure namely the lattice constant 'a' and the rod radius 'r' are also shown.*

By substitution of equations (3.5) and (3.6) into Maxwell equations and assuming that μ=1 the equation for the *z*-component of the magnetic field which is the special case of equation (2.3) is obtained.

$$\frac{\partial}{\partial x}\left[\frac{1}{\varepsilon(r)}\frac{H_z(r)}{\partial x}\right]+\frac{\partial}{\partial y}\left[\frac{1}{\varepsilon(r)}\frac{H_z(r)}{\partial y}\right]=\left(-\frac{\omega}{c}\right)^2 H_z(r) \qquad (3.7)$$

And by applying the Bloch theorem the *H* field is expanded into the superposition of plane waves

$$H_z(r)=\sum_G H(k+G)e^{i(k+G)\cdot r} \qquad (3.8)$$

where k is the wave vector in Brillouin zone, G is the reciprocal lattice vector and $H(k+G)$ is the expansion coefficient corresponding to G. The dielectric constant $\varepsilon(r)$ in equation (3.7) is periodic function of the position. Its inverse is expressed with the Fourier series:

$$\frac{1}{\varepsilon(r)} = \sum_{G} \varepsilon(G) e^{-iG \cdot r} \tag{3.9}$$

By the substitution of equations (3.8) and (3.9) into equation (3.7) the final equation is obtained.

$$\sum_{G'} (k+G) \cdot (k+G') \varepsilon(G-G') H(k+G) = \frac{\omega^2}{c^2} H(k+G) \tag{3.10}$$

An analogous equation can be written for the E polarized mode.

$$\sum_{G'} (k+G') \cdot (k+G) \varepsilon(G-G') E(k+G) = \frac{\omega^2}{c^2} E(k+G) \tag{3.11}$$

Both equations can be expressed as matrix eigenvalue equations of the form:

$$MH = \lambda H$$
$$\lambda = \frac{\omega^2}{c^2} \tag{3.12}$$

where M is an $N \times N$ matrix and N is the number of terms in the expansion of equation (3.13). The eigenvalue of matrix M gives the frequencies of allowed modes in the periodic structure for the given wavevector k.

The band structure for the triangular lattice of Figure 3.2, implemented for the case of rods of CuCl in air, is presented in *Figure 3.3*. The code was implemented in MATLAB programming language. The refractive index value used in the simulation is of 1.9 which corresponds to CuCl in the high frequency range over 8 THz. The y-axis is the normalised frequency, $\omega a/2\pi c$, and the x-axis shows positions corresponding to the wave vectors in the first Brillouin zone taking into account the lattice symmetry. The TM polarised wave has a band of forbidden frequencies depicted by the red band in *Figure 3.3a,* while there is no frequency for which propagation is forbidden for all wavevectors of the TE polarised mode. In such a case the photonic crystal has a TM polarised photonic band-gap. If the crystal has band-gaps for both TM and TE polarisations,

and moreover these band-gaps overlap, the common band of both is called the complete band-gap. Such a structure is then an omnidirectional mirror for any unpolarised or polarised wave.

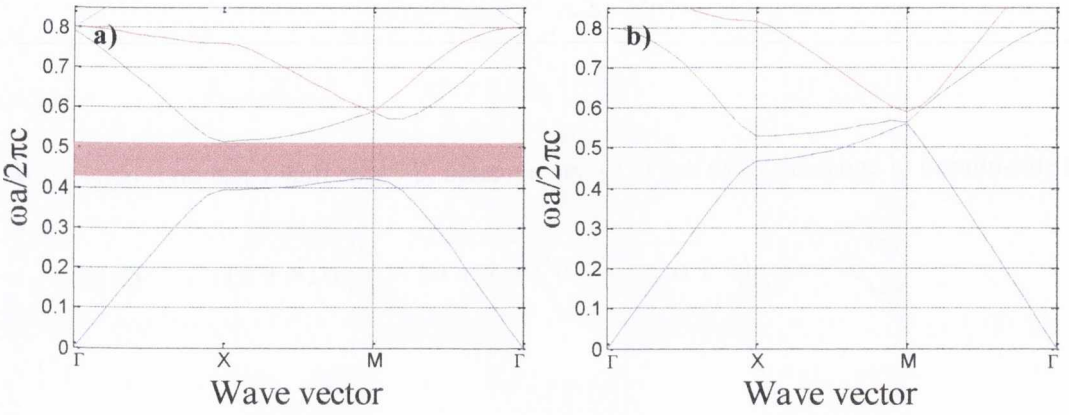

Figure 3.3: *The band structure of a triangular lattice for TM and TE mode (figures (a) and (b), respectively). The rectangle in figure (a) represents the band-gap. For the TE mode the band gap is not present.*

The band structure diagrams from *Figure 3.3* are calculated for a particular triangular lattice lattice defined by lattice parameters r and a. For further analysis it is convenient to characterize the lattice by the ratio of these parameters, called the filling ratio. Thus the range of ratios $0 < r/a < 0.5$ corresponds to the case for which the rods do not overlap. For $\frac{r}{a} > 0.5$ the rods start to overlap and the structure becomes more complex. The periodicity of the dielectric constant is controlled by the filling ratio. In

Figure 3.4 the band-gap widths are indicated for the range of filling ratios between 0 and 0.5, this is known as a band-gap map.

The band-gap regions resemble islands. The width of the island in normalised frequency gives information about the possible band-gap spectral width in the crystal. The width in terms of filling ratio helps to determine the lattice parameters and gives some information about possible tolerance in physical dimensions. The lattice parameters are determined in accordance to the desired PC band-gap frequency. In general the photonic crystals are scalable structures. Initially the concept was proven for microwave structures for which constituent structure scales are big, reaching macroscopic dimensions. For the selected frequency, corresponding to the central frequency of the stop-band, r and a can be obtained from the set of equations:

$$f_{norm} = \frac{f \cdot a}{c}$$
$$FR = \frac{r}{a} \tag{3.14}$$

Where f_{norm} is the normalised frequency, f is the central stop-band frequency, c is the speed of light, FR is the filling ratio of the rod radius - r and the lattice constant - a. FR and f_{norm} are read from the band-gap map. Finally r and a are given as:

$$a = \frac{f_{norm} \cdot c}{f}$$

$$r = \frac{FR}{a} = \frac{FR \cdot f}{f_{norm} \cdot c} \tag{3.15}$$

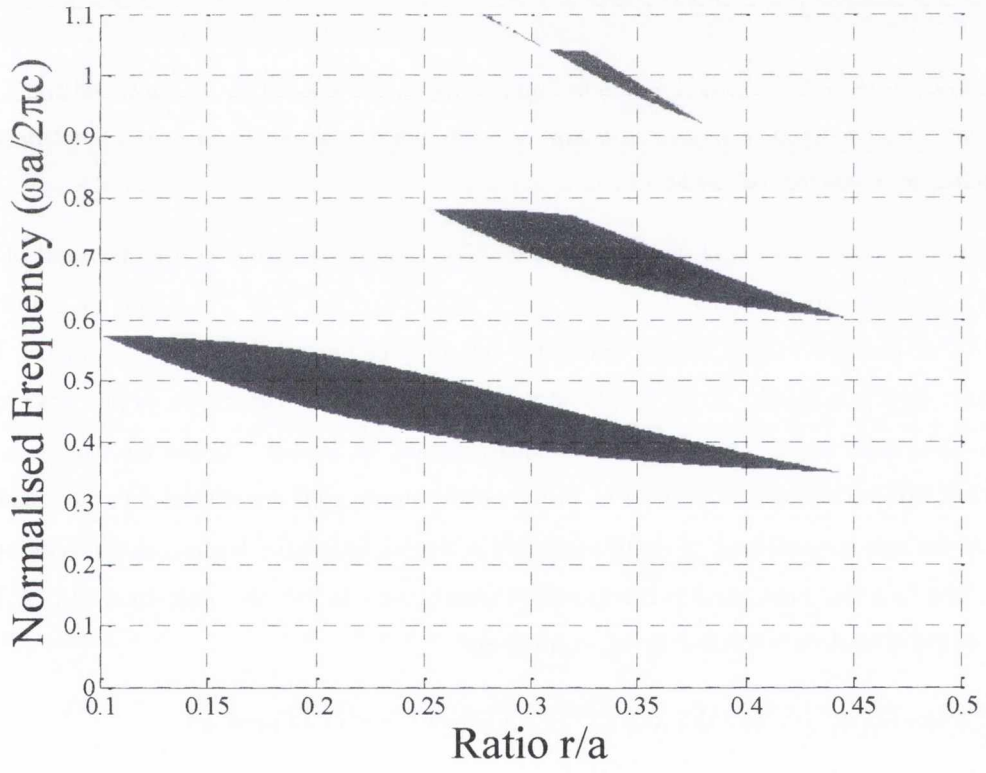

Figure 3.4: *The band-gap map of TM polarised mode in triangular lattice. From the ordinate the band-gap width can be obtained. The abscissa contains the information about the lattice parameters. For every pair of normalised frequency and ratio the exact lattice parameters can be determined for the given frequency ω.*

3.3 Comparison of different CuCl structures

Based on the concepts introduced above the results of simulations for four different PC structures will be presented. In *Figure 3.5* schematic drawings of two basic structures of 2D photonic crystals are shown.

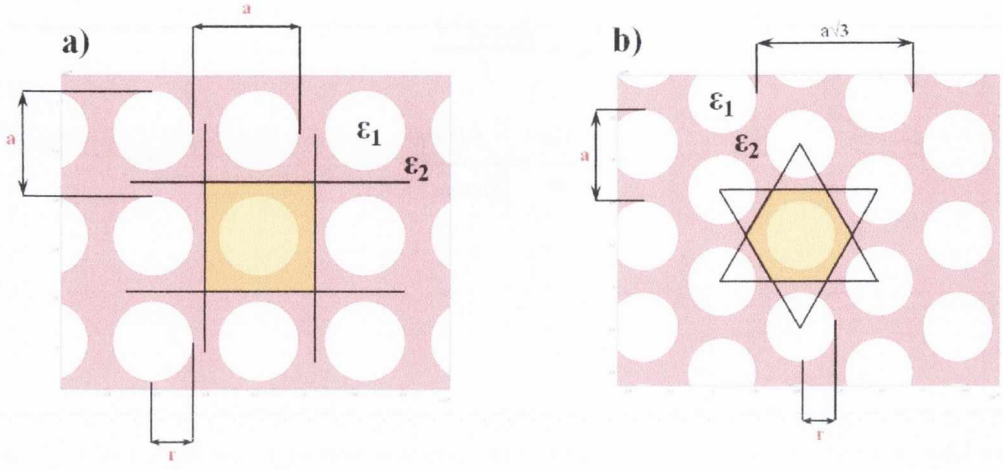

Figure 3.5: *The schematic drawings of PC lattices. The square (a) and the triangular (b) lattice are presented. The orange areas show the first Brillouin zones for both structures. The structures are defined by the lattice constant 'a' and the rod radius 'r'.*

In *Figure 3.5a* the simplest case is depicted. The circular rods of dielectric constant ε_1 and of the radius r are equidistantly distributed in both the x and y directions in a medium of dielectric constant ε_2. The distance a is the lattice constant. Such a lattice has a low level of symmetry. The first Brillouin zone is a square. It can be also noticed that the centres of neighbouring rods create the squares, and thus the lattice is named the square lattice. In *Figure 3.5b* the circular rods are organized in a different pattern. The centres of the neighbouring rods are placed on an equilateral triangle with the side length being the lattice constant a. Such a lattice has higher, closer to circular, symmetry. The first Brillouin zone is hexagonal in shape, such as the case described earlier. The four cases that will be discussed later in this section are:

-The square lattice where the rods of CuCl are distributed in air medium.

(*Figure 3.5a* with $\varepsilon_1=3.61$ and $\varepsilon_2=1$).

-The inverse square lattice where holes of air are distributed in CuCl.

(*Figure 3.5a*, with $\varepsilon_1=1$ and $\varepsilon_2=3.61$).

-The triangular lattice with CuCl rods distributed in air.

(*Figure 3.5b* with $\varepsilon_1=3.61$ and $\varepsilon_2=1$).

-The inverse triangular lattice, with air holes distributed in CuCl.

(*Figure 3.5b*, with $\varepsilon_1=1$ and $\varepsilon_2=3.61$).

For the purpose of the simulation the refractive index n of 1.9 for CuCl was assumed. The extinction coefficient k was initially omitted. The influence of absorption on PC reflectivity as well as on band-gap maps will be discussed later. In *Figure 3.6* the band-gap maps calculated for both square and inverse square lattices of CuCl rods in air are presented.

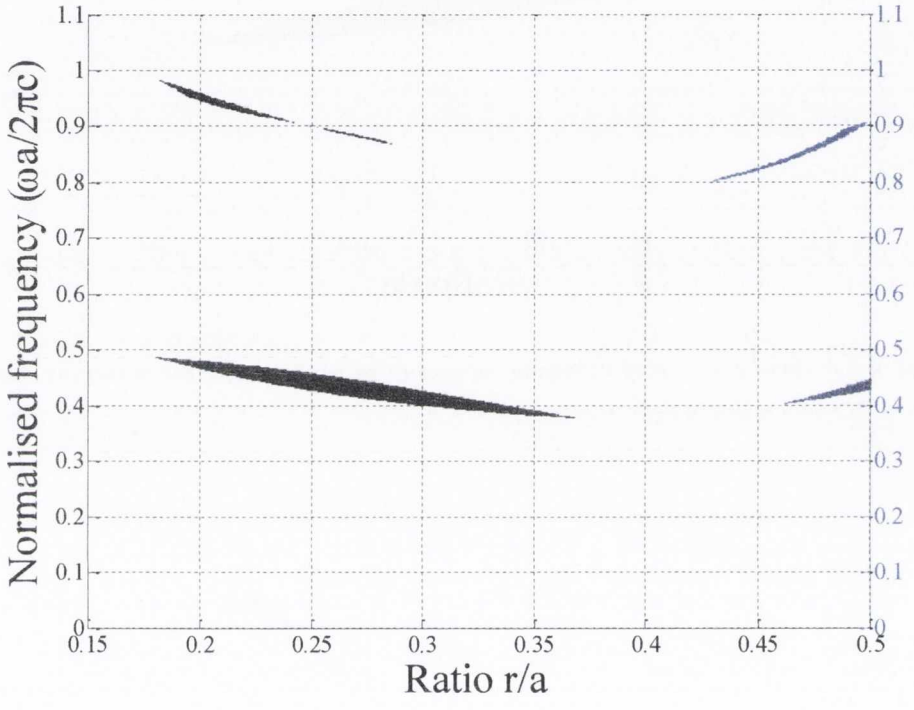

Figure 3.6: *Band-gap maps of square (black islands) and inverse square (blue islands) lattcies. The simulation was done for a refractive index of 1.9 which represents the lowest contrast for CuCl in THz range. The band-gap islands are relatively small which means that the photonic crystals would have low lattice parameters tolerance and the achievable band-gaps would be narrow.*

There is no band-gap for the TE mode in the square lattice and thus only TM mode band-gap islands are marked in black. Both TM (dark blue) and TE (light blue) islands of inverse square lattices are plotted on the right hand side of the figure. For comparison, the band-gap maps of triangular and inverse triangular lattices are presented in *Figure 3.7* and *Figure 3.8* respectively.

Both triangular lattices have significantly wider band-gaps originating in a higher level of symmetry than for the square lattice.

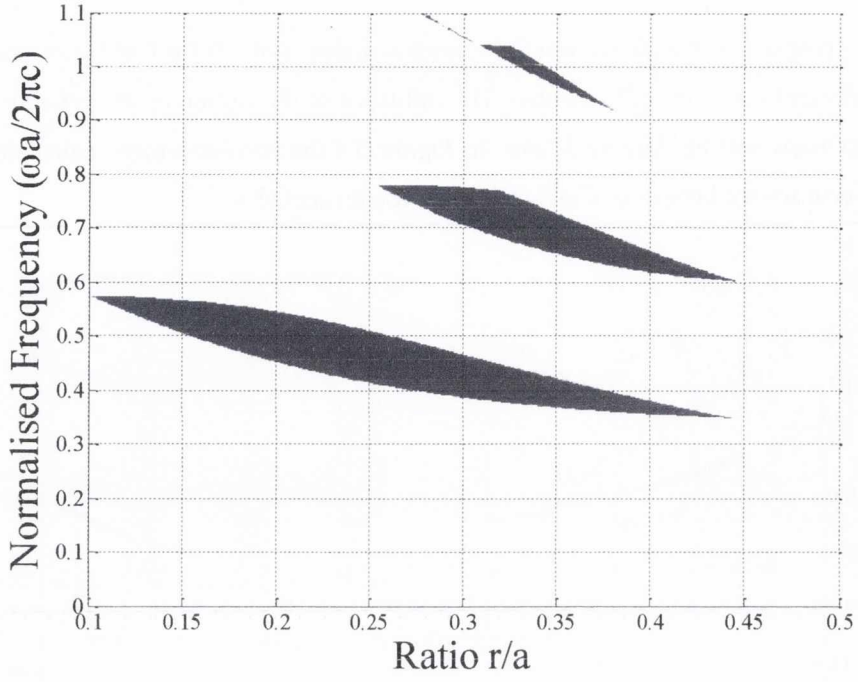

Figure 3.7: *Band-gap map of triangular lattice of CuCl rods in air. TM modes are marked dark grey, TE modes are not present in this structure.*

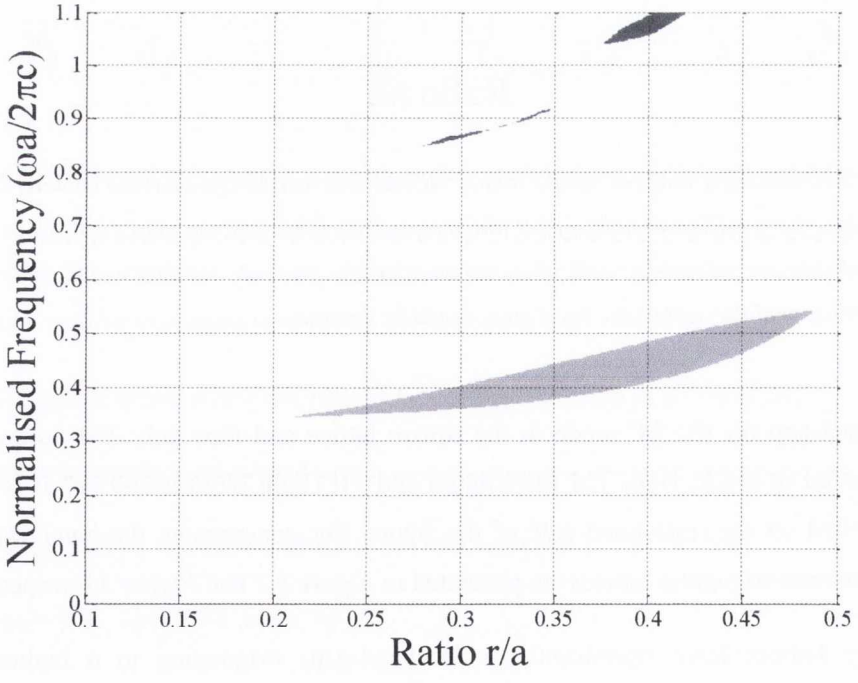

Figure 3.8: *Band-gap map of a triangular lattice of air holes in CuCl (inverse triangular). TM and TE modes are marked dark grey and light grey, respectively.*

The band-gap width can be obtained from the difference of the normalised frequency borders for a particular r/a value. Further analysis will thus concentrate on the triangular lattices. The influence of the absorption on the band-gap width is shown in *Figure 3.9*.

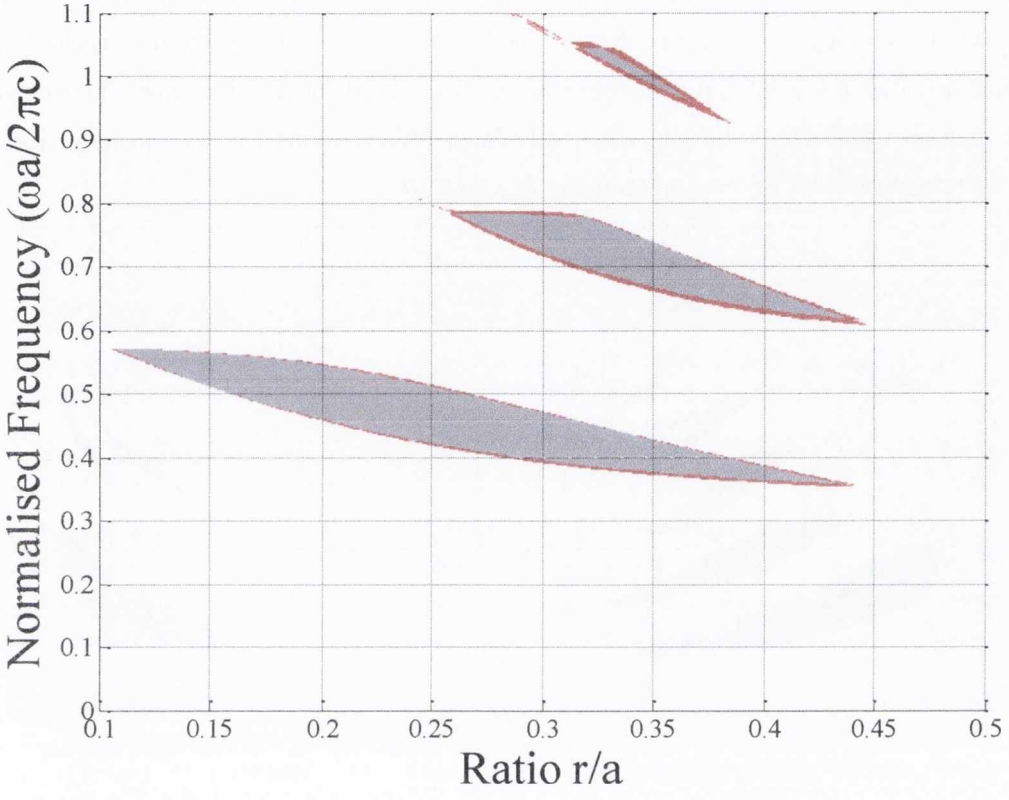

Figure 3.9: *The band-gap maps for triangular lattice calculated with and without absorption. The widening of band-gap due to absorption is depicted by the red rim around the grey island for the non-absorbing case. The widening of band-gap island is only apparent. In fact due to increased absorption particular modes do not propagate within structure but also they are not reflected.*

The grey islands in *Figure 3.9* are band-gap maps for the triangular lattice of non-absorbing CuCl (n=1.9, k=0) rods in air. Introduction of absorption (k=0.3) into the simulation broadens the band-gap. A non-zero absorption value requires the dielectric function in equations (3.16) and (3.17) to be treated as a complex number. The band-gap islands of absorbing CuCl (n=1.9, k=0.3) are the sum of grey fields and red rims. This apparent broadening of the band-gap islands can be misleading. The band-gap islands should indicate areas in space of normalised frequency and filling ratio where modes are not able to propagate, but in the case of absorption the modes are not excluded from propagation because of reflection, but rather due to interaction with the structure (i.e. with phonons). The reflectivity spectra of PC structures, presented later, will show further how the absorption affects the PC performance. As was shown in *section 3.1* the refractive index of CuCl is not constant in THz range.

Two THz bands can be considered, the range below 3.5THz, where the absorption coefficient is low at cryogenic temperatures but rises at room temperature and the band of frequencies over 8 THz where the absorption remains low in comparison with other materials used for THz applications even at room temperature. The band-gap maps shown in *Figure 3.6* to *Figure 3.9* are calculated for a refractive index of 1.9. This value is valid for high frequencies. Below 3.5 THz the refractive index n is approximately 3. The higher value of refractive index leads to wider band gaps, and thus the band-gap maps have to be recalculated for low frequency THz bands in order to remain valid. The band gap maps calculated for the triangular and inverse triangular lattices for refractive index of 3 are presented in *Figure 3.10*.

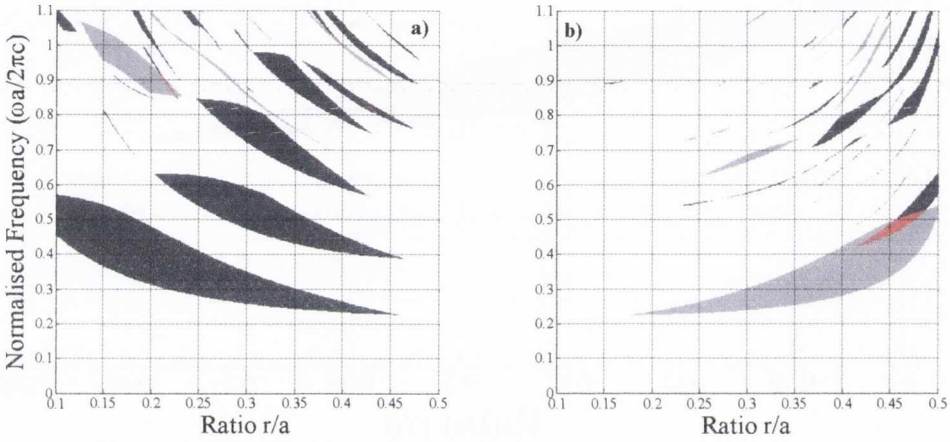

Figure 3.10: *Band-gap maps of triangular and inverse triangular lattices for a refractive index of 3. Dark grey areas represent TM mode, light grey TE mode. The complete band-gap areas are marked in red colour.*

In both cases the islands are significantly bigger than for a refractive index of 1.9. Moreover the complete band-gap emerges due to the increased refractive index contrast. In the case of the triangular lattice the complete band-gap is only residual. The width of the band-gap in dimensionless frequency units is 0.006. It would be virtually impossible to observe it experimentally. In the case of the inverse triangular lattice the complete bad-gap is more significant, but still much smaller than the TE band-gap alone. These band-gap values are 0.034 and 0.158, respectively. The enlargement of band-gap maps with increased refractive index contrast is in agreement with the trend expected.

The band-gap maps in *Figure 3.10* do not include the absorption. In order to examine the influence of absorption on the PC properties, reflectivity spectra are calculated using a transfer matrix method described in more detail in chapter 4. To calculate the reflectivity the optimal parameters of the structures are required and these can be obtained from the band gap-map. The intersection of the island in the y direction gives the stop-band width for the particular lattice

parameters r and a. The intersection of the island in the x direction gives the range of filling ratios for which any particular frequency remains within the gap. The optimal parameters occur when the stop-band is the widest and the range of filling ratios is as wide as possible for the central frequency of the stop-band. The optimal parameters of the lattice correspond can be obtained from such a bad-gap map. The normalised frequency is the dimensionless measure of the band-gap. Having the optimal (maximum) frequency the filling ratio can be read. From this pair of parameters (normalised frequency and filling ratio) the radius and the lattice constant can be determined for the frequency given. The issue is discussed in more details in *section 3.2.2.2.* From *Figure 3.10* the optimal parameters can be determined for a filling ratio r/a of 0.19. Since this map is valid for frequencies below 3.5 THz, the central frequency can be taken as 3 THz. From the map the stop-band border frequencies can be read as 0.32 and 0.49 with the centre at approximately 0.4. Using *equation (3.15)* the lattice parameters r and a can be determined for any given frequency. For example, for 3 THz central frequency r=7.6 μm and a=40μm. Such structures can be physically achieved. Dimensions above 10 μm for both the rod diameter and the lattice constant are not so difficult to work with even with relatively simple techniques such as chemical etching. In *Figure 3.11* the reflectivity spectra of the triangular lattice PC with lattice parameters determined above are presented.

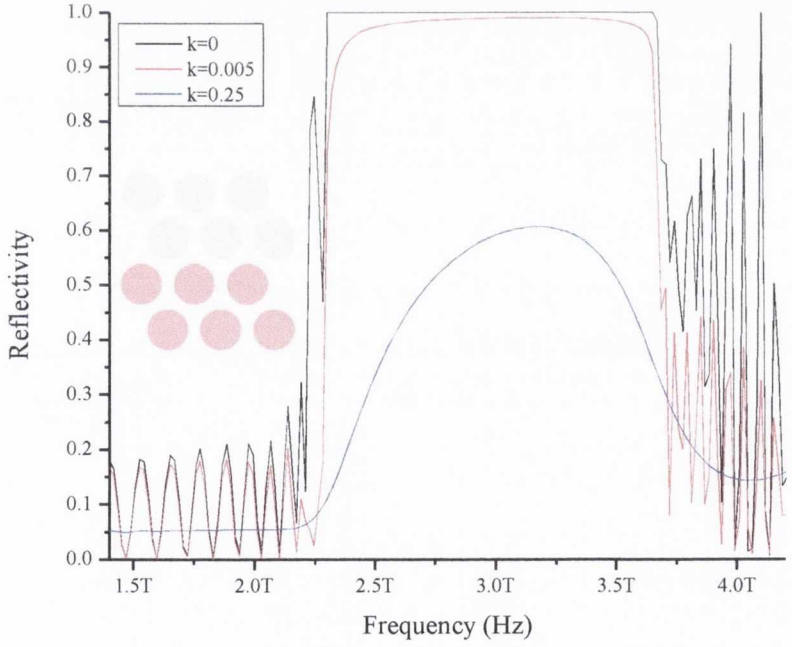

Figure 3.11: *Reflectivity spectra of CuCl based triangular lattice PC for three different extinction coefficient values. The structure consists of 16 periods of PC. An inset shows two periods of the triangular lattice. The idealised case of non absorptive medium can be treated as the reference. For k=0.005, which is CuCl at liquid He, the reflectivity of approximately 0.98 is achievable. For k=0.25 which corresponds to CuCl at RT reflectivity drops to less than 60%.*

The Translight software developed by Andrew L. Reynolds in the University of Glasgow was used for these computations. The triangular lattice of CuCl rods in air is considered as this geometry contains less of the absorbing medium than the inverse triangular lattice of air holes in CuCl. The stop-band determined using these parameters ranges from 2.4 THz to 3.67 THz. The curves show reflectivity as a function of frequency for three values of extinction coefficient k. The reflectivity of the structure with omitted absorption (k=0) is plotted with the black line. The reflectivity reaches a value of 100% in this case. However, as was previously discussed, CuCl has non-negligible absorption even at cryogenic temperatures. The red curve shows the results for the optical parameters of CuCl at liquid helium temperature, where $n=3$ and $k=0.005$ at frequency of 3THz. In this case the reflectivity is decreased, but remains at a level of approximately 0.98 over a wide range of frequencies. The blue line shows the reflectivity calculated for an extinction coefficient of 0.25, which corresponds to the room temperature case, also at 3THz. Such a high value of absorption significantly suppresses the reflectivity of the PC mirror, which only slightly exceeds a reflectivity of 50%.

On the other hand, as previously discussed, CuCl has relatively low absorption at room temperature for frequencies over 8THz. The absorption coefficient data from the reference [37] are presented in *Figure 3.12*.

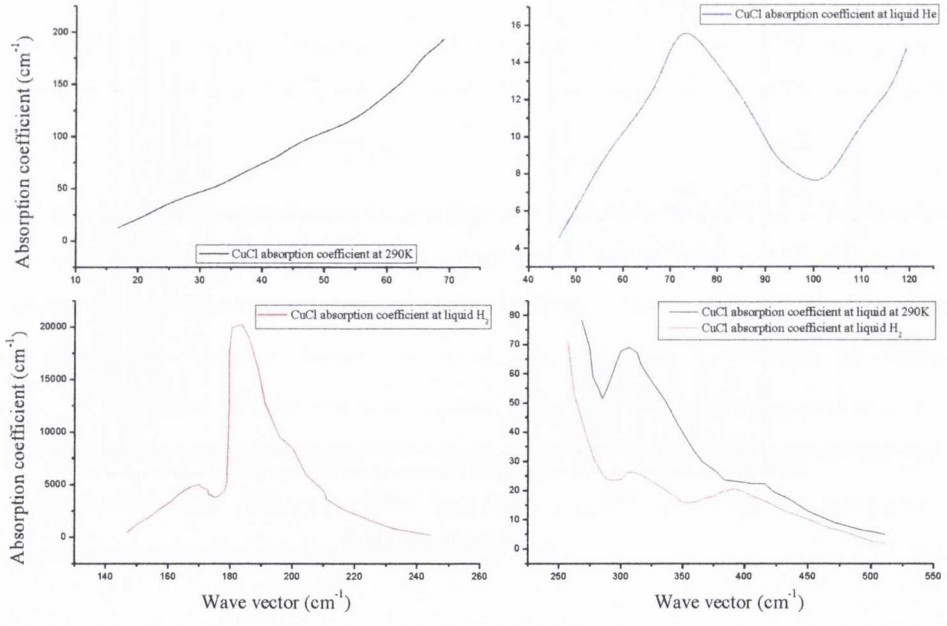

Figure 3.12: *The absorption coefficient of CuCl in THz/far infrared range after the reference [37]. Different temperatures are marked with appropriate colours. There are few bands of low absorption visible, even at room temperature.*

As can be seen, the absorption of CuCl of frequencies above 8 THz has a minimum at 8.56 THz, increases slightly up to 9 THz before decreasing again. Using the band-gap map from *Figure 3.7* the lattice parameters for the PC with a triangular lattice of CuCl rods in air with a band-gap at 8.56 THz are calculated. A radius r of 3.5 μm and lattice constant a of 17.5 μm are obtained. The reflectivity spectra for this lattice at normal incidence are presented in *Figure 3.13*.

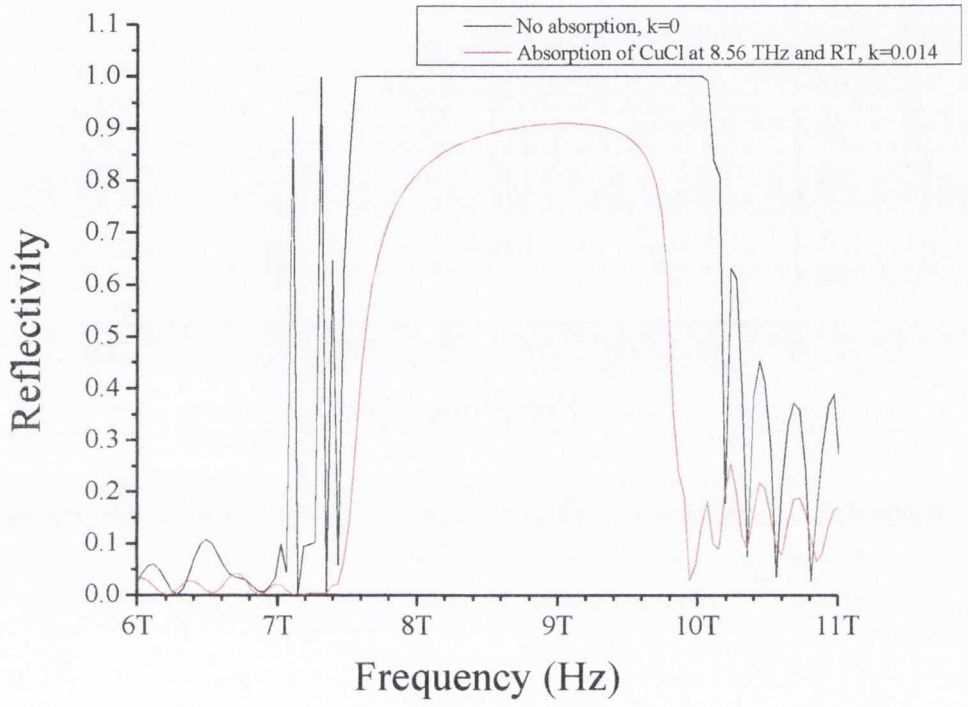

Figure 3.13: *Reflectivity spectra of CuCl PC at 8.56 THz with and without absorption for 16 periods of PC. Due to relatively low absorption in this range of frequencies the reflectivity of CuCl PC reaches 0.9 even at room temperature.*

Again, the black curve shows the idealized case, when the absorption of CuCl is omitted while the red curve shows the realistic case including CuCl absorption. In literature, when addressing THz mirrors, it is often the transmittance spectra that are presented rather the than reflectivity ones [25], [29]. Such an approach is justified, since the calculated reflectance is then compared to the measured values. However, it has to be noted, that in the case of an absorbing mirror a drop in transmittance does not necessarily mean high reflectivity. As was mentioned in the context of band-gap map calculation, the introduction of absorption into the model led to the false broadening of band-gap islands. The transmittance is suppressed by both reflectivity and absorption. In *Figure 3.14* the transmittance spectra of the CuCl PC at 8.56 THz are shown with and without absorption. The band-gap width for both cases is almost equal. The transmittance drops to 0 in both cases, although the reflectivity differs.

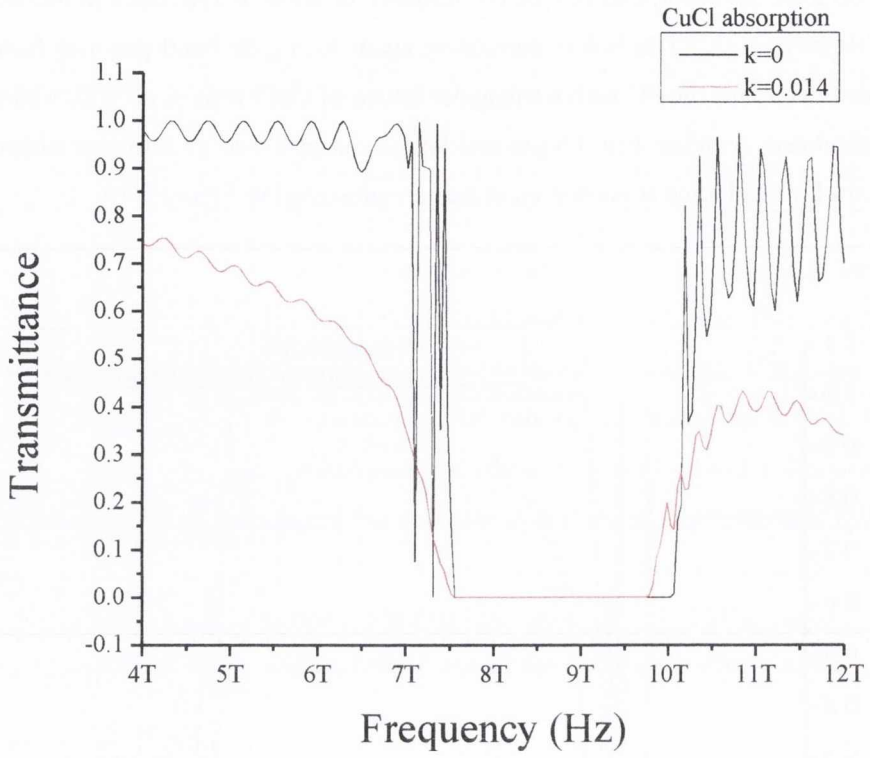

Figure 3.14: *Transmittance of a mirror comprised of 16 periods of the triangular lattice of CuCl PC with and without absorption. In both cases the transmittance is surpassed to negligible within the stop-band. Due to significant CuCl absorption the transmittance outside the stop-band is significantly lowered in reference to idealised non-absorptive case.*

In *Figure 3.15* the transmittance and reflectivity of the same structure is shown as a function of the number of periods forming the mirror.

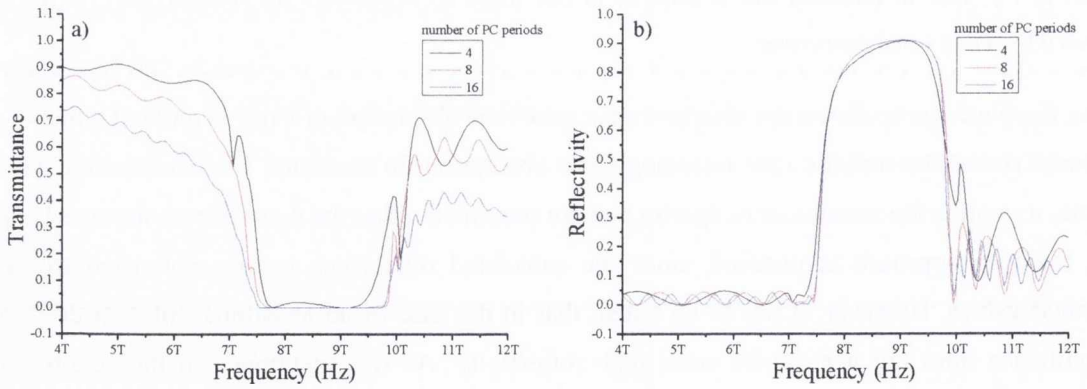

Figure 3.15: *Transmittance and reflectivity spectra of the CuCl PC mirror comprised of different numbers of periods. While the number of periods has limited influence on the reflectivity inside the stop-band, the transmittance outside the stop-band depends on the number of PC periods. Balancing this value the structures suitable for filtering applications can be obtained.*

The reflectivity remains nearly constant for PC periods of 4-16. Number of periods below 14 would not guarantee satisfactory transmittance attenuation within the stop-band. The overall transmittance decreases with an increasing number of periods. This feature can be used in THz filter design. As can be seen in *Figure 3.15b* 4 periods guarantees the maximum reflectivity. The transmittance of the CuCl PC vs PC periods number is shown in *Figure 3.15a*. For frequencies below the stop-band the transmittance reaches 0.9 for higher frequencies, while above the stop-band, the reflectance is lower and remains within the range of 0.6-0.7. Thus a structure built of 4 periods of CuCl PC can be used as a low-pass filter or even as a band filter.

3.4 Conclusions

High interest in THz radiation has generated the need for appropriate materials. HR silicon possesses exceptionally good properties in the THz range, but is a rather expensive solution. The appropriate materials being sought have to be transparent for THz radiation and have a high value of refractive index *n*, preferably constant. In the lower part of the THz range CuCl shows low absorption at cryogenic temperatures and for frequencies over 8THz has relatively low absorption even at room temperature. Apart from HR-Si other THz materials have low absorption only at low THz frequencies often even below 1 THz, such as in the case of steatite or ZrO_2 [28], [49]. The band-gap maps of four CuCl PC structures were calculated. Due to low symmetry the square and inverse square lattices have much narrower band-gaps than the triangular and inverse triangular lattices. The higher band THz band-gap map for the triangular lattice shows band-gap islands occurring only for TM polarised radiation, however the advantage of this geometry is that it contains less of the absorbing medium than the inverse triangular lattice. The widest stop-band occurs for an r/a ratio of ~0.26. The centre of the stop-band is at ~0.44 on a normalised frequency axis with a maximum and minimum value of 0.45 and 0.42, respectively. Taking 8.56 THz as a central frequency the stop-band covers 8.17 THz to 8.75 THz. The width of the island given in r/a dimensionless units provides information on how sensitive the structure is to geometric variations. With the band-gap centred at 0.26±0.2, a variation in the radius between 3.7 μm and 4.3 μm remains within tolerance. If the *r* value shifts to one of these extreme values, the band-gap shifts so that 8.56 THz is at the edge of the band, no longer in the centre. For a fixed radius, the r/a ratio provides information on the tolerance of the lattice constant for the r/a ratio centred at 0.26, and with the normalised frequency varying between 0.42 and 0.45, a lattice variation between 14.7 μm and 15.8 μm can be tolerated. Extraction of these physical parameters shows that the fabrication tolerances are well within the capability of standard material processing techniques and therefore such PC structures can be easily achieved. For the lower THz band, where CuCl has significant absorption, reasonable reflectivity values of almost 0.99 are achievable only at cryogenic temperatures at 3THz. In the higher THz band, over 8 THz, CuCl has moderate absorption and reflectivity of 0.91 is achievable at room temperature at 8.56 THz. Such reflectivity limits the use of CuCl PC mirrors in waveguides, although other applications may be considered. The

transmittance spectra calculated for the same structures show that such a CuCl PC could be used as a filter. Quite high reflectivity and a slight absorption around the photonic band-gap can completely suppress the propagation within band-gap frequencies and can be tailored to transmit out of band-gap frequencies through the structure.

3.5 References

[1] D. van der Weide, "Applications and Outlook for Electronic Terahertz Technology," *Opt. Photonics News*, no. 4, pp. 49-53, 2003.

[2] A. Fitzgerald et al., "Medical applications of broadband terahertz pulsed radiation," in *Lasers and Electro-Optics Society, 2005. LEOS 2005. The 18th Annual Meeting of the IEEE*, pp. 120-121, 2005.

[3] K. Humphreys et al., "Medical applications of terahertz imaging: a review of current technology and potential applications in biomedical engineering," in *Engineering in Medicine and Biology Society, 2004. IEMBS'04. 26th Annual International Conference of the IEEE*, vol. 1, 2004.

[4] J. Handley, A. Fitzgerald, T. Loeffler, K. Seibert, E. Berry, and R. Boyle, "Potential medical applications of THz imaging," *Proc. Medial Image Understanding and Analysis 2001*, pp. 17–20, 2001.

[5] J. F. Federici, D. Gary, R. Barat, and Z. Michalapoulou, "T-Rays vs. Terrorists," *IEEE Spectrum*, pp. 47-52, 2007.

[6] D. G. Allis, J. A. Zeitler, P. F. Taday, and T. M. Korter, "Theoretical analysis of the solid-state terahertz spectrum of the high explosive RDX," *Chem. Phys. Lett.*, vol. 463, no. 1, pp. 84-89, 2008.

[7] L. Moller, J. Federici, A. Sinyukov, C. Xie, H. C. Lim, and R. C. Giles, "Data encoding on terahertz signals for communication and sensing," *Opt. Lett.*, vol. 33, no. 4, pp. 393-395, 2008.

[8] R. Piesiewicz, C. Jansen, D. Mittleman, T. Kleine-Ostmann, M. Koch, and T. Kurner, "Scattering analysis for the modeling of THz communication systems," *IEEE Transactions on Antennas and Propagation*, vol. 55, no. 11, pp. 3002-3009, 2007.

[9] M. C. Beard, G. M. Turner, and C. A. Schmuttenmaer, "Terahertz spectroscopy," *Journal of Physical Chemistry B*, vol. 106, no. 29, pp. 7146-7159, 2002.

[10] S. Lou, T. Guo, H. Fang, H. Li, and S. Jian, "A New Type of Terahertz Waveguides," *Chin. Phys. Lett.*, vol. 23, no. 1, pp. 235-238, 2006.

[11] Y. Kasai and T. Seta, "Terahertz-Wave propagation Model. Atmospheric Propagation Model of Terahertz-Wave," *JNIICT*, vol. 55, no. 1, pp. 73-77, 2008.

[12] G. M. Hale and M. R. Querry, "Optical Constants of Water in the 200 nm to 200 um Wavelength Region," *Appl. Opt.*, vol. 12, no. 3, pp. 555-563, 1973.

[13] A. Hofmann, E. Hörster, J. Weinzierl, L. P. Schmidt, and H. Brand, "Flexible low-loss dielectric waveguides for THz frequencies with transitions to metal waveguides," presented at the European Microwave Conference, Munich, pp. 955-958, 2003.

[14] L. J. Chen, H. W. Chen, T. F. Kao, J. Y. Lu, and C. K. Sun, "Low-loss subwavelength plastic fibre for terahertz waveguiding," *Opt. Lett.*, vol. 31, no. 3, pp. 308-310, 2006.

[15] H. Cao and A. Nahata, "Coupling of terahertz pulses onto a single metal wire waveguide

using milled grooves," *Phys. Lett*, vol. 80, pp. 2634-2636, 2002.

[16] T. I. Jeon, J. Zhang, and D. Grischkowsky, "THz Sommerfeld wave propagation on a single metal wire," *Appl. Phys. Lett.*, vol. 86, p. 161904, 2005.

[17] R. Mendis and D. Grischkowsky, "Undistorted guided-wave propagation of subpicosecond terahertz pulses," *Opt. Lett.*, vol. 26, no. 11, pp. 846-848, 2001.

[18] J. A. Deibel, K. Wang, M. D. Escarra, and D. M. Mittleman, "Enhanced coupling of terahertz radiation to cylindrical wire waveguides," *Trans. Microwave Th. Tech*, vol. 38, pp. 1684-1691, 1990.

[19] J. Weinzierl, C. Fluhrer, and H. Brand, "Dielectric Waveguides at Submillimeter Wavelengths," in *Sixth International Conference on Terahertz Electronics*, pp. 166-169, 1998.

[20] G. Gallot, S. P. Jamison, R. W. McGowan, and D. Grischkowsky, "Terahertz waveguides," *J. Opt. Soc. Am. B*, vol. 17, no. 5, pp. 851-863, 2000.

[21] Y. Chen et al., "Effective surface plasmon polaritons on the metal wire with arrays of subwavelength grooves," *Opt. Express*, vol. 14, no. 26, pp. 13021-13029, 2006.

[22] B. M. A. Rahman, C. Themistos, T. Huda, and K. T. V. Grattan, "Low-loss terahertz waveguides exploiting surface-plasmon modes," in *Proceedings of SPIE*, pp. 67720F-67720F-10, 2007.

[23] K. J. Chau and A. Y. Elezzabi, "Extraordinary Terahertz Transmission through Ensembles of Sub-wavelength Size Metal Particles," in *International Topical Meeting on Microwave Photonics*, pp. 285-288, 2005.

[24] S. Wang, W. Lu, X. Chen, Z. Li, X. Shen, and W. Wen, "Two-dimensional photonic crystal at THz frequencies constructed by metal-coated cylinders," *Journal of Applied Physics*, vol. 93, no. 11, p. 9401, 2003.

[25] N. Krumbholz et al., "Omnidirectional terahertz mirrors: A key element for future terahertz communication systems," *Applied Physics Letters*, vol. 88, no. 20, p. 202905, 2006.

[26] Y. Han et al., "Terahertz supermirrors," in *Infrared, Millimeter, and Terahertz Waves, 2009. IRMMW-THz 2009. 34th International Conference on*, pp. 1–2, 2009.

[27] A. L. Bingham and D. R. Grischkowsky, "Terahertz 2-D Photonic Crystal Waveguides," *IEEE Microwave and Wireless Components Letters*, vol. 18, no. 7, pp. 428-430, 2008.

[28] P. Bolivar et al., "Measurement of the dielectric constant and loss tangent of high dielectric-constant materials at terahertz frequencies," *IEEE Transactions on Microwave Theory and Techniques*, vol. 51, no. 4, pp. 1062-1066, 2003.

[29] C. M. Yee and M. S. Sherwin, "High-Q terahertz microcavities in silicon photonic crystal slabs," *Applied Physics Letters*, vol. 94, no. 15, p. 154104, 2009.

[30] S. Li et al., "Improved Y-splitter photonic crystal waveguides in terahertz regime," *Applied Physics B*, vol. 99, no. 4, pp. 709-716, 2010.

[31] J. Krupka, J. Breeze, A. Centeno, N. Alford, T. Claussen, and L. Jensen, "Measurements of

Permittivity, Dielectric Loss Tangent, and Resistivity of Float-Zone Silicon at Microwave Frequencies," *IEEE Trans. Microwave Theory Techn.*, vol. 54, no. 11, pp. 3995-4001, 2006.

[32] C. Yee, N. Jukam, and M. Sherwin, "Transmission of single mode ultrathin terahertz photonic crystal slabs," *Applied Physics Letters*, vol. 91, no. 19, p. 194104, 2007.

[33] H. Liu, J. Yao, D. Xu, and P. Wang, "Propagation characteristics of two-dimensional photonic crystals in the terahertz range," *Appl. Phys. B*, vol. 87, no. 1, pp. 57-63, 2006.

[34] J. Dai, J. Zhang, W. Zhang, and D. Grischkowsky, "Terahertz time-domain spectroscopy characterization of the far-infrared absorption and index of refraction of high-resistivity, float-zone silicon," *J. Opt. Soc. Am. B*, vol. 21, no. 7, pp. 1379–1386, 2004.

[35] W. Withayachumnankul, B. M. Fischer, S. P. Mickan, and D. Abbott, "Transmission characteristics of T-ray multilayer interference filters," in *Proceedings of SPIE*, pp. 68011G-68011G-15, 2007.

[36] R. Moussa, L. Salomon, F. de-Fornel, J. Dufour, and H. Aourag, "Photonic band gaps in highly ionic medium: CuCl, CuBr, CuI," *Infrared Phys. Technol.*, vol. 44, pp. 27-34, 2003.

[37] A. Hadni, F. Brehat, J. Claudel, and P. Stimer, "Far-Infrared-Active Phonon Processec in CuCl," *J. Chem. Phys.*, vol. 49, pp. 471-473, 1968.

[38] M. Cordona, "Optical Properties of the Silver and Cuprous Halides," *Phys. Rev.*, vol. 129, no. 1, pp. 69-78, 1963.

[39] J. G. Gross, S. Lewonczuk, M. A. Khan, and J. Ringeissen, .

[40] A. Goldmann and D. Westphal, "Band structure and optical properties of CuCl: an angle-resolved study of secondary electron emission," *Journal of Physics C: Solid State Physics*, vol. 16, p. 1335, 1983.

[41] G. Oohata, T. Nishioka, D. G. Kim, H. Ishihara, and M. Nakayama, "Exciton polaritons in bulk CuCl microcavities grown by vacuum deposition," *physica status solidi (c)*, vol. 6, no. 1, 2009.

[42] L. O'Reilly et al., "Room-temperature ultraviolet luminescence from γ-CuCl grown on near lattice-matched silicon," *Journal of Applied Physics*, vol. 98, no. 11, p. 113512, 2005.

[43] A. Mitra, F. O. Lucas, L. O'Reilly, P. J. McNally, S. Daniels, and G. Natarajan, "Towards the fabrication of a UV light source based on CuCl thin films," *Journal of Materials Science: Materials in Electronics*, vol. 18, no. 1, pp. 21-23, 2007.

[44] N. Nishida, K. Saiki, and A. Koma, .

[45] M. Schulz, "The end of the road for silicon," *Nature*, vol. 399, no. 6738, pp. 729–730, 1999.

[46] R. W. Keyes, "Physical limits of silicon transistors and circuits," *Rep. Prog. Phys.*, vol. 68, pp. 2701-2746, 2005.

[47] J. D. Joannapoulos, R. D. Meade, and J. N. Winn, *Photonic Crystals: Molding the Flow of Light*, 2nd ed. Princeton University Press, 2008.

[48] I. A. Khramova and L. A. Melnikov, "Anisotropic photonic crystals: Generalized plane wave method and dispersion symmetry properties," *Opt. Commun.*, vol. 281, pp. 5458-5466, 2008.

[49] W. Fan, H. JiaGuang, Z. ZhiYuan, G. Ming, and J. Te, "The Optical and Dielectric Response of ZrO_2 in Terahertz Region," in *Infrared Millimeter Waves and 14th International Conference on Teraherz Electronics, 2006. IRMMW-THz 2006. Joint 31st International Conference on*, p. 412, 2007.

4 Microcavity LED

4.1 Introduction

The overall performance of electroluminescent devices depends on how efficiently electrical power can be converted into radiation and how effectively the emitted light can be extracted into the surrounding medium. The material quality and device designs are some of the parameters that can be optimised to maximise the efficiency of light emission. As a result of the high contrast between the emitter and surrounding medium refractive indices, the light extraction efficiency remains the major issue. One of the possible techniques to overcome this problem is to place the emitter inside an optical micro-cavity. CuCl as a wide band-gap semiconductor is considered as a potential replacement or competitor for materials like GaN or ZnO. Before a CuCl p-n junction is feasible and built more research on material properties has to be done, even though the simulations of CuCl based light emitters can be already performed. Particularly the issue of light extraction efficiency affected by the refractive index contrast between CuCl and air will be addressed. The high quality of CuCl grown on Si was already demonstrated in chapter 2. Also the crucial parameter for multilayer structures simulations, which is the index of refraction, was obtained and presented in chapter 2. The very high quality of bulk CuCl layers on Si allows us to look towards CuCl based electroluminescent devices even though quantum well (QW) structures involving CuCl are not available yet.

As a result of interaction between the emitted photon and the cavity mode the spectral emission can be altered and the extraction efficiency can be increased [1-4]. The popular wide band-gap semiconductors do not have compatible substrates. The lattice mismatch leads to the big number of threading dislocations affecting devices' performance in terms of longevity and efficiency. Complex growth techniques are needed in order to guarantee satisfactory quality of these materials. CuCl is closely matched with silicon and as such can be easily grown on Si. Thus CuCl based electroluminescent devices are expected to perform well at high temperatures, be easier and cheaper in fabrication and have better performance in term of stability, efficiency and longevity.

4.2 Background

The external quantum efficiency (η_{ext}) can be considered the determinant of the overall light emitter performance, and is given by.

$$\eta_{ext} = \frac{P_{opt}/\hbar\omega}{I/q} = \eta_{inj}\eta_{rad}\eta_{extr} \tag{4.1}$$

where P_{opt} is the emitted optical power, I the injected current, q the electron charge and $\hbar\omega$ the photon energy. As can be seen in *eq. (4.1)* the external quantum efficiency is the product of three factors: the fraction of carriers injected in the active region (η_{inj}), the radiative fraction of spontaneous recombination (η_{rad}) and the extraction efficiency (η_{extr}) [5]. Using the combination of hetero-structures and quantum wells, η_{inj} can approach its upper limit of 1. Additionally, η_{rad} can also reach its theoretical limit of 1, due to advancements in high quality material fabrication and thus a reduction in the number of defects. In practical applications η_{extr} is significantly lower than the theoretical maximum limit of 1 (typically as low as 2-4%) [6], [7]. Thus in order to increase the overall performance of light emitting devices the extraction efficiency issue must be addressed. The influence of the cavity effects for CuCl based structures should be comparable with those of GaN, since both materials have similar values of the refractive index. In case of GaAs the contrast of refractive index with that of the air is higher thus the extraction cone is the narrowest among the mentioned materials, which enables greater improvements to be achieved.

4.2.1 The extraction efficiency

The extraction efficiency is defined as the ratio of the radiation power emitted into the surrounding medium (P_{out}) to the total radiation power emitted within the structure (P_{tot}).

$$\eta_{extr} = \frac{P_{out}}{P_{tot}} \tag{4.2}$$

Two major factors inhibiting the emission of LED structures are substrate absorption and a high refractive index contrast between the emitting medium and the surrounding cladding region. This problem of refractive index contrast is depicted in *Figure 4.1*.

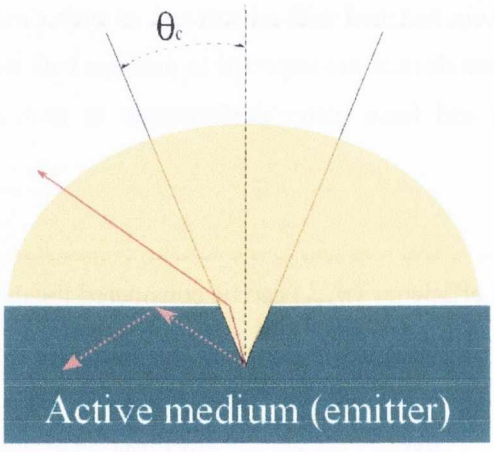

Figure 4.1: *Extraction efficiency of light from emitting medium. Radiation emitted at angles greater than the critical angle (θ_c) undergoes total internal reflection and is lost. Only the fraction of radiation contained within the extraction cone (0° - θ_c) escapes from the emitter.*

Electromagnetic radiation reaches the interface between the emitter and the surrounding medium over a range of angles of incidence, between 0° and 90°. Due to total internal reflection only the fraction of radiation contained within the escape window, the cone of 0° to the critical angle (θ_c), can leave the emitting medium. The critical angle is dependent on the ratio of the refractive indices of the emitting medium (n_m) and the surrounding medium (n_s).

$$\theta_c = \arcsin\left(\frac{n_s}{n_m}\right) \tag{4.3}$$

The remaining radiation is bound within the structure. In order to maximize the extraction efficiency several methods can be applied. One of them is the modification of the emitter surface [7], [8]. The roughened surface increases the likelihood of the photon escape due to surface scattering. Another approach is to use a reflective electrical contact [9]. A highly reflective bottom p-contact acting as a mirror can significantly increase the extraction efficiency. In this case, η_{extr} with a fourfold increase over the bare emitter case has been reported [10]. Alternatively, placing the emitter inside an optical cavity can also significantly improve the extraction efficiency [1], [11], [12] which can be even further improved with more sophisticated structures involving photonic crystals [6], [13]. The photonic crystal structure couples with the guided modes of the cavity semiconductor increasing the extraction efficiency. This combination of the semiconductor microcavity and the photonic crystal embedded within the structures, allows for the highest values of extraction efficiency, approaching the limit of 100% [14].

In this work the potential of light extraction from CuCl based structures will be considered. Firstly, the absorbing substrate will be replaced with a mirror. The refractive index contrast between an emitting medium and substrate is useful in achieving a high reflection coefficient and large bandwidth mirror. In this case only a small fraction of the emitted radiation passes the interface and is coupled to the substrate. The reflected part can be recycled toward the emission interface. The extraction efficiency is significantly improved if the structure is coupled with a material of similar refractive index, as opposed to air having a refractive index of 1.Typically there is a refractive index contrast at the emission interface also, with the whole structure acting as the resonant cavity. The semiconductor cavity modifies the emission profile and improves the extraction efficiency, as will be discussed in detail later in this chapter.

4.2.2 The radiative transitions

In emitting media, particularly semiconductors, the radiative transitions occur as a spontaneous or a stimulated process. The theoretical possibility of stimulated radiation emission was discussed by Einstein in 1916, but it took almost 40 years until it was practically demonstrated. First in the microwave regime as microwave amplification by stimulated emission of radiation (MASER), later, in the visible/UV regime as light amplification by stimulated emission of radiation

(LASER). Einstein postulated that the probability of spontaneous emission (A) is related to the probability of stimulated emission (B) by the following relationship:

$$\frac{A}{B} = 8\pi h \frac{v^3}{c^3} \tag{4.4}$$

where h is Plank's constant, v is electromagnetic radiation frequency and c is the speed of light.

The spontaneous emission probability is given by Fermi's golden rule [15],

$$A = \Gamma_0 = 2\pi\Omega_{ef}^2 \frac{\rho_0(\omega)}{3} \tag{4.5}$$

where Ω_{ef} is the Rabi frequency and $\rho_0(\omega)$ the photon mode density.

$$\rho_0(\omega) = \frac{\omega^2 V}{\pi^3 c^3} \tag{4.6}$$

where V is the quantization volume and c is the speed of light.

The coupling between an atom and the field mode is given by the following relation:

$$\Omega_{ef} = \frac{D_{ef} E_{vac}}{\hbar} \tag{4.7}$$

where D_{ef} is the matrix element of the electric dipole of the atom between two levels and E_{vac} is the vacuum electric field amplitude.

$$E_{vac} = \left(\frac{\hbar\omega}{2\varepsilon_0 V}\right)^{\frac{1}{2}} \tag{4.8}$$

where ε_0 is the free space permittivity and V is the quantization volume. The Rabi frequency of free space Ω_{ef} is the frequency at which the atom and vacuum would exchange the energy if there was only one mode of the field.

If the cavity size is comparable to the wavelength of the radiation, the emission is significantly altered. The emission rate in a cavity (Γ_{cav}) is the product of the free space emission rate (Γ_0) and an enhancement factor.

$$\Gamma_{cav} \cong \Gamma_0 \frac{Q\lambda^3}{V} \tag{4.9}$$

where λ is the wavelength, V is the cavity volume and Q is cavity quality factor defined as:

$$Q = \frac{\omega}{\Delta\omega_c} \tag{4.10}$$

for frequency ω and cavity bandwidth $\Delta\omega_c$.

The ratio of the Rabi frequency and cavity bandwidth determines the characteristics of the light-matter interaction. If the ratio is very low the interaction is negligible or weak. The influence of such a cavity can be treated as a perturbation. The case where Q is high so that $\frac{\Omega_{ef}}{\Delta\omega_c} > 1$ will be discussed in chapter 5. In the following section the case when the cavity finesse is low enough to be considered as perturbative only. Such a case is known as a weak coupling regime.

4.2.3 The influence of microcavity on emission spatial profile

The microcavity can be considered as an optical filter for the emitted radiation. In such a case a modification of the spontaneous emission spatial profile is observed [10]. A schematic drawing of a cavity is presented in *Figure 4.2*.

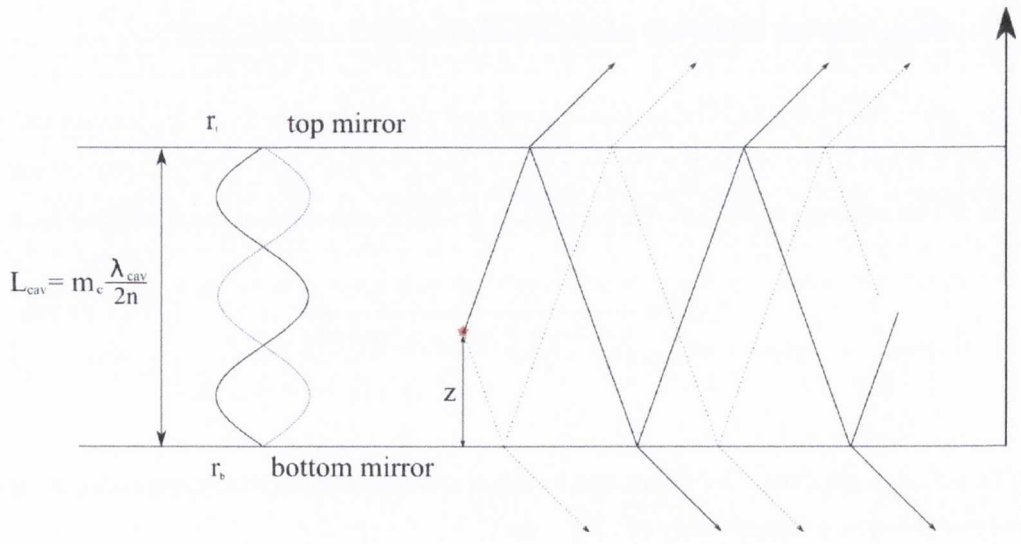

Figure 4.2: *The cavity of length L_{cav} bounded by two mirrors with reflectivities of r_b and r_t. The emitter placed at a distance z from the bottom mirror emits two series of waves. In the above example the cavity length is of $\frac{3\lambda}{2}$.*

The cavity consists of a bottom mirror of reflectivity r_b and a top mirror of reflectivity r_t. The emitting medium between the mirrors has a refractive index of n. The emitting dipole is placed at a distance z from the bottom mirror. The cavity length L_{cav} is given by the following relation:

$$L_{cav} = m_c \frac{\lambda_{cav}}{2n} \tag{4.11}$$

where m_c is an integer number, n is the active medium refractive index and λ_{cav} is the vacuum wavelength of the cavity. The emission field at the front of the cavity is defined by the equation:

$$|E_{out}|^2 = |E_{in}|^2 \times \xi \times \frac{T_t}{|1 - r_b r_t e^{2i\phi}|^2} \tag{4.12}$$

where $2\phi = 2kL_{cav}\cos\theta$ is a round trip phase shift and $k = \frac{n\omega}{c} = \frac{2\pi n}{\lambda}$. The nominator of the last term in equation (4.12), T_t, is the top mirror transmission coefficient, $T_t = 1 - r_1^2$.

The term ξ is known as the antinode factor and is defined as:

$$\xi = 1 + r_b^2 \pm 2r_b \cos(2\phi') \tag{4.13}$$

where r_b is the back mirror reflectivity and $\phi' = \frac{2\pi n}{\lambda} z \cos\theta$.

As can be seen, *equation (4.12)* takes into account the dipole distance from the bottom mirror, *z*, and the angle between the emitted radiation and the cavity vertical axis. The last term on the right hand side of this equation is the Airy-Factor (ξ_{Airy}). It can be expressed in the simplified form:

$$\xi_{Airy} = \frac{T_t}{1 + (r_t r_b)^2 - 2r_t r_b \cos(2\phi)} \tag{4.14}$$

In *Figure 4.3* there are three Airy-factor curves calculated for different top mirror reflectivities and thus corresponding to different cavity finesse values.

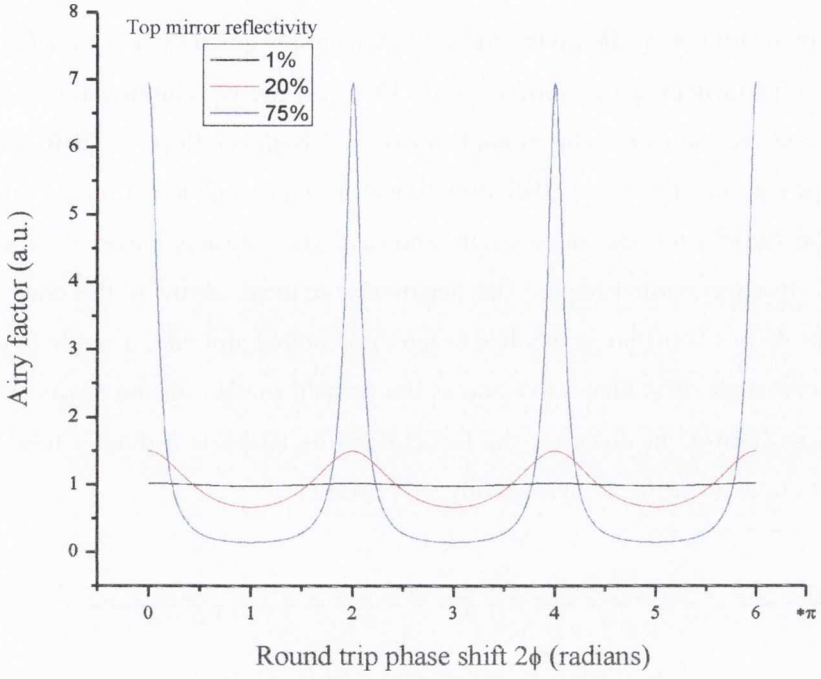

Figure 4.3: *Airy factor calculated for three different top mirror reflectivity values. The blue curve shows the high finesse case, where the periodicity of Airy factor is clearly visible. For the lower finesse cavity the periodicity is still clear, but the peaks become broader and the intensity decreases which is shown with the red curve. For the low reflectivity mirror of 1% the periodicity of Airy factor is almost negligible and the influence of a cavity vanishes.*

For the low finesse cavity there is no noticeable periodicity which becomes apparent and increases with increasing cavity finesse. The curves in *Figure 4.3* represent the normal incidence case. Thus for $\theta = 0$ the relationship $\frac{4\pi n}{\lambda} L_{cav} = 2\pi m$ states that the Airy-Factor maxima occur at an integer m, and further to this, that the optimal cavity length is given for $L_{cav} = \frac{\lambda}{2n} m$, where $\frac{\lambda}{n}$ is the wavelength inside the cavity of refractive index n. The result of Airy-factor periodicity is that the cavity favours particular wavelengths at particular angles. The antinode factor takes into account the dipole position inside the cavity. The constructive interference occurs when $\frac{4\pi n}{\lambda} z = 2\pi m$ and $z = \frac{m\lambda}{2n}$. Thus even multiples of $\frac{\pi}{2}$ contribute in the case of $\xi = 1 + r_b^2 + 2r_b \cos(2\phi')$ and odd multiples give constructive interference for antinode factor of the form $\xi = 1 + r_b^2 - 2r_b \cos(2\phi')$.

Figure 4.4 illustrates the results of the above considerations showing the power emitted on the top mirror side as a function of the angle. This model assumes the emitter is an infinitesimally thin layer. For all three cases of this simulation the emitter is placed exactly in the middle of the active region exactly between the mirrors. As was defined in the above model, the distance between the bottom mirror and the emitter is denoted as z. The cavity length, L_{cav} is the parameter

which varies in the simulation. The tuned 1λ cavity has a length of 184 nm which corresponds to a wavelength of 387nm in vacuum, corresponding to the peak emission wavelength for CuCl. Since the emitter is placed in the middle of the cavity, the z in each case is given by $z = L_{cav}/2$. The red curve in *Figure 4.4* is the farfield spatial profile of the 1λ tuned cavity. The detuning is done by varying the distance between mirrors. The bottom mirror is a highly reflective DBR stack with reflectivity near 1. The top mirror is also a DBR stack however, with much lower reflectivity below 0.5. The shape of the farfield for the tuned cavity shows slight splitting however most of the emission is centered near the normal angle. The negatively detuned cavity is the cavity of the length $L_{cav} = 164nm$. In this case almost whole emission is centered around the single lobe with a maximum at the normal angle. The blue curve shows the farfield profile for the cavity positively detuned, where $L_{cav} = 204nm$. In this case the farfield profile shape is a double lobe and the power emitted at the normal angle, 0^0, is significantly suppressed.

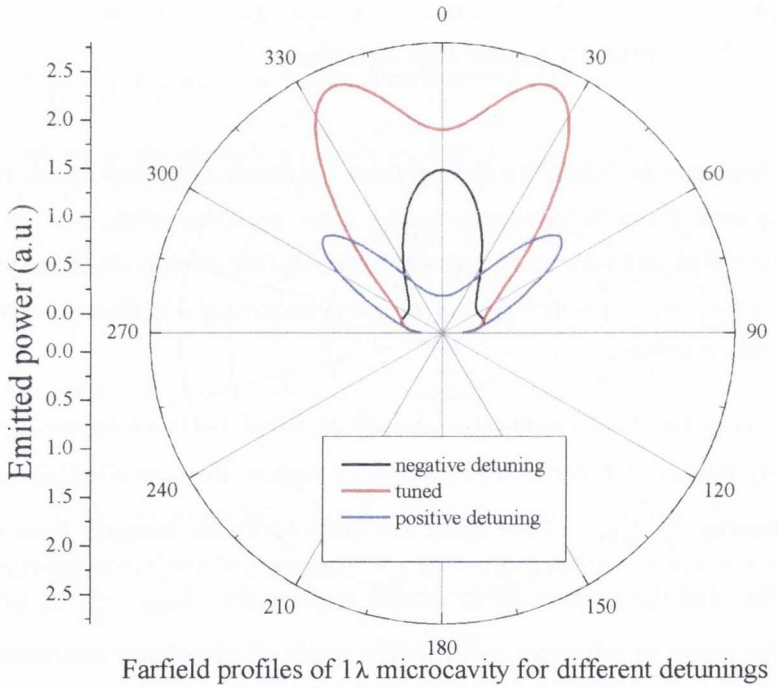

Farfield profiles of 1λ microcavity for different detunings

Figure 4.4: *Farfield profiles of three detunings of the near 1λ cavity. The single emitter is placed in the middle of the cavity. As can be seen the maximum emission is achieved with the tuned cavity. Also the majority of emission is concentrated within the cone of approximately 0°-30°. Both positive and negative detuning modify the angular dependence of emission and decrease the total emitted power.*

The emitter is placed exactly in the antinode of the cavity for the tuned cavity. In this case both antinode factor and Airy factor have maxima. Both detuned cavities are not integer multiples of λ/2 thus the central emitter is not placed in the antinode anymore at normal incidence. The plot from *Figure 4.4* is used in the extraction efficiency calculation. Total power emitted into the medium is

an integral through all wavelengths and all angles of power emitted. In the 1λ case depicted in *Figure 4.4* the maximum of extraction efficiency occurs for the tuned cavity (red curve). Both positively and negatively detuned cavities have lower extraction efficiencies.

The next section addresses the transfer matrix method which is used in the modeling of multilayer structures.

4.3 The transfer matrix model

In order to simulate the behaviour of a multilayer structure, a suitable model must be chosen. The refractive index yields information about the propagation of an electromagnetic field within the material. According to Snell's law the angle of incident a radiation is related to the angle of the refracted radiation by their refractive indices.

$$\frac{\sin\theta_1}{\sin\theta_2} = \frac{n_2}{n_1} = \frac{v_1}{v_2} \tag{4.15}$$

The group speed of electromagnetic waves within a material depends on the refractive index values, $n_1 \ldots n_y$ and is denoted by v_1 and v_2. The wavelength in the material is given by the wavelength in vacuum, λ_0 divided by the refractive index of this materal, n.

$$\lambda_m = \frac{\lambda_0}{n} \tag{4.16}$$

Based on these relations the propagation of electromagnetic radiation within a multilayered structure can be modelled. *Figure 4.5*, below, illustrates various scenarios possible in a simple two layer structure.

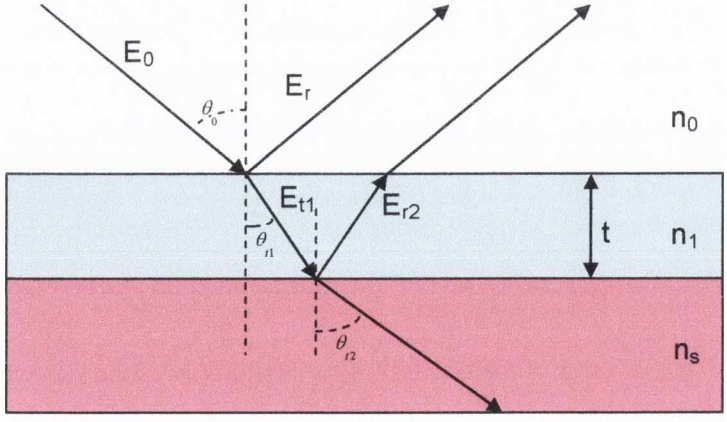

Figure 4.5: *Simple two layer structure with refractive indices n_1 and n_s, surrounded by a medium of refractive index n_0. The arrows show the propagation of electric field within the structure. Knowing the refractive indices and the layer thicknesses the propagation of the electric field can be calculated.*

The system in *Figure 4.5* consists of a thin layer of material with refractive index n_1 and thickness t, a substrate of refractive index n_s, a surrounding medium with refractive index n_0. The angle of incidence of electromagnetic field E_0 is θ_0. The refracted field angle changes in material and in substrate to θ_{t1} and θ_{t2}, respectively. The sum of the reflected, refracted and absorbed fields has to be equal to the initial field E_0.

The propagation of an electromagnetic field then can be described by matrix relations [16]. This approach is known as the Transfer Matrix Model (TMM) [16] where each layer is represented by a 2x2 matrix $\Re_i$.

$$\Re_i = \begin{bmatrix} m_{11} & m_{12} \\ m_{21} & m_{22} \end{bmatrix} \tag{4.17}$$

The matrix elements $m_{11} \ldots m_{22}$ for each layer can be calculated as follows:

$$m_{11} = \cos\delta \tag{4.18}$$

$$m_{12} = \frac{i \sin\delta}{\gamma_1} \tag{4.19}$$

$$m_{21} = i\gamma_1 \sin\delta \tag{4.20}$$

$$m_{22} = \cos\delta \tag{4.21}$$

$$\delta = \left(\frac{2\pi}{\lambda_0}\right) n_1 t \cos\theta_{t1} \tag{4.22}$$

Where n_1 is the refractive index of the material, ε_0 is permittivity of the vacuum, μ_0 is the vacuum permeability, t is the layer thickness and θ_{ti} is the transmitted beam angle.

Depending on the polarisation γ_1, it will take the form of either

$$\gamma_1 = n_1\sqrt{\varepsilon_0\mu_0}\cos\theta_{t1} \tag{4.23}$$

for the perpendicular plane of incidence ($\vec{E}_\perp$) or

$$\gamma_1 = n_1\frac{\sqrt{\varepsilon_0\mu_0}}{\cos\theta_{t1}} \tag{4.24}$$

for the parallel plane of incidence ($\vec{E}_\parallel$).

So finally for an $n=1..N$ layer structure the resulting electromagnetic field is obtained by:

$$\left[\frac{E_a}{B_a}\right] = \Re_1\Re_2\Re_3 \ldots \Re_N\left[\frac{E_n}{B_n}\right] \tag{4.25}$$

And the final transfer matrix will take the form of the product:

$$\Re_T = \Re_1\Re_2\Re_3 \ldots \Re_N \tag{4.26}$$

The transmission and reflection coefficients dependence on the matrix elements is given:

$$t = \frac{2\gamma_0}{\gamma_0 m_{11}+\gamma_0\gamma_s m_{12} + m_{21} + \gamma_s m_{22}} \tag{4.27}$$

$$r = \frac{\gamma_0 m_{11}+\gamma_0\gamma_s m_{12} - m_{21} - \gamma_s m_{22}}{\gamma_0 m_{11}+\gamma_0\gamma_s m_{12} + m_{21} + \gamma_s m_{22}} \tag{4.28}$$

where:

$$\gamma_0 = n_0\sqrt{\varepsilon_0\mu_0}\cos\theta_0 \tag{4.29}$$

$$\gamma_s = n_s\sqrt{\varepsilon_0\mu_0}\cos\theta_{r2} \tag{4.30}$$

And thus the reflectance of the structure will take the form:

$$R = |r|^2 \tag{4.31}$$

4.4 Modelling the light extraction

As was mentioned it is possible to increase the extraction efficiency from a high refractive index medium by placing the active medium inside an optical cavity. In order to calculate the extraction efficiency an approach discussed in [17], [10], [18] can be used. The presented model allows for the calculation of emission patterns in multilayered structures. The source field is placed inside the structure. Two multilayered structures on both sides of the source can then be described by transfer matrices. As a result of the refractive index differences, the unit solid angle changes from layer to layer

$$\frac{d\Omega_1}{d\Omega} = \frac{n^2 \cos\theta}{n_1^2 \cos\theta_1} = \frac{n k_z^2}{n_1 k_{z,1}^2} \tag{4.32}$$

where n and n_1 are refractive indices of two neighboring layers, k_z and $k_{z,1}$ are wave vectors.

Furthermore, the power per unit solid angle per unit surface can be defined

$$\Pi = \frac{dP}{d\Omega dS} = |E_{out}|^2 \frac{n k_z^2}{n_1 k_{z,1}^2} \tag{4.33}$$

where $|E_{out}|^2$ means outside fields.

The wave vector can be calculated for each layer

$$k_{z,j}^2 + k_{\parallel}^2 = \frac{\omega^2}{c^2} n_j^2 \tag{4.34}$$

and $k_{\parallel}$ is conserved through all layers. In the model $k_{\parallel} = n_0 \sin\theta_0$.

Finally the extracted power can be calculated by the following integration:

$$P_{extrac} = \int_0^{\frac{\pi}{2}} 2\pi\Pi(\theta) \sin\theta d\theta \qquad (4.35)$$

In a more realistic case, for example if the emission line shape is approximated by a Gaussian, the integrals have to be normalised and summed with appropriate weights. In what follows we apply this model to a CuCl multilayer structure, which can be considered as a weakly coupled planar microcavity with a view to investigating the optimization of the extraction efficiency. The extraction efficiency is the ratio of power emitted in vacuum to the power extracted from the structure.

The planar microcavity structure consists of a pair of mirrors separated by distance L_c with the cavity length comparable to the wavelength $L_c \sim \lambda$. In practice the distance between mirrors is filled with an emitting semiconductor material. As discussed above the microcavity structure can modify the emission profile. The interference effects within the cavity modify the internal angular power distribution. The preferential propagation direction of radiation can be changed so that the bigger part of emitted radiation can fit within the extraction window and increase η_{extr} [5].

The mirror

The simplest microcavity consists of a semiconductor material, in this case CuCl, sandwiched between two planar mirrors. There are different possible materials and material structures that can be used as mirrors. Sometimes, as is the case for some laser diode structures, the interface of the cavity medium and surrounding medium has satisfactory reflectivity. Usually, cleaved surfaces have rather low reflectivity. In the case of a CuCl/air interface the reflectivity is ~15% at the peak emission wavelength of 387 nm. Higher reflectivity can be achieved with metallic mirrors. A layer of metal, like Al or Au can have a reflectivity of 95%, but higher values are difficult to obtain with this type of mirror. The metallic layers are easily deposited and can provide high, and almost constant, reflectivity across a wide range of wavelengths, but in some applications reflectivity near 100% is required. The distributed Bragg reflector (DBR) can be designed to meet criteria with almost 100% reflectivity in some range of wavelengths.

The DBR is a periodic stack of low and high refractive index materials. Such a structure forbids the propagation of electromagnetic radiation within a stop band. The thicknesses of the layers, and material refractive indices, determine this forbidden band. For DBRs constructed using two materials each layer is $\frac{\lambda}{4}$ thick. The electric field within the DBR structure is shown, for an example structure, in *Figure 4.6*.

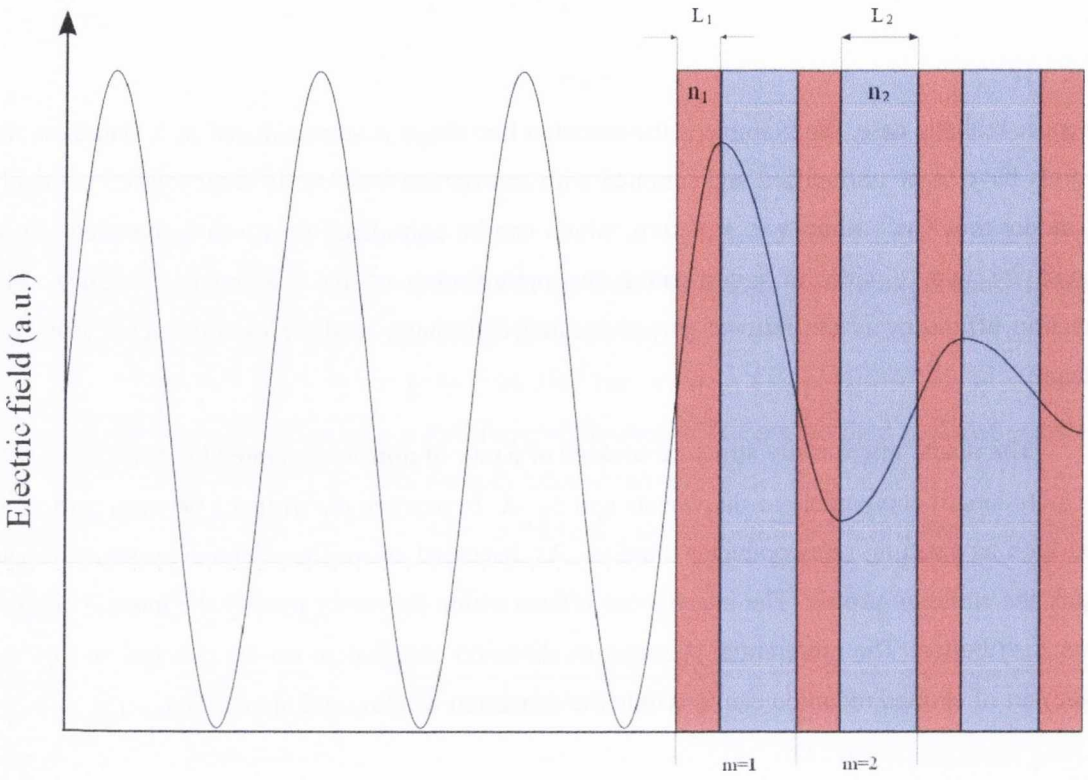

Figure 4.6: *The electric field within the DBR structure. The mirror is built of 3.5 layer pairs of thickness L_1 and L_2 and refractive indices n_1 and n_2, respectively. The electromagnetic wave freely propagating in vacuum undergoes the reflection from every interface thus the amplitude of the field decreases along the structure.*

In the example the mirror is built of m=3.5 pairs of L_1 and L_2 thick layers of materials having refractive indices n_1 and n_2, respectively. As can be seen there is some penetration of the field into the DBR. The reflectivity of the DBR can be calculated with the transfer matrix model described in section 4.3. For the number N of reflective pairs the reflectance at normal angle can be given:

$$R = \left[\frac{n_0(n_2)^{2N} - n_s(n_1)^{2N}}{n_0(n_2)^{2N} + n_s(n_1)^{2N}}\right]^2 \tag{4.36}$$

where n_0 is the refractive index of the surrounding medium, n_1 and n_2 are the refractive indices of the two materials constituting the mirror, n_s is the refractive index of the substrate on which the mirror is deposited, and N is the number of reflective pairs. The stop-band of a single pair is expressed as follows:

$$\Delta\lambda_0 = \frac{4\lambda_0}{\pi}\arcsin\left(\left|\frac{n_2 - n_1}{n_2 + n_1}\right|\right) \tag{4.37}$$

where λ_0 is the central wavelength of the stop-band and n_1 and, n_2 are the refractive indices of the DBR layers.

4.5 CuCl on Si Substrate

Firstly, the as-grown structure of a layer of CuCl on a Si substrate can be considered. The diagram in *Figure 4.7* shows the basic structure of a modeled CuCl on Si with refractive index values given for the central wavelength of CuCl excitonic emission (387 nm). It should be noted that we are considering bulk CuCl structures and the descriptions above have been developed for emitters in an infinitesimally thin layer placed at specific positions within the cavity, whereas in what follows we consider bulk CuCl layers.

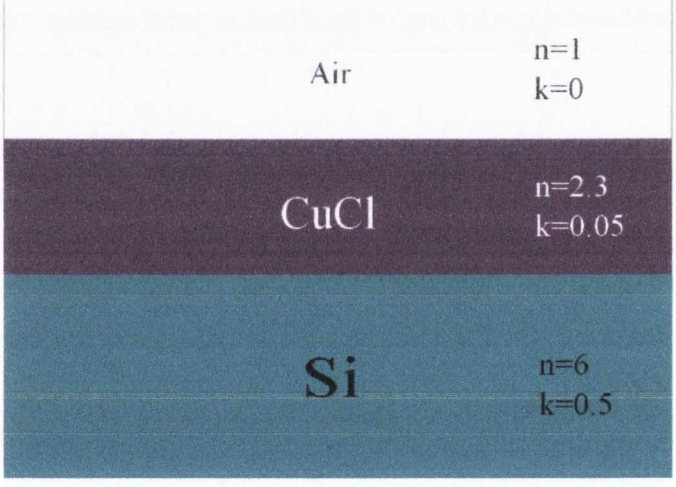

Figure 4.7: *Schematic drawing of a CuCl on Si basic structure, with refractive indices of materials marked on the right hand side. The typical layer of CuCl is in the range of 50-500 nm.*

The value of η_{extr} for the bare emitter in a medium emitting into air is expressed as $\eta_{extr} = 1/4n^2$[10], where n is the refractive index of the medium. This value is as low as 4.7% for CuCl emitting into air. The aim of this chapter is to investigate by how much the value of η_{extr} can be increased for bulk CuCl structures.

The dispersive values of the complex refractive indices of materials presented in *Figure 4.8* were used for all simulations.

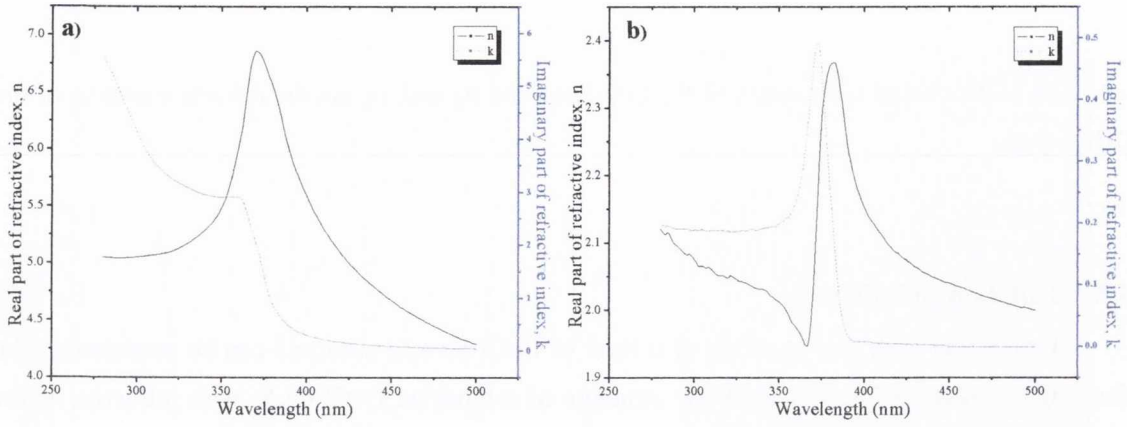

Figure 4.8: *The complex refractive indices of Si (a) and CuCl (b).The real parts of the refractive indices are presented in black on the left hand side of the figures while imaginary parts are plotted with dotted blue lines and marked on the right hand side.*

As can be seen, at the wavelength of CuCl excitonic emission, silicon exhibits significant absorption. The value of the imaginary part of the refractive index reaches 0.55 and increases with decreasing wavelength.

Firstly the extraction efficiency, η_{extr} as a function of the CuCl layer thickness is presented in *Figure 4.9*, with the assumption that the emitter is an infinitesimally thin layer. The emitter is placed in the middle of the CuCl layer for all thicknesses. The figure shows the dependence of the extraction efficiency on the emitter position for CuCl. As the thickness changes the cavity moves in and out of resonance with the emission, which causes a variation in the extraction efficiency, as described above in *section 4.2.3*. The CuCl layer thickness considered in this analysis varies between 50 and 500 nm. This range of thicknesses is achievable with the vapor deposition technique and as such was the subject of interest. The overall decrease of the extraction efficiency with increasing thickness is due to the absorption in the CuCl intra-cavity layer.

As was already discussed in paragraph 4.2.3 the emission spatial pattern also depends on the emitter position inside the cavity. Thus the extraction efficiency as a function of the emitter position in the CuCl layer for a fixed cavity thickness of 490 nm is shown in *Figure 4.10*

A CuCl layer that is 410 nm thick corresponds to cavity length of $\frac{9\lambda}{4}$. A periodic variation of the extraction efficiency is observed, again with an overall decrease as the emitter is placed deeper in the CuCl layer.It is seen that even the simple structure presented in *Figure 4.7* constitutes an optical cavity. The interfaces: active medium/substrate and active medium/air act as the mirrors.

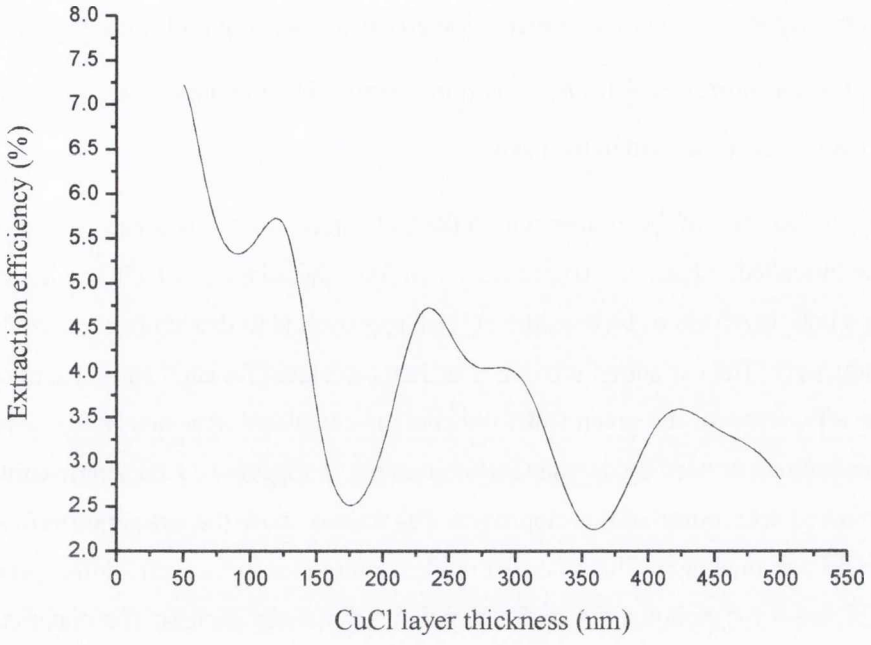

Figure 4.9: *Calculated extraction efficiency as a function of CuCl layer thickness in a CuCl on Si substrate, emitting into air. The emitter is an infinitesimally thin layer in the middle of CuCl.*

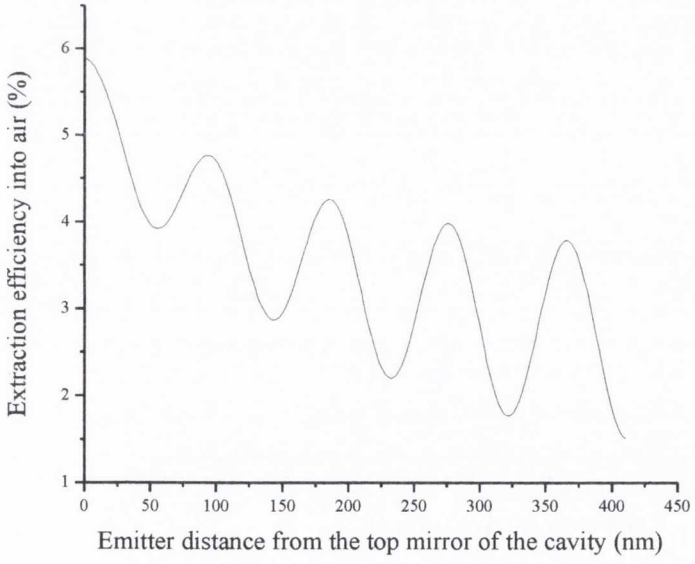

Figure 4.10: *Extraction efficiency of 410nm thick CuCl on Si vs emitter position inside the CuCl layer. The maxima of extraction efficiency correspond to the antinode emitter position while the node position gives minima in extraction efficiency.*

The reflectivity of CuCl/air interface is 15.5% and for CuCl/Si is 20% at 387nm. Since the refractive index of Si is higher than that of CuCl the wave reaching the interface experiences the

phase shift of 180°, thus the length of the cavity has to be an odd multiple of $\frac{\lambda}{4}$ in order to enable constructive interference. The maxima of extraction efficiency occur at multiples of $\frac{\lambda}{2}$ starting from the position at the top mirror or $\frac{\lambda}{4}$ from the bottom mirror. The maxima in extraction efficiency correspond to antinodes of the field in the cavity.

Clearly the position of the emitter within the CuCl intra-cavity layer can yield a substantial variation in the modelled extraction efficiency. Therefore, the adaption of the model to simulate emission from a bulk layer has to be considered. One approach is to distribute emitters throughout the emitting bulk layer. The extraction efficiency is then calculated for each emitter separately. The final extraction efficiency for the given CuCl thickness is calculated as a sum of efficiencies from the contributing emitters divided by the number of emitters. In *Figure 4.11* the single emitter model results are compared with multi-emitter approach. The curves show the extraction efficiency as a function of CuCl layer thickness. The modified model results in a curve with similar periodicity to that shown in *Figure 4.10*, though the overall extraction efficiencies are less. The maxima occur for CuCl layer thickness of multiple $\frac{\lambda}{2}$ shifted by $\frac{\lambda}{4}$.

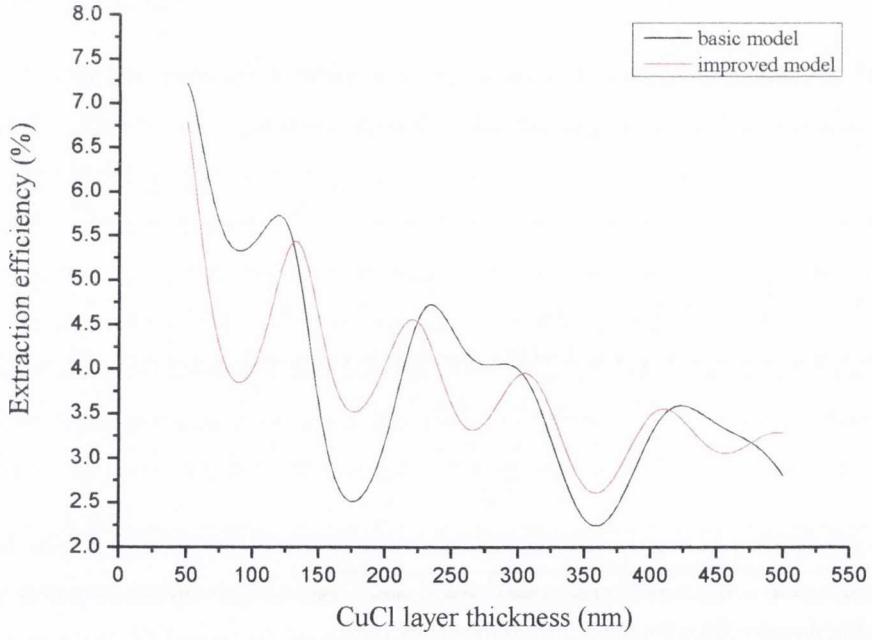

Figure 4.11:*The comparison of the extraction efficiency of CuCl on Si for both models. The black curve shows the extraction efficiency calculated for the emitter position fixed at half CuCl layer thickness while the red curve shows the more accurate approach taking into account the radiation emitted from the whole CuCl volume.*

Another issue that has to be considered is the absorption of the substrate. As previously shown in *Figure 4.8* the silicon is absorbing in the UV/blue range of wavelengths. The absorption coefficient of silicon at 387 nm is of the order of 10^5/cm. In *Figure 4.12* the influence of silicon absorption on extraction efficiency is shown.

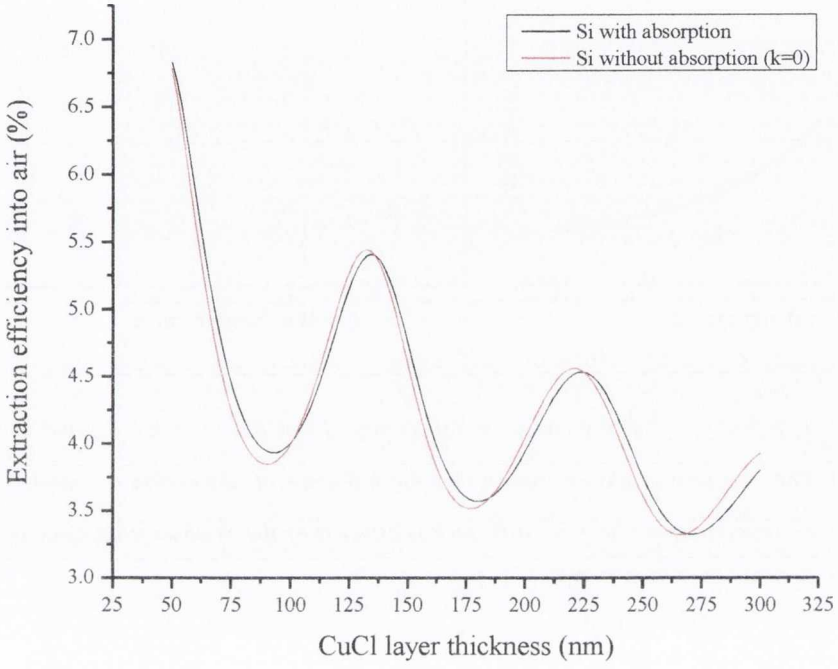

Figure 4.12: *The influence of Si absorption on extraction efficiency. The losses due to Si absorption are not significant since the radiation which passes the CuCl/Si interface is lost regardless it is absorbed within the substrate or not.*

Both curves are calculated using the multi-emitter model. The black curve shows the extraction efficiency calculated using the silicon refractive index presented in *Figure 4.8*. The red curve shows the extraction efficiency calculated with the assumption that the imaginary part of the silicon refractive index is 0. As can be seen, the extraction efficiency is not significantly suppressed by the fact of strong Si absorption. The reflectivity of the CuCl/Si interface is only 20% thus most of the radiation incident on this interface is transmitted and cannot be subsequently extracted through the front of the structure. The transmitted fraction of the emitted radiation has to be considered as lost regardless of whether it is absorbed by the substrate or emitted through the back of the thick Si substrate. Consequently, the absorption of silicon does not affect the reflectivity on a single CuCl/Si interface. However to improve the extraction efficiency of the CuCl structure, the light currently lost via transmission into the Si layer must be recovered.

Given the good lattice match between Si and CuCl, which can allow for the growth of a good quality CuCl layer, the above discussion can be extended to consider the possibility of a

CuCl/Si based DBR. In *Figure 4.13* the influence of Si absorption on the reflectivity of a single CuCl/Si interface and for a CuCl/Si 6 pairs $\frac{\lambda}{4}$ DBR stack is shown.

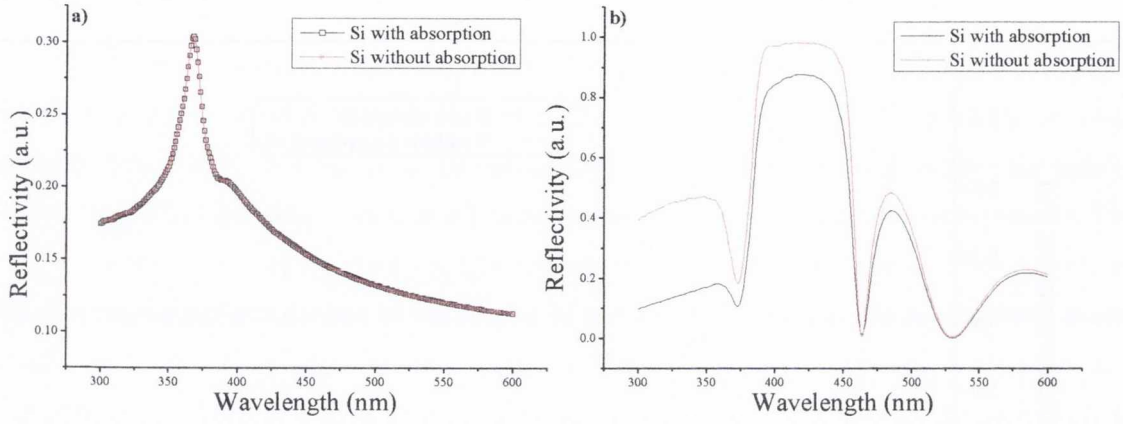

Figure 4.13: *The influence of Si absorption on reflectivity of CuCl/Si interface (a) and CuCl/Si 6 pairs* $\frac{\lambda}{4}$ *DBR stack (b). The comparison clearly shows that the influence of absorption on single CuCl/Si interface is negligible. The reflectivity of CuCl/Si DBR stack is affected by the Si absorption since radiation has pass through the number of absorptive Si layers.*

Figure 4.13a shows the reflectivity of a CuCl/Si interface. The black curve in *Figure 4.13a* is calculated for the refractive index of materials presented in *Figure 4.8*. The red shows the reflectivity of the interface if Si was non-absorptive (k=0). These curves actually overlap over a whole range of presented wavelengths thus the absorption of a Si does not affect the reflectivity of a single interface. The example stack of six $\frac{\lambda}{4}$ pairs of CuCl and Si shows the importance of absorption. In *Figure 4.13b* the curves calculated with (black) and without (red) absorption are presented. The suppression of the reflectivity by absorption is obvious, which while offering a possibility to improve the overall structure, the extraction efficiency will still have a compromised performance. The next step of simulation is to consider removing the absorbing substrate after growth of the CuCl layer and to replace it with other mirror options.

The different stages to be considered are presented in *Figure 4.14*. Firstly the Si substrate has to be removed, and then this region can be infilled with either a single material or multi-layers forming a DBR.

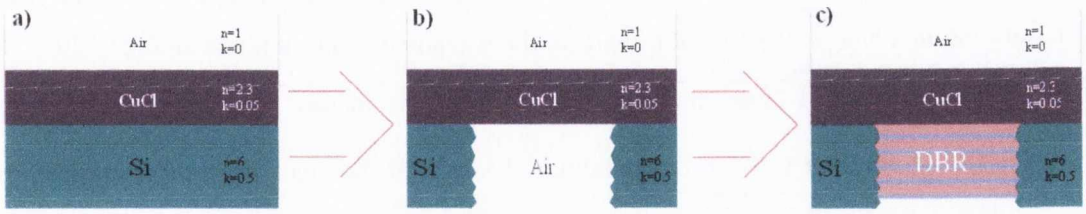

Figure 4.14: *Consecutive steps illustrating the replacement of Si substrate with a DBR structure. The silicon substrate is firstly etched (a) and then substituted with the DBR.*

Figure 4.15 shows a comparison of the extraction efficiency between the basic sample and that with the substrate removed. The curves show extraction efficiency as a function of CuCl layer thickness. Both curves look similar, but shifted. The important parameter is the distance of the emitter according to the bottom mirror. As can be seen for the CuCl on Si structure, the first maximum of extraction efficiency occurs at $\frac{\lambda}{4}$ distance from the bottom mirror.

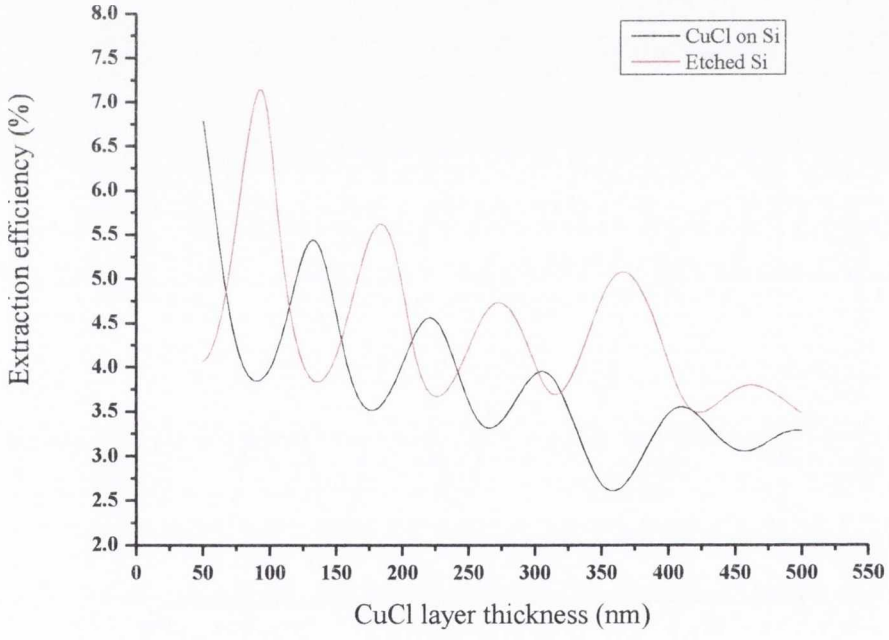

Figure 4.15: *Calculated extraction efficiency of light in CuCl on Si structure and CuCl in air (wih etched silicon). The reflectivities of both CuCl/air and CuCl/Si are similar thus the extraction efficiency values achieved in both cases are similar. The mismatch of maxima/minima positions for both curves originates in the phaseshift of electromagnetic radiation on CuCl/Si interface which is not a case for CuCl/air.*

For the CuCl in air case the first maximum occurs at the bottom mirror. The maxima of extraction efficiency of the etched sample occur approximately where CuCl on Si has the minima. Both

interfaces, CuCl/Air and CuCl/Si, are reflective as already mentioned. The difference in phase comes from the fact that on the CuCl/Si interface the wave undertakes a phase shift of 180°. The optical length of the CuCl layer thickness has to be of the integer multiplicity of $\frac{\lambda}{2}$ (even multiplicity of $\frac{\lambda}{4}$). In order to fulfil this condition, because of the mentioned phase shift on the interface, CuCl layer on Si has to be of the odd multiplicity of $\frac{\lambda}{4}$.

Figure 4.16 shows the extraction efficiency plots for two different structures. The black curve shows the extraction efficiency from 410 nm thick CuCl layer on Si as a function of emitter position (the distance of emitter from the top of the CuCl layer). The thickness of 410 nm corresponds to $\frac{9\lambda}{4}$ for λ = 387nm in vacuum. The red curve shows the same dependence of extraction efficiency on the emitter position in the structure of 366 nm CuCl in air (etched substrate). The thickness of 366 nm corresponds to $\frac{8\lambda}{4} = \frac{4\lambda}{2}$.

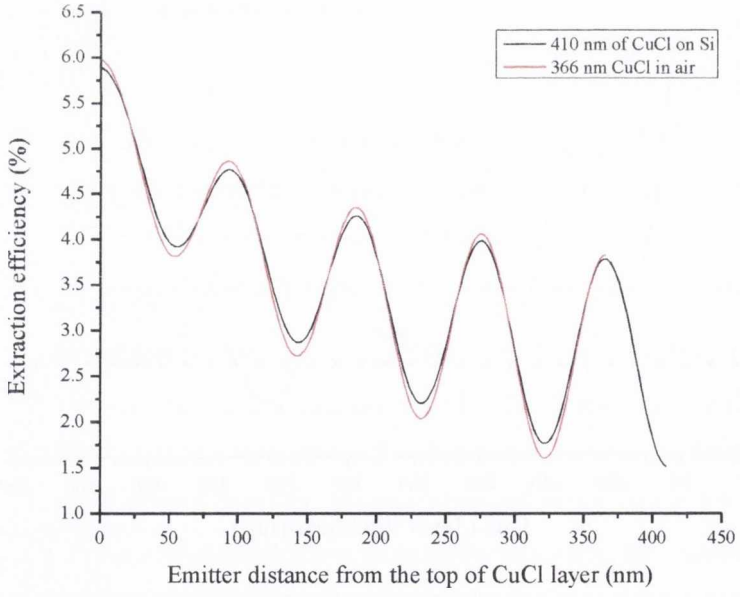

Figure 4.16: *Extraction efficiencies of CuCl on Si and CuCl in air vs the emitter position inside the CuCl layer. In these figures previously discussed phaseshift is clearly visible. Also the corresponding maxima and minima of extraction efficiency almost overlap for both curves.*

As can be seen, maxima in both cases occur at the same positions with respect to the top of the CuCl layer. Also the extraction efficiency values are very close for corresponding maxima. This fact is consistent with the reflectivity values of CuCl/Si and CuCl/air interfaces being of 20% and

15.5%, respectively. All the analysis to date indicates that a higher reflectivity interface must be implemented if the extraction is to be significantly improved.

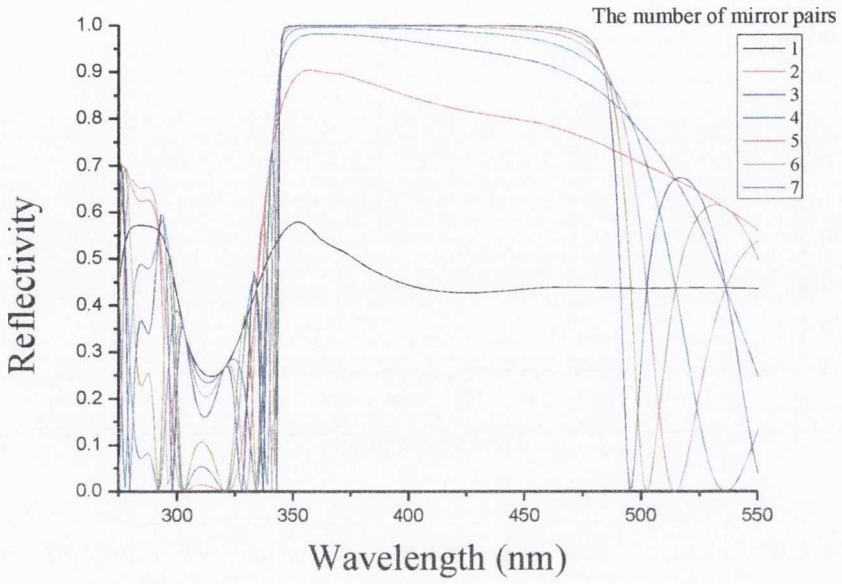

Figure 4.17: *The reflectivity of DBR as a function of wavelength for 1 to 7 SiO2/TiO2 pairs. The stack of 7 pairs of SiO2/TiO2 guarantees the maximum reflectivity. Further increase of DBR pairs increases the complexity but not the reflectivity.*

This can be achieved by placing the DBR structure on the bottom of the CuCl layer. SiO_2 and TiO_2 are chosen as the materials to form a DBR. These materials have a high refractive index contrast and thus the number of pairs required to achieve a high level reflectivity is relatively low. In *Figure 4.17* the reflectivity of a SiO_2/TiO_2 DBR is plotted as a function of wavelength for different numbers of SiO_2/TiO_2 pairs.

The mirror was designed for the central wavelength of CuCl excitonic emission at 387 nm. The thickness of SiO_2 was determined to be 66 nm, with a refractive index of 1.47 at 387 nm, whilst the thickness of TiO_2 is 28 nm and has a refractive index of 3.41 at 387 nm. As the reflectivity of the DBR does not increase significantly above 5 SiO_2/TiO_2 pairs this number was chosen as optimal. The extraction efficiencies of all three structures presented in *Figure 4.14* are shown in *Figure 4.18*.

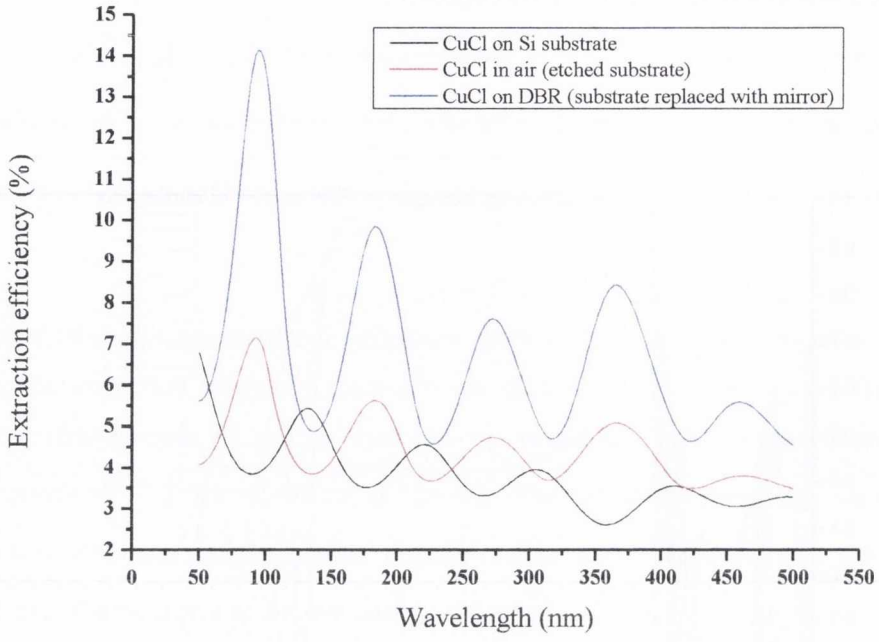

Figure 4.18: *Extraction efficiency of CuCl on Si, in air and with a TiO_2/SiO_2 DBR. The curve presenting CuCl on Si layer is not in phase with CuCl in air thus extraction efficiency values look much lower. In fact extraction efficiency is similar for both structures, but maxima occur for different thicknesses.*

As can be observed the extraction efficiency of the structure with the DBR in the place of the Si substrate has the highest extraction efficiency of all three structures discussed. As already stated, about 80% of radiation emitted towards the bottom CuCl interface was lost because of limited reflectivity of the bottom interface. Since both the CuCl/Air interface and the DBR do not change the phase of the wave, the maxima in extraction efficiency occur at the same positions for CuCl in air and CuCl on DBR. The increase in extraction efficiency is almost 50% for the DBR supported structure. In the growth and fabrication of structures for optimized emission the thickness has to be carefully adjusted to take account of the phase changes.

This air/CuCl/DBR structure is still a relatively weak cavity due to the low reflectivity at the CuCl interface. Given the bulk naure of this cavity it can be investigated whether placing another layer on the top to form a stronger cavity can provide any further improvements. The four different options considered are shown in *Figure 4.19*. Unprotected CuCl is unstable in the atmosphere due to omnipresent humidity. Thus, the potential CuCl device has to be protected in order to operate. The coating layer can have the protective function only or alternatively can also act as the top mirror and can influence the emission.

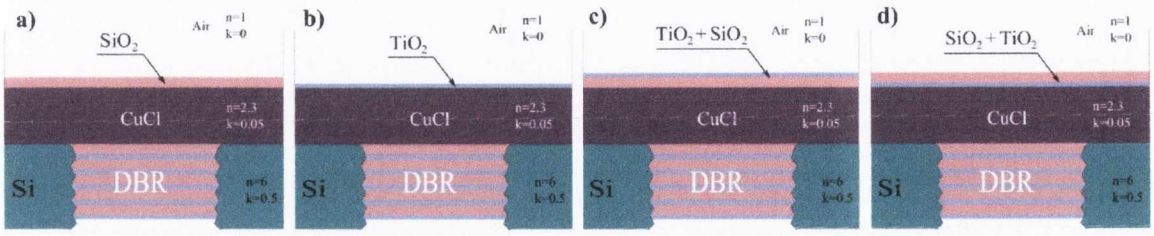

***Figure 4.19**: Four cavity structures with a range of top mirror option and a 5 pair SiO_2/ TiO_2 DBR on the bottom. The top layers utilise the same materials as bottom DBRs. They are investigated as potentially protective layers for CuCl.*

Figure 4.19a and *Figure 4.19b* show a single layer of SiO_2 and TiO_2, respectively. These cases can be considered as protective layers only. In *Figure 4.19c* there is one period of the previously discussed SiO_2/ TiO_2 DBR structure on top of the CuCl layer. The last of the considered structures has the pair of SiO_2 and TiO_2 in order inversed according to the DBR. The *Figure 4.20* shows the extraction efficiency achieved in four coated structures compared with that of *Figure 4.14c*. None of the coatings gave any improvement in terms of extraction efficiency enhancement in respect of uncoated CuCl layer. However, some of the coatings can be considered as potential protective layers. SiO_2/TiO_2 which is an inverse DBR pair does not modify the phase and has the same maximum extraction efficiency of 14% at 100 nm thick CuCl layer as uncoated sample. The extraction efficiency is limited by the CuCl/air interface refractive index contrast. Further improvement by the means of the cavity effect is impossible due to significant absorption of CuCl. Decrease of CuCl active region thickness would allow for possible improvement. The negative influence of coating is visible for thicker CuCl layers. The single layer of TiO_2 also guaranties high extraction efficiency however for phase shifted CuCl layer thicknesses. The choice of coating would be determined by the device design. If the design and fabrication capabilities would allow for CuCl thickness below 100 nm thus the SiO_2/TiO_2 coating is reasonable. However, for CuCl thickness of 375 the layer of SiO_2 allows for the highest extraction efficiency, comparable to that of uncoated CuCl.

For CuCl the refractive index value is lower than for other wide band gap materials (i.e. GaAs). Thus, as discussed previously, the overall improvements that can be achieved by overcoming total internal reflection losses are less noticeable in CuCl. In this work the impact the implementation of a cavity structure can have on the bulk emitting medium was investigated. The sensitivity of the extraction efficiency to the thickness of the CuCl layer is a consequence of the interference effects and critical to optimization of the extraction efficiency. The significant increase of extraction efficiency is achieved by the replacement of Si subtrate by a DBR. However, further improvements due to modification of the cavity are not seen.

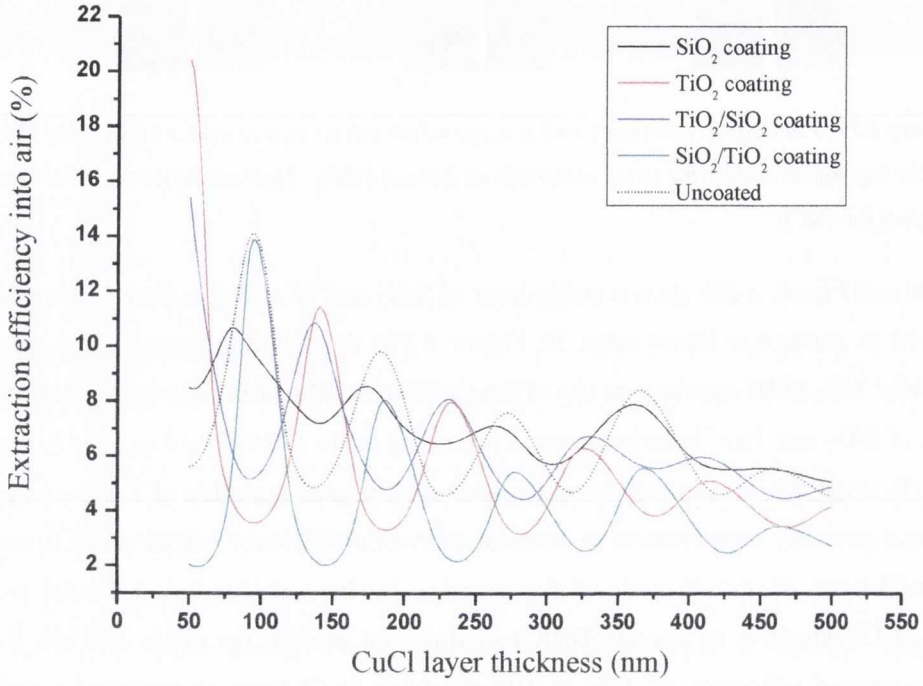

***Figure 4.20**: Extraction efficiency of CuCl on DBR. There are four different coating layers compared to an uncoated sample. The extraction efficiency cannot be optimised significantly by the means of coating. However, pairing a particular CuCl thickness with an appropriate coating can give efficient emitter additionally protected.*

Further the significance of absorption within the CuCl layer thickness will be investigated. It will be shown, that the absorption becomes the dominant loss factor in the high finesse cavity. In order to demonstrate the problem new DBR structure will be introduced. The smaller refractive index contrast between layers will allow for more gradual control over the DBR reflectivity. The reflectivity spectra in function of DBR pairs number for SiO_2/Al_2O_3 mirror are presented in

Figure 4.21. To see the impact of the absorption, firstly, the extraction efficiency of the CuCl microcavities with and without absorption is presented in *Figure 4.22*. We find that the increase of extraction efficiency due to modification of spatial pattern is possible only in the case of a non absorptive medium inside the cavity, i.e in QW structures, where thin layers of active medium are placed in the antinodes of the mode and separated by the transparent spacers.

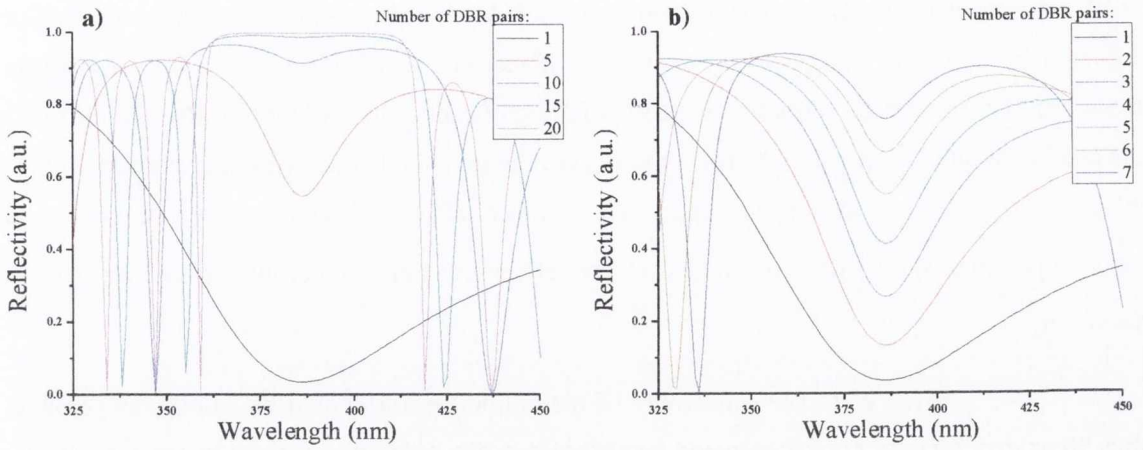

Figure 4.21: *Reflectivity of SiO_2/Al_2O_3 DBR as a function of the mirror pairs number. Du to relatively low refractive index contrast between SiO_2 and Al_2O_3 the reflectivity can be controlled gradually.*

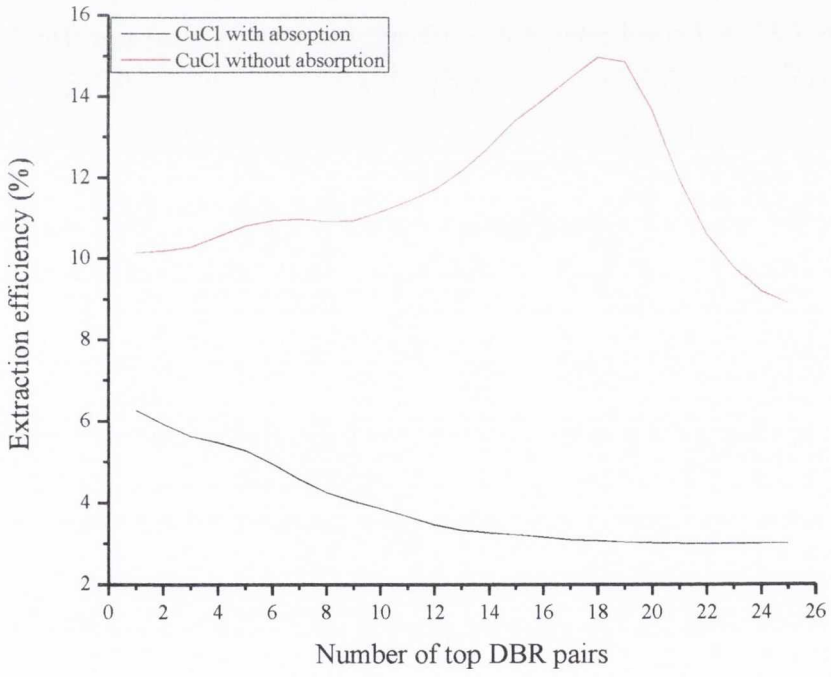

Figure 4.22*: Extraction efficiency into air from 190 nm thick (1 λ) bulk CuCl microcavity as a function of top DBR pairs number. The black curve shows the results obtained for the real CuCl absorption. The red curve is calculated for CuCl without absorption (k=0).*

In the case of the bulk structures, the absorption of the thick active region plays a significant role. The spatial pattern is modified in both cases, however the benefit of this modification is suppressed by absorption in the bulk cavity. In order to illustrate these points, the

DBR constituent materials are changed to SiO_2 and Al_2O_3 which will allow for more gradual variation in the mirror reflectivity as a function of the number of mirror pairs. As was already discussed, TiO_2 and SiO_2 refractive indices differ significantly thus a highly reflective mirror is obtained with only a few pairs. As few as two pairs can give a reflectivity of approximately 80%-90%, which makes a study of the impact of the mirror reflectivity with small variations over a range impossible. With $\frac{\lambda}{4}$ pairs of SiO_2/Al_2O_3 the reflectivity can be controlled in smaller steps as shown in

Figure 4.21. The reflectivity of the bottom mirror should be as high as possible, thus 20 pairs of SiO_2/Al_2O_3 was assumed for simulation. The top mirror reflectivity is controlled by the number of SiO_2/Al_2O_3 and this number is marked with colors as shown in the legend of

Figure 4.21. As can be seen in

Figure 4.21b, due to low contrast of refractive indices SiO_2/Al_2O_3 allows for smaller changes in reflectivity with increasing number of mirror pairs compared to the SiO_2/TiO_2 mirror.

In *Figure 4.23* the farfield patterns for different structures are compared. The *Figure 4.23a* shows the polar plot of the radiation emitted from the low finesse cavity, while *Figure 4.23b* shows similar plot but for the high finesse cavity.

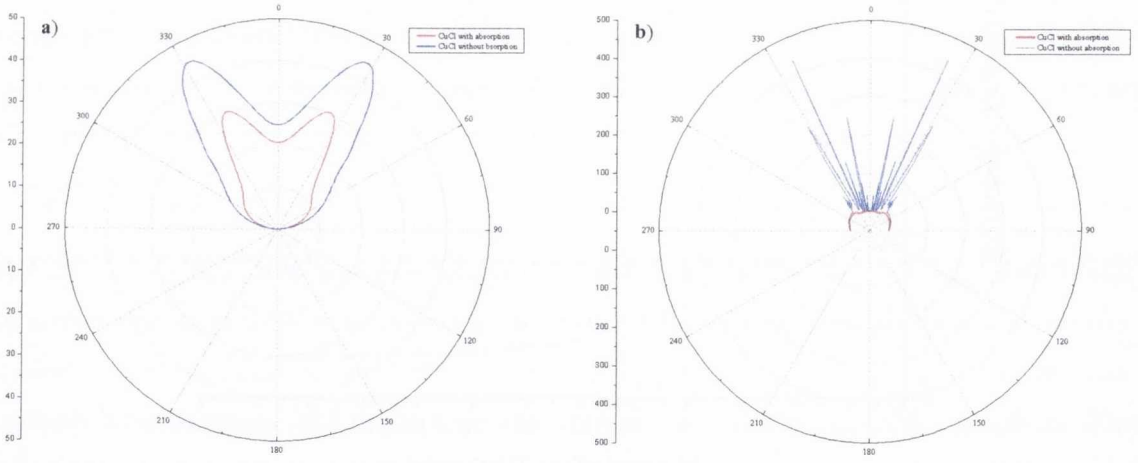

***Figure 4.23**: Farfield patterns of low (a) and high (b) finesse for a 1λ CuCl microcavity. The emission from the whole CuCl volume is taken into account. Due to CuCl absorption the bulk CuCl microcavity cannot benefit from the emission profile modifications.*

In both cases the bottom mirror is a DBR built of 20 pairs SiO_2/Al_2O_3 stack. The active region is a 190 nm thick CuCl layer which corresponds to 1λ length of the cavity. The top mirror is also the SiO_2/Al_2O_3 stack, one pair of reflectivity below 5% for low finesse cavity and 18 pairs with the reflectivity >90% for high finesse cavity. All the curves in *Figure 4.23* represent the sum of farfields calculated for twenty equidistant emitters along the CuCl layer thickness. As can be seen

in *Figure 4.23a*, in the low finesse cavity the spatial profile is not significantly affected by the absorption of CuCl. The overall radiation intensity is suppressed approximately equally in all directions. In the case of the high finesse cavity, *Figure 4.23b*, the emission profile of the cavity with non-absorbing medium has a strong angular dependence with very sharp peaks at selected angles. The emission spatial profile of high finesse cavity with absorbing medium is almost flat, with little spatial variation of the farfield pattern.

4.6 Conclusions

The efficiency of extracting emitted photons from a semiconductor is significantly affected by the contrast of refractive indices of the emitting material and surrounding medium. The extraction efficiency for the vacuum case emitter is typically of only a few percent. One of the possible methods to overcome this drawback is by placing the emitter inside an optical microcavity which results in modification of the spatial emission pattern and makes it possible to redirect radiation into the extraction cone. In this chapter we have investigated the route to optimizing the extraction efficiency for a bulk CuCl structure with a view to bulk CuCL light emitting devices. A model to consider emission from a bulk emitting layer has been implemented. The extraction efficiency is shown to depend on the structure parameters, such as refractive index, absorption and thickness of the constituent layers. The largest increase in extraction efficiency is achieved when the bottom of the structure is a highly reflective mirror. Moreover, the extraction efficiency depends on the semiconductor layer thickness. This dependence is periodic, with the periodicity of $\frac{\lambda}{2}$ where λ is the emission wavelength in the cavity. The maxima of extraction efficiency occur for the CuCl thicknesses being the even multiplicities of $\frac{\lambda}{2}$. The predicted extraction efficiency for bulk CuCl on a 7 pair SiO_2/TiO_2 DBR mirror structure is of the order of 14% for a thickness of 95 nm, slightly more than two times higher than what can be achieved for the same thickness of as-grown CuCl layer on Si. Stronger cavities do not lead to further increases in the extraction efficiency due to the effects of absorption thoughout the bulk CuCl layer. Therefore the top cladding layer while not improving the extraction efficiency is required to seal the CuCl material and provide stability for potential device performance, a SiO_2/TiO_2 and monolayer of TiO_2 are found to be good options.

4.7 References

[1] P. Royo, R. P. Stanley, and M. Ilegems, "Analytical calculation of the extraction efficiency of microcavity light-emitting diodes for display and fiber coupling applications," *IEEE JOURNAL ON SELECTED TOPICS IN QUANTUM ELECTRONICS*, vol. 8, no. 2, p. 207, 2002.

[2] D. G. Deppe, C. Lei, C. C. Lin, and D. L. Huffaker, "Spontaneous Emission from Planar Microstructures," *Journal of Modern Optics*, vol. 41, no. 2, pp. 325-344, 1994.

[3] H. Ryu, "Modification of the Light Extraction Efficiency in Micro-cavity Vertical InGaN Light-emitting Diode Structures," *Journal of the Korean Physical Society*, vol. 55, no. 3, pp. 1267-1271, 2009.

[4] A. Shaw, T. McCormack, A. L. Bradley, J. G. Lunney, and J. F. Donegan, "Modelling of Extraction Efficiency of GaN-Based Resonant Cavity Light Emitting Diodes Emitting at 510 nm," *physica status solidi (a)*, vol. 192, no. 1, pp. 103–109, 2002.

[5] D. Delbeke, R. Bockstaele, P. Bienstman, R. Baets, and H. Benisty, "High-efficiency semiconductor resonant-cavity light-emittingdiodes: a review," *IEEE Journal of Selected Topics in Quantum Electronics*, vol. 8, no. 2, pp. 189–206, 2002.

[6] M. Rattier et al., "High extraction efficiency, laterally injected, light emitting diodes combining microcavities and photonic crystals," *Optical and Quantum Electronics*, vol. 34, no. 1, pp. 79–89, 2002.

[7] T. Fujii, Y. Gao, R. Sharma, E. L. Hu, S. P. DenBaars, and S. Nakamura, "Increase in the extraction efficiency of GaN-based light-emitting diodes via surface roughening," *Applied Physics Letters*, vol. 84, no. 6, p. 855, 2004.

[8] Y. Lee et al., "Increasing the extraction efficiency of AlGaInP LEDs via n-side surface roughening," *IEEE Photonics Technology Letters*, vol. 17, no. 11, pp. 2289-2291, 2005.

[9] H. W. Jang, S. W. Ryu, H. K. Yu, S. Lee, and J. L. Lee, "The role of reflective p-contacts in the enhancement of light extraction in nanotextured vertical InGaN light-emitting diodes," *Nanotechnology*, vol. 21, p. 025203, 2010.

[10] H. Benisty, H. De Neve, and C. Weisbuch, "Impact of planar microcavity effects on light extraction—Part I: Basic concepts and analytical trends," *IEEE Journal of Quantum Electronics*, vol. 34, no. 9, 1998.

[11] H. De Neve, J. Blondelle, R. Baets, P. Demeester, P. Van Daele, and G. Borghs, "High Efficiency Planar Microcavity LED's: Comparison of Design and Experiment," *IEEE Photonics Technology Letters*, vol. 7, no. 3, pp. 287-289, 1995.

[12] D. Ochoa, R. Houdré, M. Ilegems, C. Hanke, and B. Borchert, "Microcavity light emitting diodes as efficient planar light emitters for telecommunication applications," *C. R. Physique*, vol. 3, pp. 3-14, 2002.

[13] E. Matioli and C. Weisbuch, "Impact of photonic crystals on LED light extraction efficiency: approaches and limits to vertical structure designs," *Journal of Physics D: Applied Physics*, vol. 43, p. 354005, 2010.

[14] E. Matioli et al., "High extraction efficiency light-emitting diodes based on embedded air-gap photonic-crystals," *Applied Physics Letters*, vol. 96, no. 3, p. 031108, 2010.

[15] Y. Yamamoto, F. Tassone, and H. Cao, *Semiconductor cavity quantum electrodynamics*. Springer.

[16] F. L. Pedrotti, L. M. Pedrotti, and L. S. Pedrotti, *Introduction to optics*, 3rd ed., 1 vols. New Jersey: Pearson, 2007.

[17] H. Benisty, R. Stanley, and M. Mayer, "Method of source terms for dipole emission modification in modes of arbitrary planar structures," *J. Opt. Soc. Am. A*, vol. 15, no. 5, pp. 1192-1201, 1988.

[18] H. Benisty, H. De Neve, and C. Weisbuch, "Impact of planar microcavity effects on light extraction-Part II: selected exact simulations and role of photon recycling," *IEEE Journal of Quantum Electronics*, vol. 34, no. 9, pp. 1632–1643, 1998.

5 Cavity polaritons in CuCl based microcavities

5.1 Background

As was presented in chapter 2, copper (I) chloride is a very promising material that can be considered as a potential competitor with already commercialised wide band-gap semiconductors such as GaN or ZnO. One area of intense interest in recent years is the development of cavity polariton light emitting devices based on strong light-matter interaction in solids. One of the simplest results of light-matter interactions is the creation of an exciton. The electron-hole pair created by the photon in the solid can interact via the Coulomb attraction. The bound state of the electron and hole is a quasiparticle known as an exciton [1]. If such an excitonic medium is placed inside the optical microcavity, the exciton can further interact with the electromagnetic field creating a more complex quasiparticle or a new quantum state called a polariton. A polariton is sometimes called half-light, half-matter state, because it possesses features of both. On one hand it contains matter in the form of electrons. On the other hand it has a very low effective mass and importantly, unlike electrons polaritons tend to behave like bosons. The bosonic nature it exhibits allows for new effects that are unachievable with electronic devices. For instance polariton lasers can operate without the population inversion requirement [2], [3]. In this way these lasers can have thresholds of up to two orders of magnitude lower than conventional semiconductor lasers [4]. Also the phenomena of coherent polariton condensation can be used in polariton driven optical amplifiers [5], [6]. Polaritons as bosons can constitute the collective state of a Bose-Einstein Condensate (BEC) [7-9] which is also expected to play a significant role in new generation low threshold coherent light sources. A BEC of polaritons in a semiconductor microcavity is also suggested as a possible mediator for electrons possibly enabling high temperature superconductivity [10].

The pioneering works addressing the cavity polaritons were presented in the early nineties by Weisbuch *et al* [11]. The authors demonstrated that an absorbing semiconductor placed inside a high finesse cavity can periodically absorb and emit the cavity photon. In the beginning cavity polaritons were observed only at low temperatures in quantum well (QW) microcavities [12], [13]. Initially as an active medium the mature semiconductor material of GaAs was used. A quantisation of the active layer was necessary in this case because of the very weak exciton binding energy in GaAs of 3.6 meV in bulk [14], which still remains below 20 meV in QWs [15]. Further progress in material fabrication and the introduction of materials with higher exciton binding energies helped to overcome many limitations of the initial cavity structures. With the introduction of wide band-gap semiconductors such as ZnO and GaN the observation of cavity polaritons at higher

temperatures [16], [17] and in bulk microcavities at low temperatures [18], [19] became possible . Multi QW structures and sophisticated material growth techniques allowed for the fabrication of GaAs based polariton LED working at room temperature [20].

One of the most important factors making CuCl superior to other semiconductors in terms of light-matter interaction is its very high exciton binding energy of 190 meV [21]. Another property of CuCl attributed to excitons is the oscillator strength value of the order of $10^{14}/cm^2$. For the absorbing medium the oscillator strength is the quantity expressing the strength of the transition between the ground and excited quantum states. This value is approximately one order of magnitude higher than that observed in ZnO or GaN and two orders of magnitude higher than in GaAs. The oscillator strength indicates the probability of transition from the ground state to the excited state in medium. The higher the oscillator strength value the lower cavity finesse is needed to observe strong coupling in the structure. In this work evidence for strong coupling between the exciton and cavity photon in bulk CuCl microcavity at room temperature will be presented. Cavity polariton dispersion has previously been reported for bulk CuCl microcavities only at 10K [22], [23].

5.2 The light-matter interaction.

A structure containing a semiconductor layer placed between two mirrors constitutes a semiconductor microcavity. The excitation of the active medium can be considered as an oscillator. Also the optical cavity bound by two separated mirrors can also be treated as a damped oscillator. The damping rate depends on the cavity finesse which depends on the reflectivity of the mirrors. Therefore, the semiconductor cavity system can be regarded as a coupled oscillators system. A full quantum mechanical explanation of light-matter interaction phenomena can be applied [24]. The basic properties of the semiconductor microcavity system will be discussed below.

5.2.1 The weak coupling regime

The interaction between the cavity and the intra-cavity semiconductor material takes place when the resonance of the cavity and the absorption line of the medium are comparable. In this situation two cases are possible. Firstly, the photon and the semiconductor may be in the ground state (not excited). Alternatively, the photon may be absorbed by the semiconductor and so its energy is contained within the excitation state of semiconductor. The influence of the microcavity can be treated as perturbation for the exciton. The Hamiltonian of the whole system can be written as:

$$H = H_{el} + H_{ph} + H_{per} \qquad (5.1)$$

where, H_{el} is the electronic (or excitonic) term of the Hamiltonian, H_{ph} is the photonic term and H_{per} is the perturbative term of Hamiltonian. In the weak regime of light matter interaction the spontaneous emission rate ω_{if} can be controlled. Its relation to the density of final state $D(E)$ describes Fermi's golden rule:

$$\omega_{if} = \frac{2\pi}{h}|H_{if}|^2 D(E) \tag{5.2}$$

$$H_{if} = \int \Psi_f(r)\, H \Psi_i(r) d\tau \tag{5.3}$$

where H_{if} is the transition matrix element or in Dirac's notation:

$$H_{if} = \langle f|H|i\rangle \tag{5.4}$$

where $|i\rangle$ is the initial state and $\langle f|$ is the final state.

Also the spontaneous emission spatial pattern can be modified by manipulating the optical cavity properties. In this case the cavity acts as a filter. The maximum emission intensity occurs when the medium emission wavelength and the cavity resonance are slightly detuned, as was discussed in more detail in chapter 4.

5.2.2 The strong coupling regime

When the cavity finesse is high enough to allow the photon to be reabsorbed and reemitted many times before it decays the cavity cannot be treated as perturbation anymore. In this case rather than two separate states, a new quantum state is created. The oscillating quasiparticle of the cavity photon and semiconductor exciton is called the cavity polariton. It possesses the properties of both its constituents and so is described as half-light, half-matter. More precisely the effective mass of the cavity polariton is two orders of magnitude lower than the effective mass of the electron or hole.

5.2.3 The model

As discussed in Chapter 4, the propagation of the electromagnetic field within multilayered structures can be modelled for layers of known refractive indices and thicknesses. In this model the dielectric constant $\varepsilon(\omega)$of the active medium is expressed by the function:

$$\varepsilon(\omega) = \varepsilon_b + \frac{f_{osc} q^2}{m\varepsilon_0 \omega_0^2 - \omega^2 - i\gamma_{at}\omega} \tag{5.5}$$

where ε_b is the background dielectric constant, q and m are the electron charge and mass, ω_0 is the resonance frequency of an oscillator, ω is the central frequency of the Lorentzian, γ_{at} is FWHM of the resonance line and f_{osc} is the oscillator strength.

The absorption coefficient is given by:

$$\alpha(\omega) = \frac{\gamma_{at}}{4(\omega - \omega_0)^2 + \gamma_{at}^2} \tag{5.6}$$

and the real part of the refractive index:

$$n(\omega) = n_\infty - \alpha_0 \frac{C(\omega - \omega_0)}{2\pi\omega 4(\omega - \omega_0)^2 + \gamma_{at}^2} \tag{5.7}$$

where $\alpha_0 = \frac{\pi e^2 f_{osc}}{2\varepsilon_0 mc\gamma_{at}L}$ is an absorption coefficient for n_∞=1, c is the speed of light and L is the cavity length.

Using multi-beam analysis, reflection *(R)*, transmission *(T)* and absorption *(A)* of the whole structure can be calculated.

$$R(\omega) = \frac{(1 - e^{-\alpha L})^2 R + 4Re^{-\alpha L} sin^2\left(\frac{\phi}{2}\right)}{(1 - Re^{-\alpha L})^2 R + 4Re^{-\alpha L} sin^2\left(\frac{\phi}{2}\right)} \tag{5.8}$$

$$\phi = \frac{2\pi(\omega - \omega_0)}{FSR} + \frac{4\pi(n(\omega_0) - 1)L_c\omega}{c} \tag{5.9}$$

Where ϕ is the phase shift experienced by the field upon completion of the round-trip through the cavity, αL_c is single pass absorption and $FSR = \frac{c}{2L_c}$ is free spectral range of the empty cavity with length L_c.

For $\omega = \omega_0$ and if the oscillator strength is high enough the effect of strong coupling can be observed as line splitting in *(T)*, *(R)* and *(A)*. The value of the splitting energy can be calculated with the following formula:

$$\Omega = \sqrt{\frac{F\alpha_0 L\gamma_{ex}\gamma_{ph}}{\pi} - \frac{(\gamma_{ex}\gamma_{ph})^2}{2}} \qquad (5.10)$$

Where F is cavity finesse, L is cavity length, γ_{ex}, γ_{ph} represent the damping of excitonic and photonic oscillators.

The Rabi splitting can be controlled by the cavity size and finesse which in practice is achieved by tuning the thickness of optically active material(s) and the reflectivity of cavity mirrors.

5.3 Investigation of a bulk CuCl microcavity

The bulk microcavity with CuCl as an active medium can be studied in order to observe the evidence of strong coupling. The bulk CuCl intra-cavity layer is deposited by vacuum evaporation on a pre-grown distributed Bragg reflector (DBR) and topped with a metallic mirror. The materials used to form the DBR component have to be transparent in the wavelength range of interest and provide sufficient refractive index contrast. From the available materials magnesium fluoride and titania were chosen because of relatively low absorption on the high energy side of the CuCl exciton line. Gold was used to form the top mirror, as will be discussed below.

The mirrors

The reflectivity of the MgF_2/TiO_2 DBRs was calculated using the transfer matrix model described in chapter 4 and the spectra as a function of the number of mirror pairs are shown in *Figure 5.1*. The refractive index values of MgF_2 and TiO_2 were obtained from the SOPRA webpage [25]. The thicknesses of MgF_2 and TiO_2 layers were determined to be 65 nm and 23 nm, respectively. These values correspond to a quarter of central wavelength, which was chosen to be 370 nm (3.35 eV) in vacuum for the mirror.

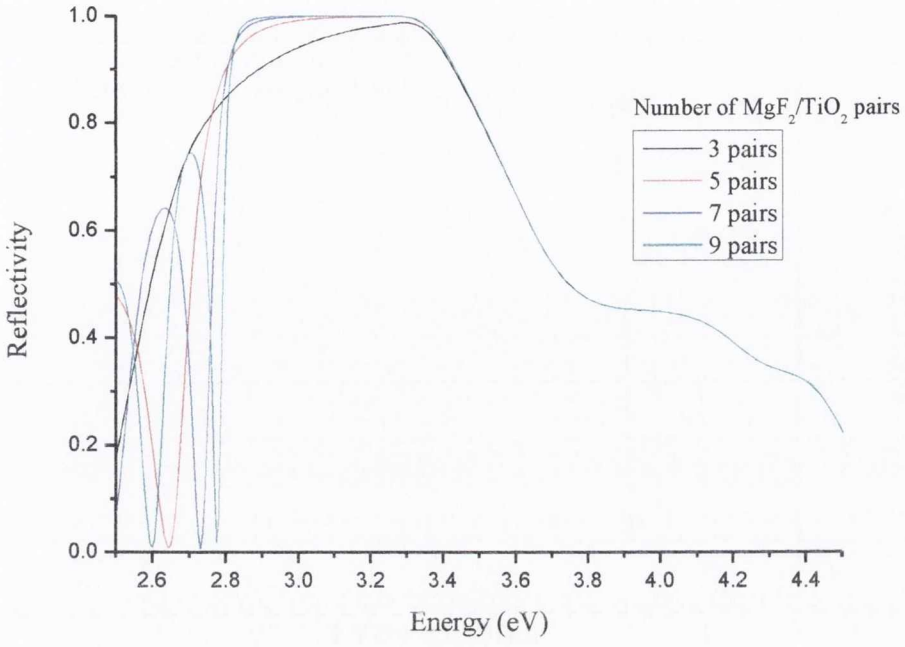

Figure 5.1: *Reflectivity of the DBR structure as a function of number of MgF_2/TiO_2 pairs.*

As the number of MgF_2/TiO_2 pairs is increased the stop-band of the mirror becomes narrower and reflectivity increases. As can be seen in *Figure 5.1* reflectivity close to 100% can be achieved in the range of 2.83 eV to 3.4 eV approximately. Such a high reflectivity is achieved with only few mirror pairs of DBR structure due to relatively high refractive contrast between MgF_2/TiO_2. As can be seen in *Figure 5.1* there is no significant difference in reflectivity between 7 and 9 pairs, however the difference between 5 and 7 pairs is noticeable. Thus, the optimal DBR consists of 7 MgF_2/TiO_2 pairs. More complex stacks do not give any significant improvement in terms of mirror reflectivity. The DBR structure consisting of seven pairs of quarter lambda thick MgF_2 and TiO_2 was grown by a commercial supplier. In *Figure 5.2* the expected reflectivity of the structure is compared with both the experimental reflectivity measured by the commercial mirror supplier and that measured using our own experimental setup described in *paragraph 5.5.2*. All spectra are consistent and give good agreement in the spectral range of interest from 350 nm to 450 nm (3.542 eV to 2.755 eV). It should be noted, that a wider stop-band would be more desirable for a study as function of detuning, but absorption in the UV of available materials made it impossible to shift the stop-band to higher energies. The stopband however does cover the most important range corresponding to exciton energy of CuCl.

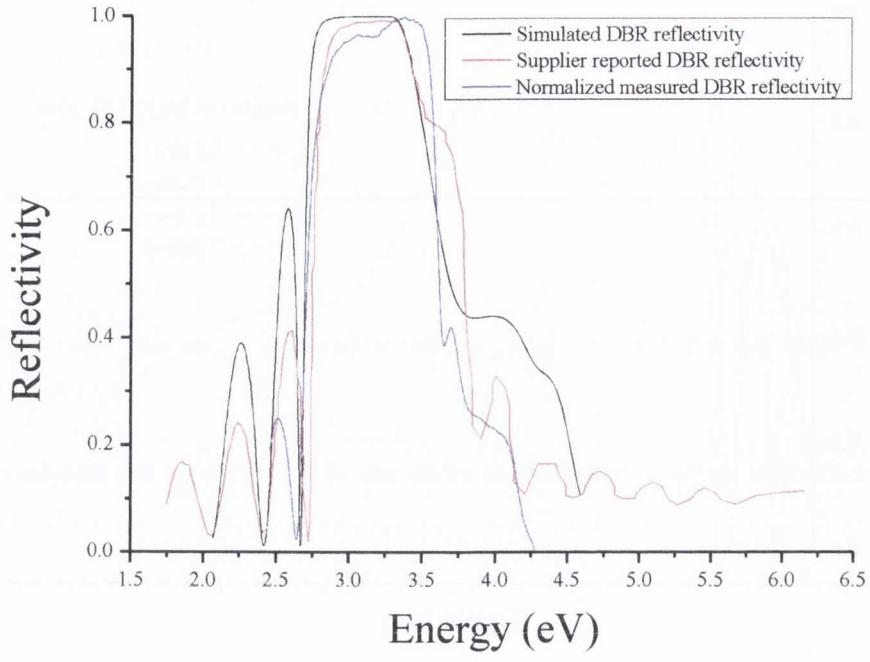

Figure 5.2: *The reflectivity of the DBR (7 pairs). The solid (black) line shows the simulated curve calculated with MATLAB using TMM. The dotted red curve shows the reflectivity of the mirror reported by the supplier. The dashed blue line shows the normalized measurement done on the mirror.*

The bottom mirror has reflectivity above 80% for wavelengths ranging from 347 nm – 446 nm. A lower reflectivity top mirror is required to allow the incidence light to penetrate the cavity. A top DBR mirror would provide more precise tuning of the top mirror reflectivity but this mirror would have to be deposited externally, and in the intervening period the CuCl layer properties would be compromised due the relatively high hygroscopicity of CuCl. The alternative is the deposition of a metal mirror. Additionally CuCl is a rather reactive compound and therefore aluminium which has very high reflectivity over the wide range of wavelengths of interest could not be used. Noble metals are non reactive. Gold was chosen as it could provide adequate reflectivity and its relatively low melting temperature was helpful in terms of thickness and precise growth rate control. A top mirror reflectivity of approximately around 37% at 371nm is obtained for a gold layer thickness of 45nm. The cavity formed using the top gold mirror and the bottom DBR mirror results in a cavity finesse not less than 58 in the wavelengths range 347 nm - 446 nm. The relatively low finesse is not a limiting factor as it is compensated by the very high value of excitonic oscillator strength in CuCl. Even cavities exhibiting finesse value below 50 were proven to be sufficient to demonstrate strong coupling in ZnO based microcavities [18]. The oscillator strength of CuCl, of the order of $10^{14}/cm^2$, is one order of magnitude higher than in ZnO[26]. Hence it is reasonable to expect evidence of strong coupling in such structures.

5.4 The bulk CuCl microcavity

The microcavity used in these experiments is a planar Fabry-Pérot resonator. The bottom mirror is a highly reflective DBR made of 7 pairs of quarter lambda MgF_2 and TiO_2 layers. The top mirror a thin gold layer, vacuum deposited *in situ* with CuCl. The active medium is the vapour deposited layer of CuCl. The thickness of CuCl varies from 90 nm to 140 nm, approximately. During the vacuum deposition the growth rate is controlled using a crystal oscillator. Further, the thicknesses of grown samples were verified with both DekTak profilometer and ellipsometry in order to determine optimal growth conditions. Based on the numerical simulations, for a refractive index value of 2.2 and the exciton wavelength of 379 nm the $\frac{\lambda}{2}$ cavity corresponds to a CuCl layer thickness of 107 nm. Detuning of the cavity resonance and exciton resonance is achieved by varying the cavity parameters. Variation of the CuCl thickness between 90 nm and 140 nm covers the wide range of resonance frequencies including CuCl exciton resonance. Other methods for investigating the exciton-photon detuning include angle tuning and temperature tuning. As uniform layer thicknesses cannot be easily achieved by the vacuum deposition technique. The thickness uniformly changes across the vacuum deposited, providing conditions for investigation of the cavity-exciton detuning with increasing cavity length across the sample. With angle detuning it can be difficult to ensure that there is no movement of the incident light spot on the sample, and therefore for the measurements presented to investigate strong coupling in a the CuCl microcavity structure position detuning was the preferred method.

5.4.1 Tuning the cavity resonance

The simulation of the reflectivity of the non-absorbing cavity is presented in *Figure 5.3* to investigate the position of the photon resonance as a function of the cavity length.

The cavity in this case is comprised of two mirrors filled with a non-absorbing material with refractive index of 2.2 (CuCl at 370 nm) and the value of the oscillator strength set to 0. The bottom mirror is the Bragg stack of seven pairs of MgF_2/TiO_2 layers described in section 5.3. The top mirror is a layer of 30 nm of gold.

As the cavity length increases the cavity resonance moves to longer wavelengths. There are four dips corresponding to different cavity lengths 98, 107, 116 and 125 nm respectively. The photon energy of the same empty cavity plotted as a function of cavity thickness is shown in *Figure 5.4*.

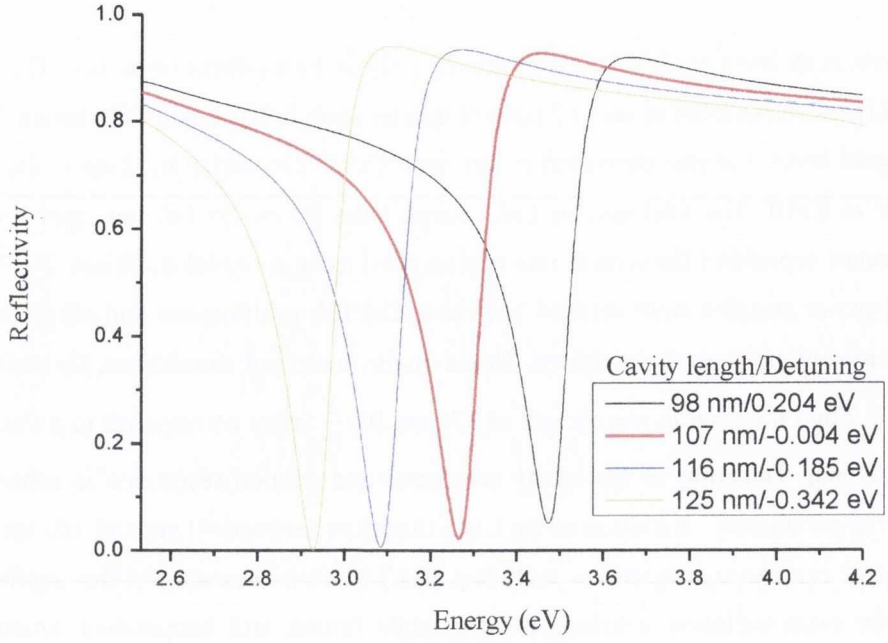

Figure 5.3: *Reflectivity spectra of an empty cavity. Cavity length oscillates around* $\frac{\lambda}{2}$ *which was found to be 107 nm for CuCl microcavity.*

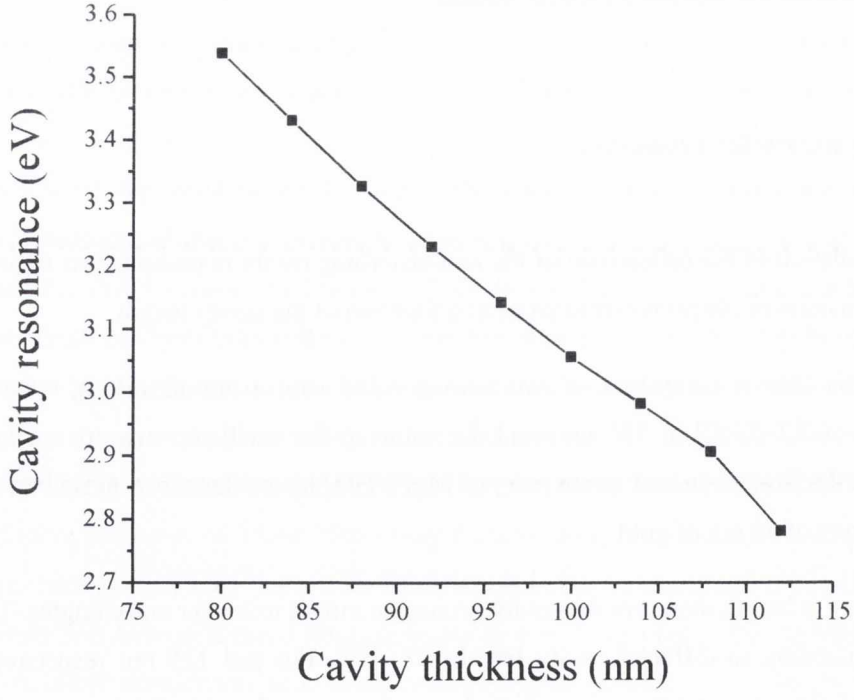

Figure 5.4: *The cavity resonance as a function of cavity thickness.*

The resonance frequency is given by the following condition:

$$f = \frac{Nc}{2d} \qquad N = \{1,2,3 \ldots\} \tag{5.11}$$

Where 2d is round trip distance and c is the speed of light in the medium.

Hence, the resonant wavelength λ is defined as:

$$\lambda = \frac{2d}{N} \tag{5.12}$$

5.4.2 The semiconductor cavity - theory

The $Z_{1,2}$ exciton has peak absorption at 379 nm (3.27 eV). As such, a cavity of 107 nm length has resonance at the same energy as the $Z_{1,2}$ exciton. Cavities of length below 107 nm are positively detuned in terms of energy thus their resonance will be at higher energies than the energy of the CuCl exciton of 3.27 eV. An example is the black curve in *Figure 5.3* representing the reflectivity of a 98 nm long cavity. The opposite is true for cavity length exceeding 107 nm, with resonance at energies below 3.27 eV. Such cavities are negatively detuned with respect to the $Z_{1,2}$ energy. In *Figure 5.3* reflectivity spectra of these cavities are shown with blue and yellow curves.

The cavities discussed above are empty. The space between the mirrors is empty or alternatively filled with a medium having negligible absorption at cavity resonance. Much more interesting phenomena can be observed for the opposite situation. If the intracavity medium has significant absorption at cavity resonance the light and matter start to interact. In the case of a semiconductor material such light-matter interactions are well defined. The interaction type can be twofold, weak or strong. Thus together with an empty cavity there are three scenarios possible. In *Figure 5.5* there are three simulated spectra presented.

The reflectivity spectra are for the same cavity, filled with three different active media. In the first case, the material has a refractive index corresponding to that of CuCl but is not absorbing, that is, it has an oscillator strength value of zero. The dotted curve shows only the dip in reflectivity resulting from the cavity resonance. The red dashed curve shows the spectrum calculated for a cavity filled with a similar medium but having some absorption, at a value lower than the absorption in CuCl. The value of the oscillator strength in simulation was set to $5.6 \times 10^{13}/cm^2$. The broadening of the absorption dip is a result of the interaction between the cavity photon state and

the active medium exciton state. In this case the interaction strength remains within the weak coupling regime.

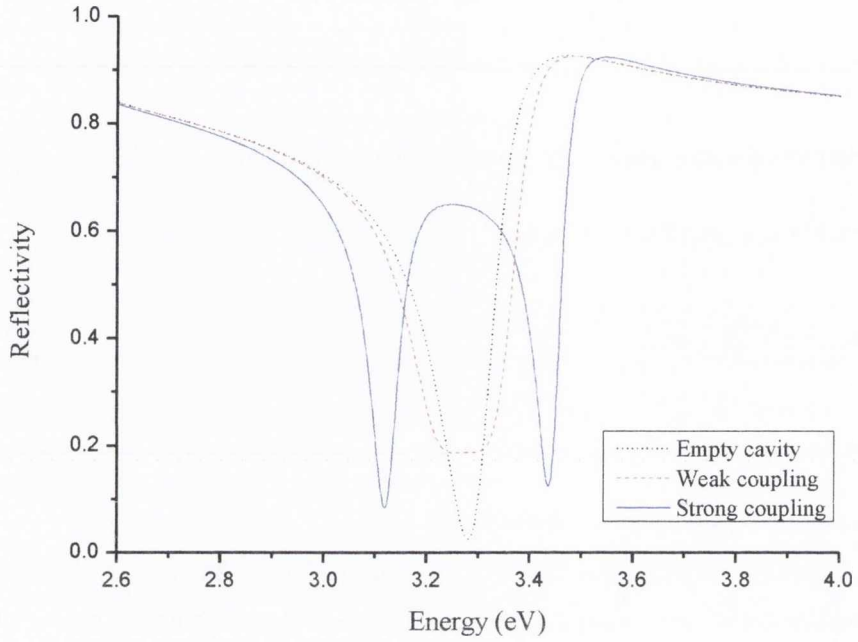

Figure 5.5: *Reflectivity of empty cavity and cavity filled with weakly and strongly interacting media. The cavity length is of 107 nm, which corresponds to* $\frac{\lambda}{2}$ *value.*

With increased values of oscillator strength the new quantum state becomes visible. The influence of the active medium cannot be treated as perturbation for cavity photon anymore. The splitting of the reflectivity line is evidence of the oscillating energy transfer between the cavity photon and the semiconductor exciton. The two dips in the solid blue curve correspond to upper and lower polariton bands. These bands are separated by the energy corresponding to Rabi splitting Ω. The Rabi splitting can be determined from the anticrossing plots of polariton bands versus detuning energy. The Rabi splitting is visible as a difference in energy between lower polariton band (LPB) and upper polariton band (UPB). Comparison of two cases of near $\frac{\lambda}{2}$ CuCl microcavities is presented in *Figure 5.6*. *Figure 5.6a* shows the two polariton bands obtained from reflectivity simulation at an angle of incidence of 0°. The cavity length varies from 98 nm to 132 nm. The cavity length of 107 nm corresponds to the resonant energy of the CuCl medium, thus the cavity resonance is tuned to the exciton. In *Figure 5.6b* the cavity length is fixed to 115nm. The detuning is done by changing the angle of incidence between 0° and 60°. For the angle of approximately 36° the cavity resonance and exciton energy are equal. From the plot in *Figure 5.6a* the Rabi energy is determined as 315 meV from the angle dependant simulation in *Figure 5.6b* the Rabi energy is of 330 meV.

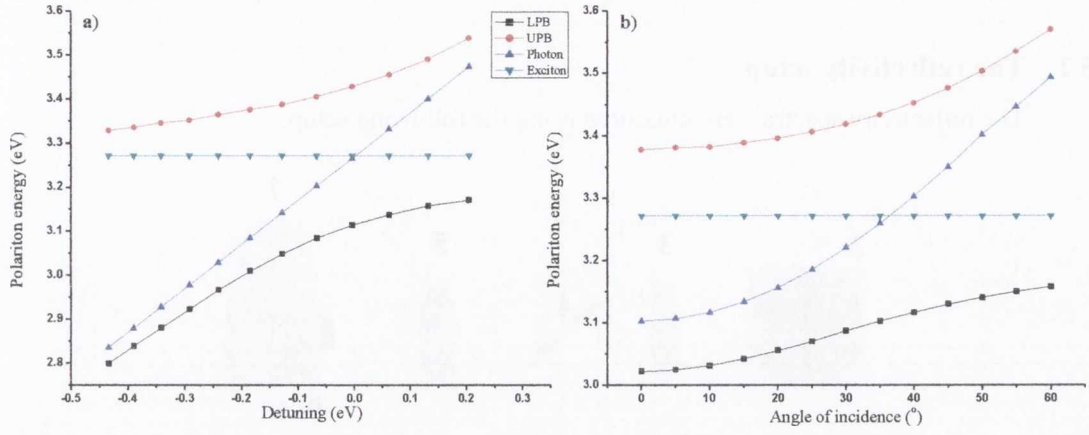

Figure 5.6: *Anti-crossing polariton bands in a CuCl microcavity where detuning was obtained by:* ***a)*** *changing the cavity length from 98 nm to 132 nm,* ***b)*** *changing the angle of incidence for constant cavity length of 115 nm.*

5.5 The experiment

5.5.1 The sample

The sample used in the experiment is the following three layer structure:

1) Top mirror – gold.
2) Active layer – CuCl.
3) Bottom mirror – DBR.

The samples used in the experiments were prepared by a vacuum deposition process at room temperature using an Edwards E-360 evaporator. The pressure in the chamber was lowered to the order of 10^{-6} mbar prior to evaporation. Commercially obtained mirrors described in section 5.3 were used as substrates. A layer of CuCl was evaporated *in situ* with the top mirror gold layer. The growth rate of both CuCl and gold was controlled in realtime with the help of the crystal oscillator. The rate was of approximately 0.3 nm/s for CuCl and similar for gold. The thickness of the CuCl layer varied gradually along the length of the sample from 98 nm to 132 nm. The wedge like structure was achieved by means of variable exposition of the substrate to the CuCl vapours. The thickness of 107 nm corresponds to a $\frac{\lambda}{2}$ cavity. The boundary thicknesses of CuCl layers were chosen in accordance to the stop-band of the bottom mirror. For the thickness values out of 98 nm – 132 nm range, the cavity resonance would be out of the mirror stop-band, thus no cavity effect could be observed for such thicknesses. A 30 nm thick layer of gold was used as the

top mirror. Due to CuCl instability the cavity was protected from atmospheric influence in a vacuum containers and a cryostat chamber all the time after the evaporation.

5.5.2 The reflectivity setup

The reflectivity spectra were measured using the following setup:

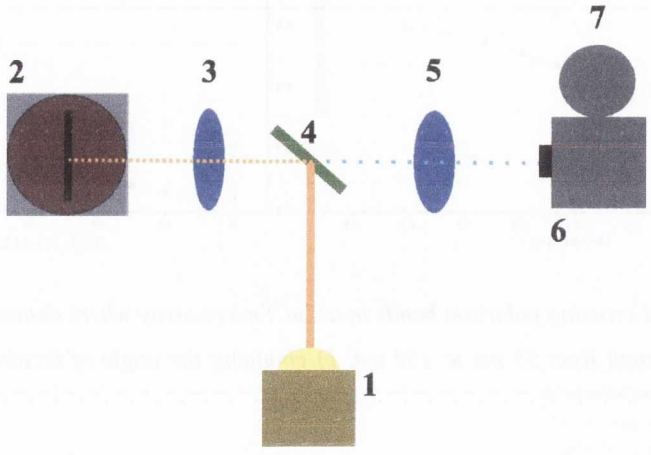

Figure 5.7: *The reflectivity measurement setup. The white light beam from the xenon lamp (1) is split by the beam splitter (4). The sample is placed within the cryostat (2). The lenses (3) and (5) help to focus the light. The final spectrum is measured using a spectrometer (6) and liquid nitrogen cooled CCD (7).*

A Hamamatsu xenon lamp was used as a white light source, which was directed to the beam splitter. The reflected fraction of the light was focused onto the sample. The sample was held in the liquid helium cryostat. Use of the cryostat facilitated reflectivity measurements over a wide range of temperatures (10K-296K) and helped to preserve the sample, which is destroyed at atmospheric conditions. The beam reflected at normal incidence from the sample was again split by the beam splitter. The transmitted fraction was focused by a lens, onto a detector, a liquid nitrogen cooled CCD coupled to the Triax 190 spectrometer, of 0.3 nm spectral resolution. The recorded spectra corresponding to three different detunings are presented in Figure 5.7.

5.5.3 The results

The reflectivity spectra taken at room temperature for the $\frac{\lambda}{2}$ cavity are compared with the modelled spectra. For all measured values of detuning both upper and lower polariton bands are visible. This is the result of very high values of oscillator strength in CuCl and thus very high value of Rabi splitting reaching 275 meV. The simulation using the value of oscillator strength reported in literature gave an even higher value of Rabi splitting of 400 meV. Such strong splitting was not observed in practice. Decreasing the value of oscillator strength led to more reliable results. The discrepancy between the reported and observed oscillator strength can be caused by the number of coinciding factors. Firstly, the layer of CuCl grown on the DBR is not a single crystalline. The structural defects can lead to nonradiative transitions decreasing the excitonic oscillator strength. Secondly, despite precautions being taken in order to protect the samples some contact with the

atmosphere was unavoidable. This could lead to partial CuCl degradation and affect the oscillator strength. Finally the physical evaporation is rather simple growth technique and the quality of layers achieved this way is always worse in comparison with more sophisticated techniques like epitaxial growth. Since the substrate on which CuCl was grown was incompatible MgF_2/TiO_2 DBR, the CuCl layer was amorphous and as such comparable rather to the material grown on the glass.

The lower value of Rabi energy than expected is consistent with previously mentioned dependence of oscillator strength on semiconductor layer thickness. CuCl layer thickness in the range of 100 nm corresponds to approximately 150 Bohr radii of its excitons.

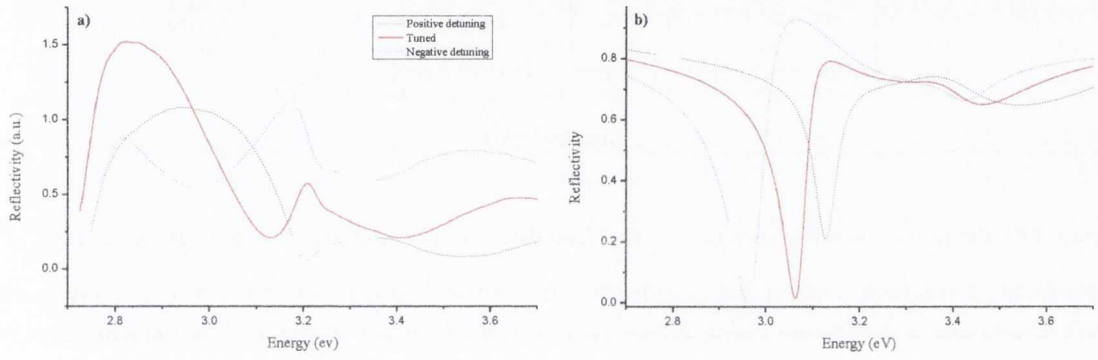

Figure 5.8: ***a)*** *Measured and* ***b)*** *simulated reflectivity spectra of a* $\frac{\lambda}{2}$ *cavity. Dotted lines show a positively detuned (black) and a negatively detuned (blue) cavity. The red lines show the reflectivity of a cavity for zero detuning.*

In order to determine CuCl cavity polariton dispersion the reflectivity spectra are taken for the number of sample locations corresponding to different CuCl thicknesses. The renge of thicknesses was chosen so that the thickness of 107 nm at which the cavity is tuned to the exciton is included. In the *Figure 5.9* the set of reflectivity measurements for CuCl microcavity is shown.

The anti-crossing of lower polariton band (LPB) and upper polariton band (UPB) is shown in *Figure 5.10*. As can be seen the Rabi splitting reaches the value of 275 meV. As expected this is a much higher energy than that observed in GaAs or even GaN or ZnO. Previously reported Rabi energy values for different CuCl cavities at cryogenic temperatures were somewhat lower. The Rabi energy depends not only on the material properties, particularly on the oscillator strength, but also on the cavity design. The cavity discussed in this work is a similar structure to those investigated in [22-23], however there are significant design differences, i.e top mirror type. Moreover the cavity measurements performed for this work were taken at room temperature. Direct comparison between cryogenic and room temperatures in the case of CuCl is impossible because of the thermal dependence of absorption. The exciton line in CuCl is a combination of two excitons called $z_{1,2}$ and z_3.

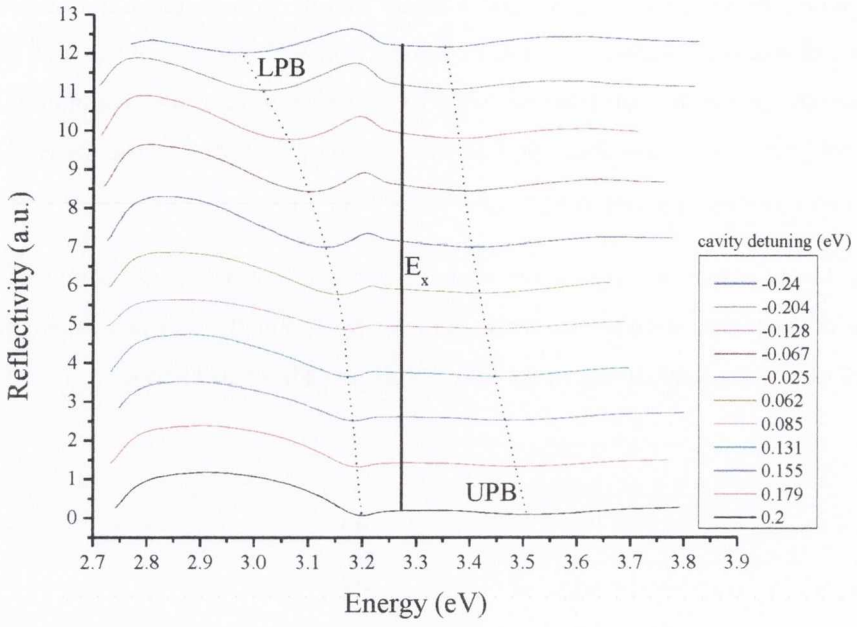

Figure 5.9: The *set of refectivity spectra of* $\frac{\lambda}{2}$ *CuCl microcavity. The detuning is done by the means of CuCl layer thickness variation. During the growth the layer of CuCl was formed into the ridge shape. The translational stage of the cryostat sample holder allows for an adjustment of the sample position and thus the measured thickness.*

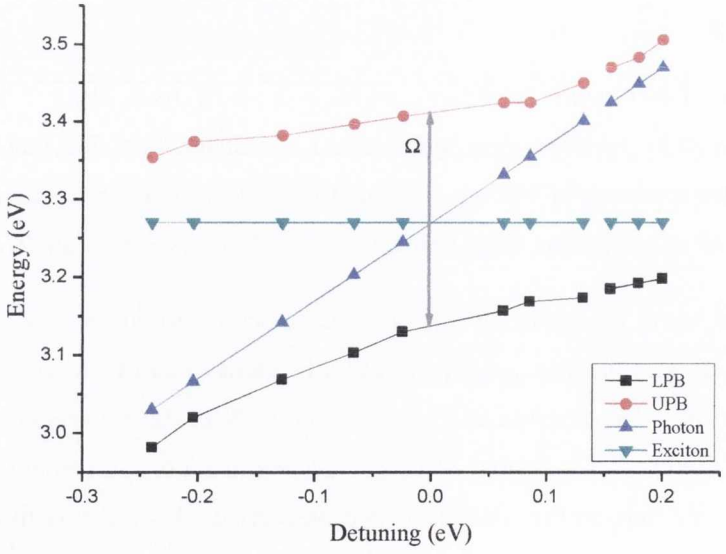

Figure 5.10: *Anticrossing of polariton bands in a CuCl microcavity. The lower polariton band (black squares) and upper polariton band (red circles) visible. Also the lines of a cavity photon (blue triangles) and CuCl exciton (inversed green triangles) are presented.*

At room temperature these lines are broad and overlap. Thus the spectrum of absorption is visible as a single peak $z_{1,2}$ with only the shoulder of z_3[27]. At lower temperatures the spectral lines of both excitons become narrower and can be distinguished in absorption spectra.

The same is true for the reflectivity spectra of CuCl based microcavities. At low temperatures the coupling has to be treated separately for $z_{1,2}$ and z_3. As such, Rabi splitting has to be determined separately. In *Figure 5.11* the measured polariton dispersion is compared with the simulated data.

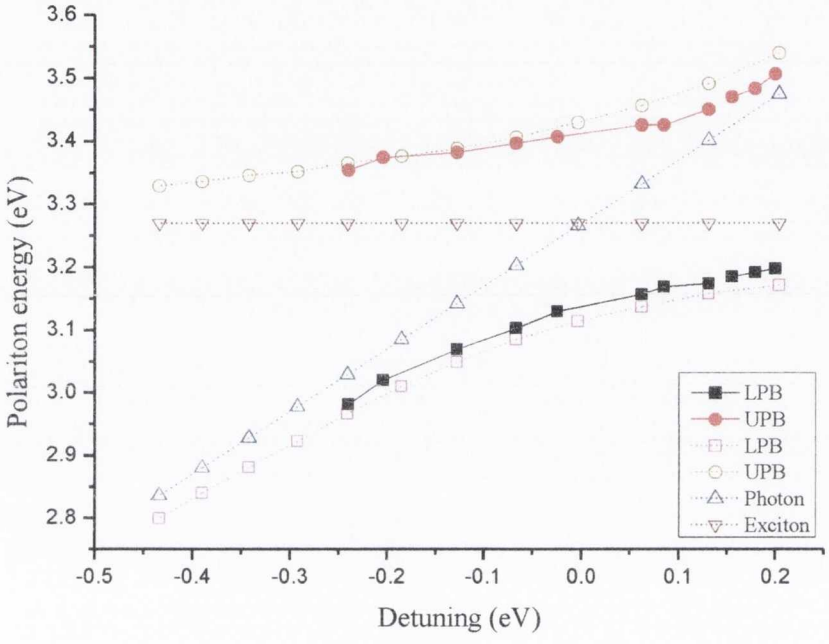

Figure 5.11: *Polariton bands vs energy detuning in CuCl cavity. The solid figures and lines show the measured points. The empty figures and dotted lines represent the simulated data.*

Over the simulation data represented by empty symbols and dotted lines the experimental points are plotted with solid figures. The fit between simulation and experiment is very good.

5.6 Conclusions

Due to a very high exciton binding energy of 190 meV and the oscillator strength two orders of magnitude higher than in GaAS, CuCl is a great material for polariton driven photonic devices. By the vacuum deposition technique the thin layer of CuCl is deposited on a MgF_2/TiO_2 mirror. In order to constitute the optical microcavity the active layer of CuCl is covered with a 30 nm thick gold layer. Such a bulk microcavity is measured with the help of reflectivity setup. Reflectivity spectra taken at room temperature show the splitting feature indicating the strong coupling between the cavity photon and CuCl exciton. From the anticrossing plots of cavity polaritons the Rabi oscillation energy of 275 meV is obtained. According to the author's knowledge, this is the first time the evidence of strong light-matter coupling in bulk CuCl microcavity at room temperature has been reported. The Rabi energy values obtained for bulk CuCl microcavities at cryogenic

temperatures are comparable [22], [23]. In λ thick cavity Rabi energies for Z_3 and $Z_{1,2}$ excitons are 97 meV and 162 meV, respectively. Thus the sum of 259 meV is very close to the value obtained for λ/2 cavity at room temperature presented in this chapter. The fact that relatively low finesse CuCl microcavity growth with the help of an inexpensive vacuum deposition technique is satisfactory to demonstrate strong light-matter coupling at room temperature makes CuCl a very promising material for the growing field of polaritonic devices.

5.7 References

[1] J. J. Pankove, *Optical processes in semiconductors*, II., 1 vols. New York: Dove Publications, Inc., 1975.

[2] S. Christopoulos et al., "Room-Temperature Polariton Lasing in Semiconductor Microcavities," *Physical Review Letters*, vol. 98, no. 12, 2007.

[3] G. Malpuech, A. Kavokin, A. Di Carlo, and J. Baumberg, "Polariton lasing by exciton-electron scattering in semiconductor microcavities," *Physical Review B*, vol. 65, no. 15, 2002.

[4] S. Tsintzos, P. G. Savvidis, G. Konstantinidis, Z. Hatzopoulos, and N. T. Pelekanos, "Towards electrically-pumped microcavity polariton lasers," *physica status solidi (c)*, vol. 5, no. 12, pp. 3594-3596, 2008.

[5] M. Saba et al., "High-temperature ultrafast polariton parametric amplification in semiconductor microcavities," *Letters to Nature*, vol. 414, 2001.

[6] M. Saba, C. Ciuti, S. Kundermann, J. L. Staehli, and B. Deveaud, "Towards a room-temperature polariton amplifier," *Semiconductor science and technology*, vol. 18, p. S325, 2003.

[7] H. Deng and Y. Yamamoto, "Exciton-polariton Bose-Einstein condensation," *Reviews of Modern Physics*, vol. 82, no. 2, pp. 1489-1537, 2010.

[8] J. Kasprzak et al., "Bose–Einstein condensation of exciton polaritons," *Nature*, vol. 443, no. 7110, pp. 409-414, 2006.

[9] P. Littlewood, "PHYSICS: Condensates Made of Light," *Science*, vol. 316, no. 5827, pp. 989-990, 2007.

[10] F. P. Laussy, A. V. Kavokin, and I. A. Shelykh, "Exciton-Polariton Mediated Superconductivity," *Physical Review Letters*, vol. 104, no. 10, 2010.

[11] C. Weisbuch, M. Nishioka, A. Ishikawa, and Y. Arakawa, "Observation of the Coupled Exciton-Photon Mode Splitting in a Semiconductor Quantum Cavity," *Phys. Rev. Let*, vol. 69, no. 23, pp. 3314-3317, 1992.

[12] R. Houdre, C. Weisbuch, R. P. Stanley, U. Oesterle, P. Pellandini, and M. Ilegems, "Measurements of Cavity-Polariton Dispersion Curve from Angle-Resolved Photoluminescence Experiments," *Phys. Rev. B*, vol. 73, no. 15, pp. 2043-2046, 1994.

[13] R. Houdre et al., "Saturation of the strong-coupling regime in a semiconductor microcavity: Free-carrier bleaching of cavity polaritons," *Phys. Rev. B*, vol. 52, no. 11, pp. 7810-7813, 1995.

[14] S. Adachi, *Properties of group-IV, III-V and II-VI semiconductors*, 1 vols. Chichester:

John Wiley & Sons, Ltd, 2005.

[15] S. Tarucha, Y. Okamoto, and others, "Exciton binding energy in GaAs quantum wells deduced from magneto-optical absorption measurement," *Solid State Communications*, vol. 52, no. 9, pp. 815–819, 1984.

[16] T. Tawara, H. Gotoh, T. Akasaka, N. Kobayashi, and T. Saitoh, "Cavity Polaritons in InGaN Microcavities at Room Temperature," *Physical Review Letters*, vol. 92, no. 25, 2004.

[17] L. van Vugt, S. Rühle, P. Ravindran, H. Gerritsen, L. Kuipers, and D. Vanmaekelbergh, "Exciton Polaritons Confined in a ZnO Nanowire Cavity," *Physical Review Letters*, vol. 97, no. 14, 2006.

[18] F. Médard et al., "Experimental observation of strong light-matter coupling in ZnO microcavities: Influence of large excitonic absorption," *Physical Review B*, vol. 79, no. 12, 2009.

[19] N. Antoine-Vincent et al., "Observation of Rabi splitting in a bulk GaN microcavity grown on silicon," *Physical Review B*, vol. 68, no. 15, 2003.

[20] S. I. Tsintzos, P. G. Savvidis, G. Deligeorgis, Z. Hatzopoulos, and N. T. Pelekanos, "Room temperature GaAs exciton-polariton light emitting diode," *Applied Physics Letters*, vol. 94, no. 7, p. 071109, 2009.

[21] K. L. Shaklee, R. F. Leheny, and R. E. Nahory, "Stimulated Emision from the Excitonic Molecules in CuCl," *Phys. Rev. Lett.*, vol. 26, no. 15, pp. 888-891, 1971.

[22] G. Oohata, T. Nishioka, D. G. Kim, H. Ishihara, and M. Nakayama, "Exciton polaritons in bulk CuCl microcavities grown by vacuum deposition," *physica status solidi (c)*, vol. 6, no. 1, 2009.

[23] G. Oohata, T. Nishioka, D. Kim, H. Ishihara, and M. Nakayama, "Giant Rabi splitting in a bulk CuCl microcavity," *Physical Review B*, vol. 78, no. 23, 2008.

[24] C. F. Klingshirn, *Semiconductor optics*. Berlin: Springer-Verlag, 1995.

[25] "SOPRA Thin Films," *SOPRA Thin Films*. [Online]. Available: http://www.sopra-sa.com/.

[26] S. Faure, T. Guillet, P. Lefebvre, T. Bretagnon, and B. Gil, "Comparison of strong coupling regimes in bulk GaAs, GaN, and ZnO semiconductor microcavities," *Physical Review B*, vol. 78, no. 23, 2008.

[27] L. O'Reilly et al., "Growth and characterisation of wide-bandgap, I-VII optoelectronic materials on silicon," *J. Mater. Sci. - Mater. Electron.*, vol. 16, pp. 415-419, 2005.

6 Conclusions and future work

6.1 Conclusions

This work was initially motivated by the development of CuCl on Si as a material system. As was described, CuCl has a small lattice mismatch of <0.4% with Si, offering the possibility of a wide bandgap material with a reduced number of defects relative to other contemporary material systems, such as GaN and ZnO. The study presented in this thesis followed two parallel paths. Firstly the basic parameters were investigated in order to evaluate the materials' quality. The accurate values of such parameters are also required in the numerical simulation process. Secondly, computational models were developed to investigate potential optoelectronic applications of CuCl, and in some cases to verify experimental results.

In the first part of the thesis the optical properties of copper chloride on Si, and related materials of the same group, namely copper bromide deposited on Si, were investigated. Many characteristics of the temperature dependent photoluminescence spectra were analysed to extract the parameters which could subsequently be used to assess the optical quality of the material, and could be used for comparision with CuCl deposited on less suitable substrates, or characteristics of single crystal CuCl. Both CuCl and CuBr were studied. XRD spectroscopy confirmed that the structural quality of the grown semiconductor is very high. The preferable direction of growth of the CuCl layer is (111) on both (111) and (100) oriented Si. The layer was found to be polycrystalline. The low temperature CuCl emission spectrum consists of four peaks. Analysis attributed the peaks to the free and bound excitons and biexcitons, and not to phonon replica features. In the case of the low temperature CuBr PL spectra there was no evidence for biexcitonic peaks. As a result of exciton-phonon interactions, thermal broadening of excitonic peaks is observed. For both CuCl and CuBr the free exciton peak width as a function of temperature was analysed. The coupling strength parameters for exciton-phonon interactions were obtained. At low temperatures up to 150 K, exciton peak broadening is driven by exciton – acoustic phonon interactions. Over 150 K, the interaction between excitons and optical phonons becomes dominant. CuBr PL spectra suggest that exciton interaction with acoustic phonons is lower than in CuCl, which is consistent with literature data for CuBr quantum dots. The exciton-optical phonon interaction in CuBr is also lower than in CuCl, which is also expected. The analysis of the PL intensity as a function of temperature lends insight into the process driving the luminescence quenching. For both halides thermal activation energies of quenching processes are determined. For CuCl the activation energy is determined to be of 167.8±6.5 meV and for CuBr of 59±7 meV. This energy determines the thermal dissociation of excitons. As a possible p-type dopant for CuCl the oxygen was investigated. The PL quenching is more complex than in case of pure CuCl samples. From the spectra of the PL intensity as a function of temperature new mechanisms were introduced

as a consequence of the doping, which manifested as a negative thermal quenching feature in the temperature dependence of the PL intensity. The thermal activation energies associated with these processes were estimated. However, if the electrical experiments would confirm that the holes concentration is really increased due to oxidisation, oxygen can be considered as a p-type dopant.

One of the most important optical parameters of semiconductors is refractive index. In order to successfully simulate and design the optical aspects of the device one has to know the complex refractive index of all the constituent materials. For CuCl the refractive index was obtained from ellipsometry angles measured on a set of CuCl on Si samples with CuCl layers of different thicknesses. The complex refractive index was determined the range 244-1600 nm, which includes energies greater than the band-gap. This refractive index data was subsequently used for the simulations of CuCl microcavity structures.

Due to its low absorption in parts of the THz range, copper chloride is also investigated as a potential material for photonic crystal THz mirrors. The band-gap maps calculated using the plane wave method can be used to determine lattice parameters for which 2D CuCl photonic crystals act as THz mirrors. In the range below 3 THz high reflectivity of 0.99 is achievable only at low temperatures. For frequencies above 8 THz reflectivity of 0.9 occur, even at room temperature. The simulations of designed triangular lattices show that CuCl can compete with THz materials like alumina or steatite and can potentially be applied in THz mirrors and filters.

Placing a semiconductor in a microcavity affects the emission rate and the emission spatial pattern. Such a cavity can work in both, weak and strong coupling regimes. The influence of a cavity can be weak, in which case the cavity is considered as a perturbation for the exciton. Modification of the spatial pattern can be used to increase the extraction efficiency of light from the emitting medium. A number of CuCl structures were studied in order to optimise the thickness of the CuCl layer and multilayer structure in terms of light extraction. While the influence of the microcavity is expected to be reduced for a bulk emitter, the simulations shed light on the optimum parameters and influence replacing the Si substrate with a distributed Bragg reflector. Overall an extraction efficiency of ~14% could be achieved for a 95 nm thick CuCl layer, with a DBR substrate. There was little benefit from the addition of a top mirror, however as CuCl is highly sensitive to water moisture in air a number of capping options were considered and the their effects assessed. Depending on the desired CuCl thickness the appropriate coating can be determined. For 95 nm thick CuCl layer satisfactory results are obtained with SiO_2/TiO_2 pair. In this case the extraction efficiency is not affected with regard to the uncoated CuCl on DBR. Also, a monolayer of TiO_2 does not suppress the light extraction, however due to the high refractive index the phase of the radiation is changed, thus the maxima of extraction efficiency occur for different CuCl thichnesses.

In the case of bulk CuCl, increasing the cavity finesse does not help to increase the extraction efficiency. The spatial pattern of low finesse cavity is very similar for both, bulk and QW emitters in a microcavity. In case of a high finesse cavity the directional modes visible in the farfield for a QW emitter seem to be suppressed by the absorption of the bulk CuCl layer. Thus the enhancement due to cavity effects is much less significant in the bulk case.

A high finesse cavity is capable of containing the photon long enough that it undergoes multiple absorptions and re-emissions in the active medium. In such a case the cavity cannot be considered as a perturbation only and a new quantum state is created. The quasiparticle resulting from the strong coupling of the semiconductor exciton and the cavity photon is called the cavity polariton. Evidence of this new quantum state in a planar bulk CuCl microcavity at room temperature has been observed for the first time. A CuCl microcavity was designed and fabricated. The final design used a bottom 7 pairs of MgF_2/TiO_2 DBR mirror, CuCl bulk intra-cavity layer and a top 30 nm thick gold mirror. The anticrossing of the upper and lower polariton branches has been measured and an enormous Rabi splitting of 275 meV is achieved.

6.2 Future work

The work presented in this thesis is only a small step towards successful device fabrication. Future work may follow parallel paths, keeping in mind a number of milestones. Firstly the material quality of evaporated CuCl on various substrates, however good, is not optimal. Alternative growth techniques such as liquid phase epitaxy (LPE) are already under investigation with a view to achieving monocrystalline CuCl layer growth. Potential devices utilising higher quality CuCl layers would benefit from significantly decreased defect densities which would increase device longevity and efficiency. Another issue requiring further research is doping. The studies of *n* and *p* type doping with zinc and oxygen are rather preliminary up to date. In order to move forward towards p-n junction more detailed dopant analysis should be carried out, and other potential dopants, such as Sn or Ba, should be investigated. Once the techniques of doping are developed and stable, p and n type layers of CuCl can be grown, creating the simplest LED CuCl device. The doping study would also benefit from higher quality single crystal layers. Due to stoichiometry variations in evaporated CuCl, and difficulties in dopant concentration control, it was difficult to perform precise quantitative characterisation of doping. The electrical properties of oxygen doped CuCl also require further characterisation. It was observed that the variation of measurable optical parameters like thermal quenching or PL peak broadening between various vacuum evaporated samples could be significant. As mentioned above improved uniformity of CuCl samples is potentially achievable with more advanced growth techniques such as LPE, Molecular Beam Epitaxy (MBE) or atomic layer deposition.

These techniques, with greater control of the growth parameters, would also dramatically improve the precision of the layer thickness. The thickness is a key parameter for the microcavity based devices. Particularly, the accurate control of CuCl thickness is needed in order to grow CuCl based quantum wells or other dimensionally reduced structures.

Copper chloride being a member of the group of copper halides shares a number of properties with compounds such as copper bromide or copper fluoride. While the band-gap energies of these materials are slightly different all of them are wide band-gap semiconductors capable of UV/blue emission. Alloys composed of two or more of copper halides have yet to be researched with a view to band-gap engineering. The resultant alloys or compounds can also be potentially applied in the design of CuCl based Bragg reflectors or as transparent spacer layers in the structures implementing Cu-Ha QWs.

In chapter 4 the influence of the cavity on the extraction efficiency was discussed. The computational simulations showed that due to significant absorption the bulk microcavity extraction efficiency cannot be improved by the presence of the cavity. On the other hand if the absorbing medium thickness is decreased the extraction efficiency can be significantly improved with proper cavity design. The design of vertical cavity LEDs or lasers requires the active layers to be placed in antinodes of the cavity again demanding precision of the layer growth. The last chapter of this thesis presents the demonstration of strong coupling between the cavity photon and CuCl exciton inside a microcavity. In the work reported to date the relatively simple structure of a bulk CuCl layer placed inside a low finesse cavity was used. Due to the very high exciton binding energy of 190 meV and strong CuCl excitonic oscillator strength, the cavity polaritons were observed in the bulk CuCl microcavity at room temperature. In order to make GaAs or even GaN microcavities operate in the strong coupling regime, the temperature had to be decreased and the active layer thickness reduced in order to increase the exciton binding energy. These steps were not necessary in the case of CuCl. The large Rabi energy of 375 meV in the bulk CuCl microcavity could potentially be further increased with Cu-Ha QWs or a higher finesse cavity. However, limited control over the CuCl layer thickness has curtailed the potential for study of cavity-polaritons in tailored structures. In order to further progress in this field of research, and ultimately Cu-Ha based cavity polariton lasers, more advanced growth techniques will be of great importance.

In summary, some milestones for the future can be outlined. Firstly, work towards a p-n junction should be continued. This includes further study of dopants controlling the conductivity in CuCl in terms of concentrations and species. Besides preliminarily investigated zinc and oxygen, other elements like Ba or Sr should be considered. Once a p-n junction is achieved, the band-gap modification will become of high importance. Again it could be achieved by CuCl doping, or alloying with, for example, other copper halides like CuBr. The weak coupling regime study gave some insight into extraction efficiency of light from the CuCl emitter. Also, the influence of the

protective cladding was investigated. Due to its relatively low refractive index, copper chloride is less affected by the extraction efficiency suppression on the emitter/air interface than other higher index materials such as GaAs. However due to its sensitivity to air moisture the CuCl layers have to be protected. Very strong exciton-photon interaction was observed in bulk CuCl microcavities and even higher Rabi splitting can be studied in the future using quantum well or higher finesse cavities. In the THz range CuCl based photonic crystals can potentially find an application as mirrors and filters. As the features of the PCs are measured in tens of microns in the lower THz frequencies (<3THz) and in microns for high frequency THz (>8THz) relatively straight forward etching techniques should be suitable for fabrication.